



Ricerca di Sistema elettrico

Development and Verification of Calculation Models for the Accident Analysis in Nuclear Power Plants

Giacomino Bandini, Rolando Calabrese, Stefano Ederli

Development and Verification of Calculation Models for the Accident Analysis in Nuclear Power Plants

Giacomino Bandini, Rolando Calabrese, Stefano Ederli - ENEA

Settembre 2014

Report Ricerca di Sistema Elettrico

Accordo di Programma Ministero dello Sviluppo Economico - ENEA

Piano Annuale di Realizzazione 2013

Area: Produzione di energia elettrica e protezione dell'ambiente

Progetto: Sviluppo competenze scientifiche nel campo della sicurezza nucleare e collaborazione ai programmi internazionali per il nucleare di IV Generazione

Obiettivo: Sviluppo competenze scientifiche nel campo della sicurezza nucleare

Responsabile del Progetto: Felice De Rosa, ENEA

Titolo

Development and Verification of Calculation Models for the Accident Analysis in Nuclear Power Plants.

Descrittori

Tipologia del documento: **Rapporto Tecnico**

Collocazione contrattuale: Accordo di programma ENEA-MSE: Piano Annuale di Realizzazione 2013, Linea Progettuale 1, Obiettivo A: Acquisizione, Sviluppo e Validazione di Codici e Metodi per Studi ed Analisi di Sicurezza e Sostenibilità, Task A3.1&2.

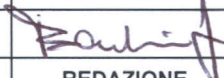
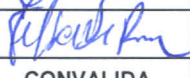
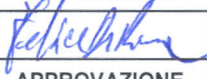
Argomenti trattati: Sicurezza Nucleare

Sommario

This report presents the activities performed in the frame of LP1, Objective A (Acquisition, development and validation of methods and codes for sustainable and safety studies and analyses), Task A3.1&2 of PAR2013, ADP ENEA-MSE. New plenum temperature models are under development to refine the accuracy of the TRANSURANUS code under steady-state and accident conditions (LOCA, RIA). For the purpose, a 2D transient heat transfer model and a finite elements model have been developed. In this frame, ENEA has introduced in TRANSURANUS the FRAPCON-3 plenum temperature model. Furthermore, pre-test analysis of debris bed reflooding experiments have been performed with the ICARE/CATHARE code to support the PEARL experimental program at IRSN and verify the capability of the new 2D porous media model implemented in the last version of the code. Moreover, the calculation of degraded core reflooding scenarios has been performed with the ASTEC code in the frame of the TMI-2 Benchmark Exercise promoted by the OECD. Besides the important achievements in code model development, improvement and verification, these activities contributed to strengthen research collaborations with foreign partners at international level and acquire tools and their knowledge for safety analysis applications to the existing nuclear power plants located near the border of our country.


Note:
Authors:

G. Bandini, R. Calabrese, S. Ederli (ENEA)

2			NOME			
			FIRMA			
1			NOME			
			FIRMA			
0	EMISSIONE	17/09/14	NOME	G. Bandini	F. De Rosa	F. De Rosa
			FIRMA			
REV.	DESCRIZIONE	DATA		REDAZIONE	CONVALIDA	APPROVAZIONE

List of Contents

1.	Introduction	3
2.	Upper plenum temperature calculations: comparison of TRANSURANUS with a 2D model under steady-state conditions	4
2.1	TRANSURANUS models for plenum temperature	4
2.1.1	<i>Standard version options</i>	<i>4</i>
2.1.2	<i>2D transient model</i>	<i>4</i>
2.1.3	<i>FRAPCON-3 model</i>	<i>5</i>
2.2	COMSOL 2D model	7
2.3	Comparisons of models	8
2.4	Results and discussions	9
2.5	Final remarks	11
3.	Complementary ICARE/CATHARE calculations to support the experimental program PEARL	13
3.1	Brief description of the PEARL facility	13
3.2	ICARE/CATHARE modeling of the PEARL facility	14
3.2.1	<i>Minor modifications to account for the new radial size of heated debris bed and bypass</i>	<i>14</i>
3.2.2	<i>Experimental scenario and boundary conditions</i>	<i>15</i>
3.3	ICARE/CATHARE numerical results	16
3.3.1	<i>Heat-up and filling phase</i>	<i>16</i>
3.3.2	<i>Reflooding phase</i>	<i>17</i>
3.3.2.1	Water flow rate equal to 5 m/h	17
3.3.2.2	Water flow rate equal to 10 m/h	19
3.3.2.3	Water flow rate equal to 15 m/h	20
3.3.2.4	Water flow rate equal to 30 m/h	21
3.4	Final remarks	22
4.	Calculation of degraded core reflooding scenarios in the TMI-2 plant with the ASTEC code	48
4.1	Description of code models used	48
4.2	TMI-2 plant and core nodalization	49
4.3	TMI-2 plant initial conditions	50
4.4	SLB sequence and reflooding scenarios	52
4.5	Analysis of results	52
4.6	Final remarks	62
5.	Conclusions	63

 Ricerca Sistema Elettrico	Sigla di identificazione	Rev.	Distrib.	Pag.	di
	ADPFISS–LP1-031	0	L	3	64

1. Introduction


The in-depth analysis of design basis and severe accidents in existing and future nuclear power plants requires the use of qualified numerical tools provided with models able to simulate in a consistent and reliable way all different phenomena that might occur during the various phases of an accident, starting from its initiating event up to the eventual release of radioactive materials into the environment. Furthermore these models shall be able to assess the effectiveness of accident management measures which might be taken to mitigate the consequences of these accidents.

This report presents the results of the activities performed by ENEA in the frame of Tasks 3.1 & 3.2 of PAR2013 – LP1 and devoted to the development and verification of code models used in the analysis of accidents in nuclear power plants. The report is structured in three different sections dealing with:

- Section 2¹ - New plenum temperature models are under development to refine the accuracy of the TRANSURANUS code under steady-state and accident conditions (LOCA, RIA). Efforts have been undertaken to improve the description of the plenum volume sub-system by means of 2D models. For the purpose, a 2D transient heat transfer model and, besides this, a finite elements model, implemented by means of the commercial software COMSOL Multiphysics, have been developed. For comparison, ENEA has introduced in TRANSURANUS the FRAPCON–3 plenum temperature model as well. This section presents the models and their predictions for a PWR fuel pin under steady-state conditions. In addition, preliminary results on the effect of fission gas release are discussed.
- Section 3 – Complementary pre-test analyses of PEARL debris bed reflooding experiments with the ICARE/CATHARE code in the frame of the bilateral cooperation between ENEA and IRSN. The main aim of this work is to support IRSN in the definition of geometry and boundary conditions of the tests that will be carried out in the PEARL facility, and at the same time verify the capability and consistency of the improved porous media models recently implemented in the last version of the code.
- Section 4 - The analysis of degraded core reflooding scenarios with the European ASTEC code, during an alternative severe accident sequence (SBLOCA) simulated on the TMI-2 plant, in the frame of ENEA participation in the activities of the Benchmark Exercise promoted by the OECD/NEA/CSNI. The main aim of this work is to verify the robustness of the code under the most severe accident conditions and assess degraded core coolability by late intervention of emergency core cooling systems.

Finally, the main achievements and conclusions of the above mentioned ENEA activities are summarized in Section 5.

¹ The content of this section was presented at the 23rd International Conference “Nuclear Energy for New Europe”, September 8–11, 2014, Portorož, Slovenia, paper 918. Authors: R. Calabrese (ENEA), A. Schubert (JRC-ITU), P. Van Uffelen (JRC-ITU), L. Vlahovic (JRC-ITU), Cs. Gyóri (NucleoCon).

 Ricerca Sistema Elettrico	Sigla di identificazione	Rev.	Distrib.	Pag.	di
	ADPFISS-LP1-031	0	L	4	64

2. Upper plenum temperature calculations: comparison of TRANSURANUS with a 2D model under steady-state condition

The fuel rod inner pressure is calculated through the definition of the temperature of each free volume filled with gas (upper plenum, lower plenum, gap, cracks, etc.) [1]. In LWR fuel rods a fraction between 40 and 50% of the filling gas is located in the upper plenum. Moreover, the rod internal gas pressure increases under irradiation due to the accumulation of gaseous fission products released into the free volume. To offset the increasing number of moles of fission gas, a reduction of the heat rate is applied towards the end of irradiation in the higher power cases [2]. Therefore, the accurate computation of the plenum temperature is an important issue for the assessment of fuel safety.

The TRANSURANUS modelling is under development to improve the description of the upper plenum temperature under steady-state and accident conditions. The report presents the models under consideration (2D transient, 2D COMSOL Multiphysics, FRAPCON-3) and a comparison of their predictions for a typical 17x17 PWR fuel rod under steady-state conditions [2]. The paper focuses on the contribution of conductive, convective and gamma heating to the heat transfer occurring between the plenum volume and coolant. In the concluding part, preliminary calculations on the effect of fission gas release on the plenum temperature are presented.

2.1 TRANSURANUS models for plenum temperature

2.1.1 Standard version options


For the calculation of the average temperature in the upper plenum, the TRANSURANUS code offers a "low" temperature and a "high" temperature model [1]. In the first, the plenum temperature is coincident with the coolant temperature at the uppermost section, in the second, the temperature is calculated by means of a weighted sum of the cladding inner temperature and the fuel central temperature referring, as previously, to the uppermost slice.

2.1.2 2D transient model

The new 2D transient model implemented in the TRANSURANUS code considers the plenum gas in a static condition under the hypothesis that the convective and the radiative heat transfers are negligible in comparison with the conductive contribution. The model calculates the heat conduction in the plenum volumes means of a finite volume approach in a two dimensional geometry (r, z). According to the time constants of the plenum gas (1–5 s) and cladding (~ 0.05 s), the model adopts a transient analysis approach for the first and a quasi-stationary for the second.

Some relevant characteristics of the model are briefly resumed:

- system of linear equations;
- easy modification of initial and boundary conditions;

 Ricerca Sistema Elettrico	Sigla di identificazione	Rev.	Distrib.	Pag.	di
	ADPFISS–LP1-031	0	L	5	64

- optional solution schemes;
- standard mathematical routines.

The heat transfer process is described by means of an integral form of the Fourier equation for the 2D (r, z) domain Ω :

$$\int_{\tau_k}^{\tau_{k+1}} \left\{ \iint_{\Omega_{ij}} \frac{\partial \theta}{\partial \tau} d\Omega \right\} d\tau = \int_{\tau_k}^{\tau_{k+1}} \left\{ \iint_{\Omega_{ij}} a \left[\frac{1}{r} \frac{\partial \theta}{\partial r} + \frac{\partial^2 \theta}{\partial r^2} + \frac{\partial^2 \theta}{\partial z^2} \right] d\Omega \right\} d\tau \quad (1)$$

Crank–Nicolson, Forward Euler (explicit) and Backward Euler (implicit) schemes are the three optional methods developed for the solution of Eq. (1). The use of CPU time resources depends on the number of nodes used for the geometric description of the plenum volume. Time step controls assure the numerical stability and convergence of the solution.

2.1.3 FRAPCON–3 model

The model predicts the plenum temperature by means of three terms: the energy transfer between the top of the fuel stack and the plenum gas, between the plenum gas and the coolant channel and, finally, between the plenum spring, heated by gammas, and coolant [3]. The model is applicable under steady-state conditions. The convective term is an empirical correlation for the heat transfer between horizontal plates [4]:

$$h_p = \frac{kNu}{D} \quad (2)$$

where:

h_p	heat transfer coefficient	(W / m ² K);
Nu	Nusselt number	(–);
k	thermal conductivity of the plenum gas	(W / m K);
D	cladding inner diameter – hot condition	(m).

The value of the Nusselt number, calculated through the following correlation, is strongly dependent on the regime of heat transfer. A laminar regime is assumed for values of the Rayleigh number up to $2 \cdot 10^7$, thereafter a turbulent regime is fully developed [3]. In the Eq. (3), the values assumed for the coefficients C and m are 0.54, 0.25 and 0.14, 1/3 in laminar and turbulent regime, respectively.

$$Nu = C(GrPr)^m \quad (3)$$

where:

Gr	Grashof number (–):
Pr	Prandtl number (–).

The second term of the FRAPCON–3 model deals with the calculation of the conductive heat transfer between the plenum gas and coolant according to the correlation (4) [3].

$$U_c = \frac{1.0}{\frac{2.0}{Dh_f} + \frac{\ln\left(\frac{D_o}{D_i}\right)}{K_{clad}} + \frac{2.0}{D_o(1.0 + \alpha\Delta T)h_{DB}}} \quad (4)$$

where:

U_c	plenum-to-coolant effective conductivity	(W / mK);
h_f	heat transfer coefficient at the cladding inner surface	(W / m ² K);
k_{clad}	cladding thermal conductivity	(W / m K);
D	cladding inner diameter – hot condition	(m);
h_{DB}	heat transfer coefficient at the cladding outer surface	(W / m ² K);
D_i, D_o	cladding inner and outer diameter – cold condition	(m);
α	cladding thermal expansion coefficient	(1 / K).

This correlation has been implemented in TRANSURANUS by assuming that the laminar layer between the plenum spring and cladding is equal to the initial gap width. In the presented calculations, this value is kept constant. The heat transfer coefficient at the cladding inner surface has been modelled according to the URGAP subroutine [1]. The cladding-to-coolant heat transfer coefficient was defined according to the evaluations of TRANSURANUS (ALPHAL) in the uppermost slice [1].

The third term of the plenum temperature model accounts for the spring gamma heating [3]. This contribution is calculated by means of correlation (5) under the hypothesis that the gamma component is 10% of the power flux and that the attenuation coefficient in the plenum spring is 37.6 (1/m). The average heat flux was calculated accounting for the total inner surface of the cladding under the hypothesis that the radiative source is isotropic.

$$Q_{irr} = 3.76QV_{spring} \quad (5)$$

where:

Q_{irr}	spring gamma heating	(W);
Q	rod average heat flux	(W / m ²);
V_{spring}	spring volume	(m ³).

The resulting plenum temperature correlation is presented in Eq. (6).

$$T_{plenum} = \frac{Q_{irr} + U_c \frac{V_p}{D^2} T_{BLK} + T_{pa} h_p \pi D^2 / 4}{U_c \frac{V_p}{D^2} + h_p \pi D^2 / 4} \quad (6)$$

where:

T_{BLK}	bulk coolant temperature	(K);
T_{pa}	fuel average temperature in the uppermost slice	(K);
D	cladding inner diameter – hot condition	(m);
V_p	plenum volume	(m ³).

The plenum temperature model introduced in the code accounts for a filling gas mixture composed of helium, xenon, and krypton. For the purpose, the URGAP correlations for the thermal conductivity (IHGAP=3) and dynamic viscosity have been employed [1]. The calculation of density and specific heat was based on values found in the open literature [5]. The description of the thermophysical properties dependence on temperature and pressure needs further improvements.

2.2 COMSOL 2D model

The models presented in the previous sections have been introduced as part of the TRANSURANUS source code whereas the COMSOL Multiphysics model was developed as a stand-alone application [6]. The heat transfer process in the geometric domains under consideration (fuel, cladding, spring, plenum gas) is described by means of Eq. (7).

$$\rho C_p \frac{\partial T}{\partial t} + \nabla \cdot (-k \nabla T) = Q - \rho C_p \vec{u} \cdot \nabla T \quad (7)$$

In this equation, T stands for temperature, Q for the volumetric heat source (only for the fuel and spring). The thermophysical properties ρ , C_p and k are, the density, specific heat and thermal conductivity of each domain under consideration.

In this model, the radiative contribution to the heat transfer was neglected. The effect of convection is embedded in the second term in the right part of the eq. (7) where \vec{u} is the velocity vector. This term is included only in the model for the upper plenum². The velocity field of helium in the upper plenum is calculated according to the Navier-Stokes equations (8a, 8b) for a laminar flow regime.

² The helium in the gap is considered as static (velocity = 0) so that heat transfer occurs only via conduction.

$$\frac{\partial \rho}{\partial t} + \rho \nabla \cdot \vec{u} = 0 \quad (8a, 8b)$$

$$\rho \frac{\partial \vec{u}}{\partial t} = \nabla \cdot \left(-pI + \mu \left(\nabla \vec{u} + \nabla \vec{u}^T - \frac{2}{3} \nabla \cdot \vec{u} \right) \right) + \rho \vec{g}$$

In the Eq. 8a and 8b, p stands for the pressure of fluid and I for the identity matrix, μ is the fluid dynamic viscosity and \vec{g} the gravity acceleration. The equations express the conservation of mass (8a) and momentum (8b). The rightmost term in the second equation accounts for the effect of buoyancy that is basically natural convection. For solving the given equations, the following boundary conditions need to be defined: cladding outer temperature, volumetric heat source within the fuel, gamma heating of the spring.

In order to avoid discontinuities in the cladding temperature, the axial power profile was interpolated by means of a smoothing function in such a way that it drops to zero at a level of 40 mm above the top of the fuel stack (Figure 2.1).

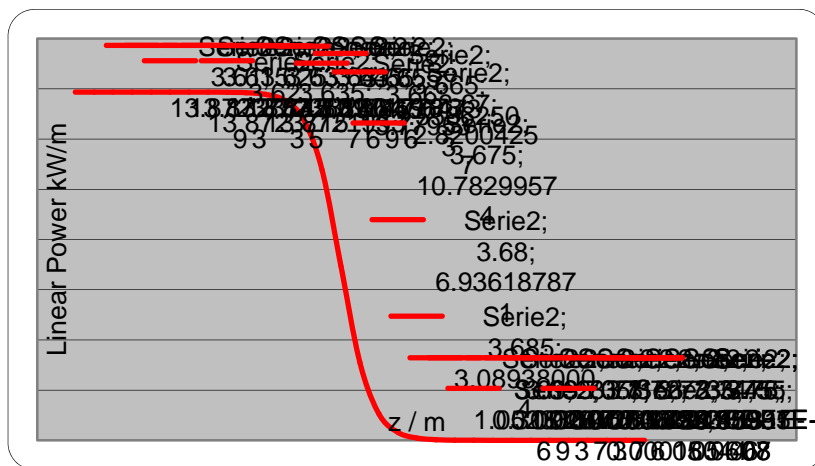


Figure 2.1: Smoothing function at the border fuel stack / plenum

2.3 Comparisons of models

The comparison of presented models was performed under conditions typical for a 17x17 PWR fuel rod as resumed in Figure 2.2 [2]. At the top of the fuel stack, the linear heat rate was about 60% of the peak value (22.97 kW/m) [2]. In the COMSOL calculations, a constant radial power profile and a cosine-shaped axial power profile were assumed whereas the cladding outer temperature boundary condition was defined by means of a simplified thermal-hydraulic model. The determination of the spring gamma heating relied on the correlation (5) [3]. The values of the fuel average temperature and coolant temperature applied in the TRANSURANUS analysis were set in agreement with the values adopted in the COMSOL analysis. The geometrical model employed in the comparison consists of the upper part of the fuel stack (0.05 m) and the plenum volume as shown in Figure 2.2. This analysis

deals with a very short irradiation history (120 s) during which the COMSOL model defines the absolute value of the inner pressure and reaches the steady state. Due to the Navier-Stokes equations, the model is not stable by solving a stationary problem.

Reference design data [2]

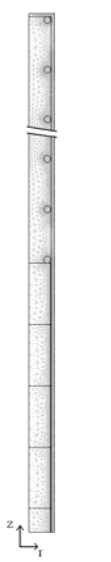
Pitch (mm)	12.6	
Cladding OD (mm)	9.4	
Cladding thickness (mm)	0.61	
Gap thickness (mm)	0.084	
Fuel pellet and spring diameter	8.0	
Pellet length (mm)	11.4	
Plenum length (mm)	254	
Turns in the plenum spring	28	
Plenum spring wire diameter (mm)	1.27	
Helium fill gas pressure (MPa)	2.41	
Active fuel length (m)	3.66	
System pressure (MPa)	15.5	
Coolant inlet temperature (°C)	277	
Coolant flow rate (10 ⁶ kg/m ² h)	12.47	
Pellet density (%TD)	95	

Figure 2.2: Fuel rod specifications and fuel section modelling (rodlet approach)

2.4 Results and discussion

The models' results are presented in Table 2.1. The table resumes the values of the upper plenum temperature and pressure at the end of transient (120 s).

Table 2.1: Results at the end of the short irradiation history (120 s) – upper plenum

	TRANSURANUS models				COMSOL model
	"low" temperature	"high" temperature	2D transient	FRAPCON-3	
Temperature (K)	598.37	720.75	601.25	600.16	600.94
Pressure (MPa)	4.83	5.81	4.86	4.85	4.84

The results confirm that the models are in fair agreement with small deviations from the code "low" temperature option. The values of the 2D transient model presented in Table 2.1 refer to the Crank-Nicolson solution scheme whereas the results of the solution algorithms are gathered in Figure 2.3.

In these preliminary simulations, no fission gas release occurs and the presented results refer to a helium-filled plenum. The agreement shown in the models' predictions is understandable when considering that the conductive heat transfer is the dominant

contribution. This hypothesis is confirmed by the low value of the Rayleigh number calculated by the FRAPCON-3 model fully consistent with a laminar regime of the convective heat transfer that is well described in the COMSOL model. In general, the contribution of the gamma heating is of minor importance.

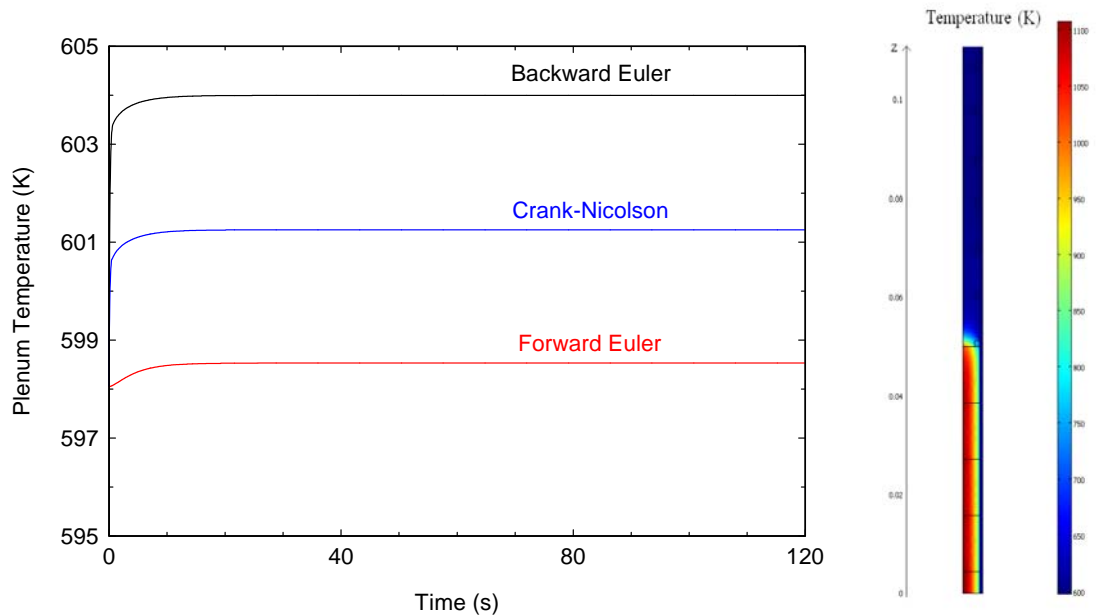



Figure 2.3: Plenum temperature: 2D transient model (left side), COMSOL (right side)

A further calculation was performed by means of TRANSURANUS on an integral fuel rod consistent with the data resumed in Figure 2.2. In this analysis, the irradiation reaches a burn-up of about 56 GWd/t at constant heat rate consistent with the values presented in Section 2.3. The results of this analysis are shown in Table 2.2.

Table 2.2: Results at the end of the irradiation history (56 GWd/t) – upper plenum

Models	"low" temperature	"high" temperature	FRAPCON-3
Temperature (K)	594.73	746.29	603.27
Pressure (MPa)	8.17	9.90	8.27

The FRAPCON-3 model introduced in TRANSURANUS treats the presence of the xenon and krypton fission products vented to the free volume of the fuel rod. The results presented in Table 2.2 deal with a fission gas release of 3.86% at the end of irradiation. The values of the upper plenum pressure are higher than the corresponding results presented in Table 2.1 accounting for the presence of free volumes at higher temperatures not taken into account in the simplified geometry adopted in the previous analysis. Moreover, the increase seen in the prediction of the "high" temperature model confirms the effect of fission gas

 Ricerca Sistema Elettrico	Sigla di identificazione	Rev.	Distrib.	Pag.	di
	ADPFISS–LP1-031	0	L	11	64

release on the average fuel temperature of the uppermost fuel section. This consideration is confirmed in the results of the FRAPCON–3 model where the deviation of the upper plenum temperature if compared to the results of the "low" temperature option is higher than in Table 2.1. The Rayleigh number moves from a value of $0.37 \cdot 10^5$ at the beginning of irradiation to a value of $0.54 \cdot 10^7$ at the end of irradiation thus approaching the transition to a turbulent regime [3]. Across the irradiation, the Prandtl number moves from 0.68 to 1.16 and the Grashof number from $0.55 \cdot 10^5$ to $0.48 \cdot 10^7$.


Two factors may affect the regime of convection: the increase of the fuel central temperature due to the degradation of the gap conductance and the change in the thermophysical properties of the gas mixture. The density of the gaseous fission products xenon and krypton is notably higher than helium [5]. According to the COMSOL results in the rodlet geometry, TRANSURANUS is expected to overestimate the first factor not accounting for the effect due to the presence of the plenum spring. As shown above, the value of the Prandtl number is slightly changing with the composition of the gas mixture. On the contrary, the value of the Grashof number has a significant dependence on the filling gas composition. With a plenum temperature of 600 K and values of the inner pressure ranging in the interval 2–8 MPa, the Grashof number increases, for a common geometry and ΔT , by a factor 550–600 if, instead of helium, xenon is adopted as filling gas [5]. According to these observations, the values of the Rayleigh number calculated for a rodlet filled with helium was $0.23 \cdot 10^5$ while for a xenon-filled rodlet this value increases to $0.40 \cdot 10^8$ well beyond the onset of a turbulent regime for the convective term. For a xenon-filled rodlet, the FRAPCON–3 model predicted a plenum temperature higher than presented in Table 2.1 (633.52 K) while no significant deviations were noted in the results of the 2D transient model (599.14 K).

2.5 Final remarks


A comparison of the models developed to refine the TRANSURANUS evaluations of the upper plenum temperature has been presented. The models' predictions showed a good agreement under the conditions selected for the comparison and indicated that the conductive heat transfer has a prominent role in helium rods. The results of the FRAPCON–3 model showed that fission gas release could cause a transition from a laminar to a turbulent regime of heat transfer. Therefore, the hypothesis of negligible convective contribution to heat transfer assumed in the 2D models should be reconsidered in the case of significant fission gas release. A limited effect was noted for the gamma heating of the plenum spring. These preliminary conclusions will be further assessed and verified. Geometrical effects not modelled in a 1.5 dimensional code and transient conditions will be considered as well.

References

1. K. Lassmann, "TRANSURANUS: a fuel rod analysis code ready for use", Journal of Nuclear Materials 188, 295–302 (1992).

 Ricerca Sistema Elettrico	Sigla di identificazione	Rev.	Distrib.	Pag.	di
	ADPFISS–LP1-031	0	L	12	64

2. G. M. O'Donnell, H.H. Scott, R. O. Meyer, "A New Comparative Analysis of LWR Fuel Designs", Technical Report, NUREG-1754, U.S. Nuclear Regulatory Commission (2001).
3. G. A. Berna, C. E. Beyer, K. L. Davis, D. D. Lanning, "FRAPCON-3: A Computer Code for the Calculation of Steady-State, Thermal-Mechanical Behavior of Oxide Fuel Rods for High Burnup", Technical Report, NUREG/CR-6534 (vol. 1 & 2), U.S. Nuclear Regulatory Commission (1997).
4. H. W. McAdams, "Heat transmission", McGraw-Hill Series in Chemical Engineering (1954).
5. J.-M. P. Tournier, M. S. El-Genk, "Properties of noble gases and binary mixtures for closed Brayton Cycle applications", Energy Conversion and Management 49, 469–492 (2008).
6. COMSOL, COMSOL Inc., COMSOL Multiphysics User's Guide, Version 3.5 (2008).

 Ricerca Sistema Elettrico	Sigla di identificazione	Rev.	Distrib.	Pag.	di
	ADPFISS-LP1-031	0	L	13	64

3. Complementary ICARE/CATHARE calculations to support the experimental program PEARL

The experimental program PEARL has been designed by IRSN to study the reflooding process of a debris bed, considering higher temperatures and higher pressures with respect to experiments carried out in the past. Moreover, the diameter of the test section is large enough to allow 2D/3D effects in the water penetration through the debris bed.

The debris bed is composed of stainless steel spheres heated by induction and enclosed by an unheated debris bed composed of quartz spheres and called bypass.

In the frame of the bilateral cooperation with IRSN, the ENEA has already completed a series of ICARE/CATHARE pre-test calculations to support the IRSN in the definition of geometry and boundary conditions of the tests that will be carried out in the PEARL facility [1].

The main result of the performed studies was those 2D effects, consisting in the preferential water progression through the unheated debris bed outer region (bypass), mainly depends on the assumed water flow rate. Increasing water flow rate and steam production rate, the pressure gradient between the debris bed center and the periphery also increases, favoring the water flow through the bypass to the detriment of the inner region of the heated debris bed. 2D effects becomes not negligible only when the water velocity in the debris bed (40% of porosity) is higher than 15 m/h.


The features of the bypass region, as particles size and porosity, have conversely a negligible effect on the reflooding behavior and the water flow rate, after which 2D effects take place, is basically independent by the features of the bypass.

The objective of the present work is to investigate the effect of the bypass thickness on the reflooding behavior. In particular we want to study if a thicker bypass region can promote the onset of 2D effects at a lower water flow rate. For this purpose the calculations performed with different water flow rates have been repeated, assuming a larger unheated outer region to the detriment of the heated debris bed.

3.1 Brief description of the PEARL facility

The plan of the PEARL facility is represented in the Figure 3.1. The inlet circuit enables the injection of steam and/or water at the bottom of the test section. The outlet circuit, at the top of the test section, allows to collect water and condensed steam in a container of 250 liters. Different values of pressure can be imposed. The test section is set in a nitrogen atmosphere, maintained at a constant temperature of 200°C (473 K).

The provisional plan of the test section is reported in the Figure 3.2. A quartz cylindrical duct, which inner diameter is 540 mm, contains the debris bed composed of stainless steel spheres. Induction heating is used to generate power within the debris bed.

 Ricerca Sistema Elettrico	Sigla di identificazione	Rev.	Distrib.	Pag.	di
	ADPFISS–LP1-031	0	L	14	64

The stainless steel debris bed has a diameter of 500 mm and it is separated from the quartz tube by an unheated debris bed composed of quartz spheres. Such outer region, called bypass, has a thickness of 20 mm and should have higher porosity and permeability than the heated stainless steel debris bed.

The above described debris bed size is the one considered in the previous ICARE/CATHARE pre-test calculations. The new calculations will be based on a bypass thickness of 32.83 mm that increases the cross section of the bypass of about 60%. The external diameter of the heated debris bed becomes then 474.34 mm that reduces the cross section of about 10%.

The stainless steel debris bed and the bypass are supported by a double layer of unheated debris bed; the lowest one composed by pyrex spheres and the above one by quartz spheres.

3.2 ICARE/CATHARE modeling of the PEARL facility

The ICARE/CATHARE modeling of the PEARL facility is basically the same of the previous calculations and it is represented in Figure 3.3. The solid structures of the test section, including the quartz tube and debris beds, are represented with ICARE2 2D axial symmetric components. The ICARE2 2D element extends axially from 0 to 2.66 m.

CATHARE2 volume elements (0D geometry) roughly simulate the void volumes of the PEARL facility below and above the ICARE2 2D element. Inlet and outlet pipelines are represented by CATHARE2 pipe elements (1D geometry). The water-steam behavior within volume and pipe elements is calculated with standard CATHARE2 model. A specific 2D model, adapted for porous medium characteristics, is adopted within the debris bed.

Boundary conditions are imposed at the inlet (steam-water flow rate and temperature) and outlet (pressure) pipes.

3.2.1 Minor modifications to account for the new radial size of heated debris bed and bypass

The different debris bed regions which their main features are illustrated in Figure 3.4. The only modification of the previous modelling concerns the radial size of the heated debris bed and bypass. Pyrex and quartz debris bed remain unchanged. The main features of the heated debris bed and bypass are detailed in Table 3.1.

Table 3.1: Heated debris bed and bypass main features

	Heated debris bed		Bypass	
	old	new	old	new
Composition	Stainless steel	Unchanged	Quartz	Unchanged
Porosity	40%	Unchanged	50%	Unchanged
Spheres diameter	4 mm	Unchanged	8 mm	Unchanged
Height	500 mm	Unchanged	500 mm	Unchanged
Inner diameter	0	Unchanged	500 mm	474.34 mm
Outer diameter	500 mm	474.34 mm	540 mm	540 mm
Number of axial meshes	12	Unchanged	12	Unchanged
Number of radial meshes	10	9	2	3

Differences between new and old debris bed dimensions are underlined. The number of axial and radial meshes adopted in the numerical simulation is also indicated.

The whole radial meshing (heated debris bed plus bypass) is not changed and the new bypass simply includes an additional radial mesh that was the outermost radial mesh of the old heated debris bed. The same radial meshing has been adopted to simplify the comparison between old and new numerical results.


3.2.2 *Experimental scenario and boundary conditions*

The experimental scenario and boundary conditions are the same of the previous calculations. They are reported hereafter. The pressure is imposed as outlet boundary condition and set to 3 bar during the whole simulated transient.

The preliminary heat-up phase, designed to reach a maximum debris bed temperature of 1073 K (700°C), is characterized by the injection of overheated steam at 473 K (200°C), at very low flow rate ($0.4201 \cdot 10^{-3}$ kg/s), during 1900 s. The specific power of the heated debris bed is the same of the previous calculations (127.7 W/kg). The total power is clearly reduced of about 10%, as the cross section of the heated debris bed.

At 1900 s, the steam injection is stopped and a very high water flow rate is imposed (2.9646 kg/s), until 1940 s, to fill the bottom part of the test section, including pyrex and quartz non heated debris beds.

At 1940 s, when the water level is roughly at the bottom of the heated debris bed (948 mm of axial level), the water flow rate is set to the targeted one for the reflooding phase. The calculations performed with different reflooding flow rates will be then repeated taking into account the new heated debris bed and bypass radial size.

 Ricerca Sistema Elettrico	Sigla di identificazione	Rev.	Distrib.	Pag.	di
	ADPFISS-LP1-031	0	L	16	64

The injected water temperature, during filling and reflooding phases, is 381.54 K (108.54°C), corresponding to 25°C of subcooling.

At the beginning of the heated debris bed reflooding (1940 s), the specific power is also increased from 127.7 W/kg to 150 W/kg. Also in this case the total power is 10% lower than the one of the previous calculations.

3.3 ICARE/CATHARE numerical results

Four calculations have been carried-out, with the new ICARE/CATHARE modelling (thicker bypass), imposing different injected water flow rates during the reflooding phase: 5, 10, 15 and 30 m/h. The given water flow rates are expressed as equivalent water velocities in a debris bed 40% of porosities that radially extends on the whole PEARL test section.

In order to make a proper comparison between the obtained numerical results, the selected water flow rates are the same investigated in the previous calculations, except for 40 m/h of water flow rate, not considered in the new calculations. The new calculations will be identified as “Large bypass” and the previous ones as “Regular bypass”.

3.3.1 Heat-up and filling phase

The heat-up (0-1900 s) and filling (1900-1940 s) phases are common to all calculations. The heated debris bed and bypass temperatures at the end of the overheated steam phase (1900 s) are presented in Figure 3.5, in the form of axial profiles at different radial locations.


The bypass thickness has a negligible effect on the central temperature of the heated debris bed ($R = 0$ mm) that is basically the same in both calculations and it is very close to the targeted one (973 K).

The radial gradient of temperature is on the contrary clearly affected by the bypass size and the temperature of the outer mesh of the bypass ($R = 267.4486$ mm) predicted by the “Large bypass” calculation is 60 - 70°C lower than what observed in the “Regular bypass” case.

The temperature distribution in the different debris bed regions and in the cylindrical wall of PEARL test section, predicted by “Regular” and “Large bypass” calculations at the end of the filling phase (1940 s), is illustrated in Figure 3.6.

The temperatures of the pyrex and quartz debris bed, from 0.068 to 0.948 m of axial level, are very close to the injected water temperature (381.54 K).

A large portion of the heated debris, from 0.948 to 1.448 m, is characterized by nearly uniform temperature. Sudden temperature decreases can be observed in the vicinity of the underlying quartz debris bed (axial direction) and, in radial direction, near the boundary between the stainless steel debris bed and the bypass.

 Ricerca Sistema Elettrico	Sigla di identificazione	Rev.	Distrib.	Pag.	di
	ADPFISS–LP1-031	0	L	17	64

In the case of “Large bypass” configuration, the radial extent of the region at uniform temperature is lower than what observed in the “Regular bypass” calculation. Symmetrically, the radial extension of the external colder region is greater in the “Large bypass” calculation with respect to what predicted in the “Regular bypass” case.

The effect of assumed bypass size on the void fraction distribution at the end of the filling phase (Figure 3.7) is negligible. One can observe that the water level is, in both calculations, very close to the bottom of heated debris bed and bypass (axial level = 0.948 m).

3.3.2 Reflooding phase

The results of the new calculations (“Large bypass”), obtained with different flow rates during the reflooding phase, are described in the next paragraphs and compared to the ones of the previous calculations (“Regular bypass”).

3.3.2.1 Water flow rate equal to 5 m/h

The Figure 3.8 shows the radial profile of the collapsed water level, measured from the bottom of heated debris bed and bypass, at the beginning of the reflooding phase (1970 s). One can observe that in both “Regular” and “Large bypass” calculations, the collapsed water level in the bypass is lower than in the heated debris bed and it exhibits a peak at the boundaries between the stainless steel debris bed and the bypass. This is due to capillary pressure difference between the bypass (greater particles diameter and porosity) and the heated debris bed that removes some water from the bypass toward the outer side of the heated debris bed.


In the “Large bypass” calculation, the observed peak is shifted inwards, that is consistent with the larger size of the bypass. Except for this, the differences with the “Regular bypass” case are minimal.

The debris bed behavior during the reflooding is well illustrated from Figure 3.9 to Figure 3.17 that show, for both “Regular” and “Large bypass” cases, the temperatures distribution in the debris bed, the void fraction and the radial profile of the collapsed water level at 2100 s, 2300 s and 2600 s of transient time.

The temperature distribution in the debris bed puts into evidence the effect of the bypass size on the radial extension of the “cold” region at the debris bed edge: slightly greater in the “Large bypass” case. The differences between the two calculations gradually decrease during the course of the transient and, at 2600 s (Figure 3.11), the temperature distribution provided by two calculations is very similar.

The void fraction distribution (Figure 3.12 to Figure 3.14) is practically independent on the bypass size and, in both calculations, the swollen water level remain almost flat indicating a quasi 1D water progression through the debris bed.

The collapsed water level (Figure 3.15 to Figure 3.17) is in general slightly higher in the “Large bypass” case, indicating a little greater axial progression velocity of the water

 Ricerca Sistema Elettrico	Sigla di identificazione	Rev.	Distrib.	Pag.	di
	ADPFISS-LP1-031	0	L	18	64

front. This is probably linked with the steam production rate that, due to the lower debris bed average temperature and power (10% less), is slightly lower with respect to the “Regular bypass” calculation. The differences are, however, very limited and tend to decrease during the course of the transient.

In both calculations, the collapsed water level at 2100 s (Figure 3.15) is slightly lower in the bypass than in the heated debris bed. As before mentioned, this is due to the capillary pressure that removes some water from the bypass toward the outer side of the heated debris bed. With the gradual increase of the water level during the course of the transient, the effect of capillary pressure is contrasted by gravity and friction forces and the collapsed water level becomes flatter and even slightly higher in the bypass than in the central region of the heated debris bed (Figure 3.16 and Figure 3.17). The described behavior can be observed in both calculations.

In any case the radial profile of the collapsed water level doesn’t show any significant preferential penetration of the water through the bypass and the increase of the bypass size is not able to induce 2D effects at the considered water flow rate.

The Figure 3.18 shows the evolution vs. time of the maximum debris bed temperature. The results of “Large” and “Regular bypass” calculations are plotted in the same figure.

One can remark that the quenching of the whole debris bed is slightly anticipated in the case of “Large bypass” calculation. This is consistent with the axial progression of the water that, as before explained, is a little faster than in the case of “Regular bypass”.


The evolution vs. time of temperature and void fraction in the outer side of the bypass (radial mesh 12), at the top (last axial mesh) of the debris bed, is plotted in Figure 3.19. The quenching of the bypass is slightly earlier in the “Large bypass” calculation. This is mainly due to the temperature at the beginning of the reflooding phase that is lower than in the case of “Regular bypass”. The water penetration is not affected by the bypass size, as demonstrated by the first appearance of water at the given level (indicated by void fraction that becomes < 1) that occurs at the same time in both calculations (with an accuracy of 10 s, that is the acquisition frequency of the calculated temperature).

The debris bed thermal behavior during reflooding is synthesized in Figure 3.20 that shows the axial progression of the quenching front at the heated debris bed center (R1 - radial mesh 1) and at the outer side of the bypass (R12 - radial mesh 12). The results obtained in the “Large” and “Regular bypass” calculations are plotted together.

The quenching time is established when the debris bed temperatures becomes lower than: saturation temperature plus 50°C. In the previous work [1] the threshold temperature for the debris bed quenching was: saturation temperature plus 100°C.

The effect of bypass size on the debris bed quenching is rather small.

In both cases the quenching of the bypass takes place before that of the heated debris bed center. This is not correlated to 2D effects on the water penetration but it is mainly explained by the lower temperature of the bypass with respect to the debris bed center.

 Ricerca Sistema Elettrico	Sigla di identificazione	Rev.	Distrib.	Pag.	di
	ADPFISS-LP1-031	0	L	19	64

Moreover, it can be observed that the progression rate of the quenching front, given by the slope of the plotted curves, scarcely depends on the radial position (debris bed center or bypass) further confirming the quasi 1D behavior of the debris bed reflooding.

The earlier quenching of the bypass at the top of the debris bed (Figure 3.19) observed in the “Large bypass” case, due to the temperature differences with respect to the “Regular bypass” calculation, also happens at axial levels below. This is shown by the curves of Figure 3.20 that describe, for both calculations, the axial progression of the quenching front in the bypass. One can however remark that the evolution of the quenching front exhibits almost the same slope in both calculations (the two curves are slightly spaced in time but they remain almost parallel) indicating again that, at the assumed water flow rate, the increase of the bypass size is not able to induce 2D effects on the debris bed quenching.

3.3.2.2 Water flow rate equal to 10 m/h

The distribution of temperatures and void fraction in the debris bed as well as the radial profile of the collapsed water level are illustrated, from Figure 3.21 to Figure 3.26, at two transient times: 2050 and 2250 s.

The bypass size has a minor effect on the temperature distribution. As it was observed in the previous paragraph (water flow rate equal to 5 m/h), the differences between the two calculations mainly concern the radial extension of the “cold” region at the debris bed edge: slightly greater in the “Large bypass” case (Figure 3.21 and Figure 3.22).


The void fraction distribution (Figure 3.23 and Figure 3.24) and the collapsed water level (Figure 3.25 and Figure 3.26) don’t reveal any significant preferential progression of the water through the bypass, indicating that 2D effects are negligible in both calculations.

The evolution vs. time of the maximum debris bed temperature is plotted in Figure 3.27. The effect of the bypass size on the quenching of the whole debris bed is quasi negligible even if a slightly earlier quenching can be observed in the “Large bypass” case.

The Figure 3.28 shows the evolution vs. time of the bypass outer side temperature and void fraction, at the top of debris bed. The effect of the bypass size is more significant than what observed for the maximum debris bed temperature. Lower bypass temperatures are predicted in the “Large bypass” case and this leads to a slightly earlier quenching of the bypass with respect to the “Regular bypass” calculation.

The axial progression of the quenching front at the heated debris bed center (R1 - radial mesh 1) and at the outer side of the bypass (R12 - radial mesh 12) is plotted in Figure 3.29 for both calculations. The comparison of obtained results, confirms the negligible effect of bypass size on the quenching of the heated debris bed center and the minor effect on the quenching of the bypass.

In both cases, 2D effects during the reflooding are negligible.

 Ricerca Sistema Elettrico	Sigla di identificazione	Rev.	Distrib.	Pag.	di
	ADPFISS-LP1-031	0	L	20	64

3.3.2.3 Water flow rate equal to 15 m/h

The debris bed temperature distribution is given, at 2050 and 2150 s of transient time, in Figure 3.30 and Figure 3.31. The void fraction distribution and the radial profile of the collapsed water level are given from Figure to Figure at the same transient times (2050 and 2150 s).

The bypass size has a minor effect on the temperature distribution and, as it was remarked at 5 and 10 m/h of water flow rate, it mainly concerns the radial extension of the “cold” region at the debris bed edge: slightly greater in the “Large bypass” case.

The void fraction distributions (Figure 3.32 and Figure 3.33) highlights a moderate preferential penetration of water through the debris bed outer region. The effect of bypass size is quasi negligible and the observed behavior is mainly due to the pressure gradient between the center and the periphery of the debris bed that is enhanced by the higher steam production rate and pressure drops with respect to lower water flow rates.

The effect of pressure drops on the pressure distribution is also demonstrated by the water collapsed level radial profiles in Figure 3.34 and Figure 3.35. The collapsed water level slightly increases from the center to the debris bed periphery showing that the pressure field is not only affected by the hydrostatic term. The effect of bypass size is not very significant even if one can observe that the radial gradient of the collapsed water level is slightly more pronounced in the “Large bypass” case.


The effect of the bypass size on the whole debris bed quenching is negligible, as it can be observed in Figure 3.36 that shows the evolution vs. time of the maximum debris bed temperature.

The evolution vs. time of the bypass outer side temperature and void fraction, at the top of debris bed, is plotted in Figure 3.37. The bypass quenching is slightly earlier in the “Large bypass” case and, in consideration of the negligible differences on the timing of water arrival (indicated by the void fraction that becomes < 1), this is mainly linked with the temperature at the beginning of reflooding: lower than the one predicted by the “Regular bypass” calculation.

Figure 3.38 shows the axial progression of the quenching front at the heated debris bed center (R1 - radial mesh 1) and at the outer side of the bypass (R12 - radial mesh 12), for both calculations.

In both calculations, the axial progression of the quenching front is slightly faster in the bypass than at the debris bed center (the slope of the curves associated with the bypass quenching is slightly greater than the ones of the debris bed center), confirming that 2D effects begin to appear.

The effect of bypass size on the axial progression of the quenching front is completely negligible at the heated debris bed center.

 Ricerca Sistema Elettrico	Sigla di identificazione	Rev.	Distrib.	Pag.	di
	ADPFISS-LP1-031	0	L	21	64

As remarked at lower flow rates, the quenching of the bypass is slightly earlier in the “Large bypass” case but this does not affect the progression rate of the quenching front that is practical independent on the bypass size (the curves associated with the two calculations remain parallel).

3.3.2.4 Water flow rate equal to 30 m/h

The debris bed temperature distributions, reported at three transient times (1970, 2000 and 2050 s) from Figure 3.39 to Figure 3.41 show, as it was observed at lower water flow rates, that the radial extension of the “cold” region at the debris bed edge is slightly greater in the “Large bypass” case.

The void fraction distributions at the same transient times (1970, 2000 and 2050 s), illustrated from Figure 3.42 to 3.44, point out the preferential water penetration trough the outer region of the debris bed.

The void fraction distribution at 2050 s (Figure 3.44) shows that some water, after flowing through the outer side of the debris bed, remains above the porous medium. Indeed, the produced steam prevents the downward flow of water and a bottom to top reflooding continues to takes place.


The described 2D behavior is remarked in both “Large” and “Regular bypass” calculations and any significant effect of the bypass size can be observed.

The 2D behavior of the water penetration though the debris bed is confirmed by the radial profiles of the collapsed water level at 1970, 2000 and 2050 s (Figure 3.45 to Figure 3.47) that in both cases increases from the center to the debris bed periphery, demonstrating that the pressure field is not only affected by the hydrostatic term. The radial gradient of the collapsed water level is slightly more pronounced in the “Large bypass” case but the differences with the results of the “Regular bypass” calculation are not very significant which reveals the minor role of the bypass size to promote the 2D behavior of the water penetration.

The evolution vs. time of the maximum debris bed temperature (Figure 3.48) shows that the effect of the bypass size on the quenching of the whole debris bed is completely negligible.

The evolution vs. time of the bypass outer side temperature and void fraction, at the top of debris bed, is plotted in Figure 3.49. The water arrival at the top of the bypass (indicated by the void fraction that becomes < 1), is slightly earlier in the “Large bypass” calculation but the difference with the “Regular bypass” case is quasi insignificant and the slightly earlier bypass quenching, observed in the “Large bypass” case, is mainly linked with the temperature at the beginning of reflooding: lower than the one predicted by the “Regular bypass” calculation.

The debris bed behavior during the reflooding is synthesized in Figure 3.50 that shows the axial progression of the quenching front at the heated debris bed center (R1 - radial mesh 1) and at the outer side of the bypass (R12 - radial mesh 12), for both calculations.

 Ricerca Sistema Elettrico	Sigla di identificazione	Rev.	Distrib.	Pag.	di
	ADPFISS-LP1-031	0	L	22	64

In both calculations, the axial progression of the quench front is faster in the bypass than at the debris bed center (the slope of the curves associated with the bypass quenching is greater than the ones of the debris bed center). The differences on the progression rate of the quenching front are much more consistent than those observed at 15 m/h of water flow rate, confirming that 2D effects are well established when the water flow rate is equal to 30 m/h.

The effect of the bypass size is not significant even if the progression of the quenching front in the bypass is slightly faster in the “Large bypass” case.

2.4 Final remarks

The performed complementary sensitivity calculations with a ticker unheated region (bypass), at the outside of the stainless steel debris bed, has a very limited effect on the debris bed behavior during the reflooding.

In particular, the increase of the bypass size has a poor efficacy to enhance 2D effects, consisting on a preferential water penetration through the external debris bed region, during the reflooding.

The obtained results confirm the conclusions of the previous work [1] on the essential role of the water flow rate to enhance 2D effects. Increasing water flow rate and steam production rate, the pressure gradient between the debris bed center and the periphery also increases, favoring the water flow through the bypass to the detriment of the inner region of the heated debris bed.

2D behavior of the water penetration within the debris bed becomes visible, independently on the bypass thickness, at a water flow rate of 15 m/h. 2D effects are well established when the water flow rate is equal to 30 m/h.

References

1. G. Bandini, R. Calabrese, N. Davidovich, F. De Rosa, S. Ederli, F. Rocchi, M. Di Giuli, M. Sumini, F. Teodori, W. Ambrosini, A. Manfredini, F. Oriolo, “Calcoli e validazioni relativi ai codici di calcolo specifici per l'analisi degli incidenti gravi”, Report Ricerca di Sistema Elettrico RdS/2013/060, Rapporto ENEA ADPFISS-LP1-017.

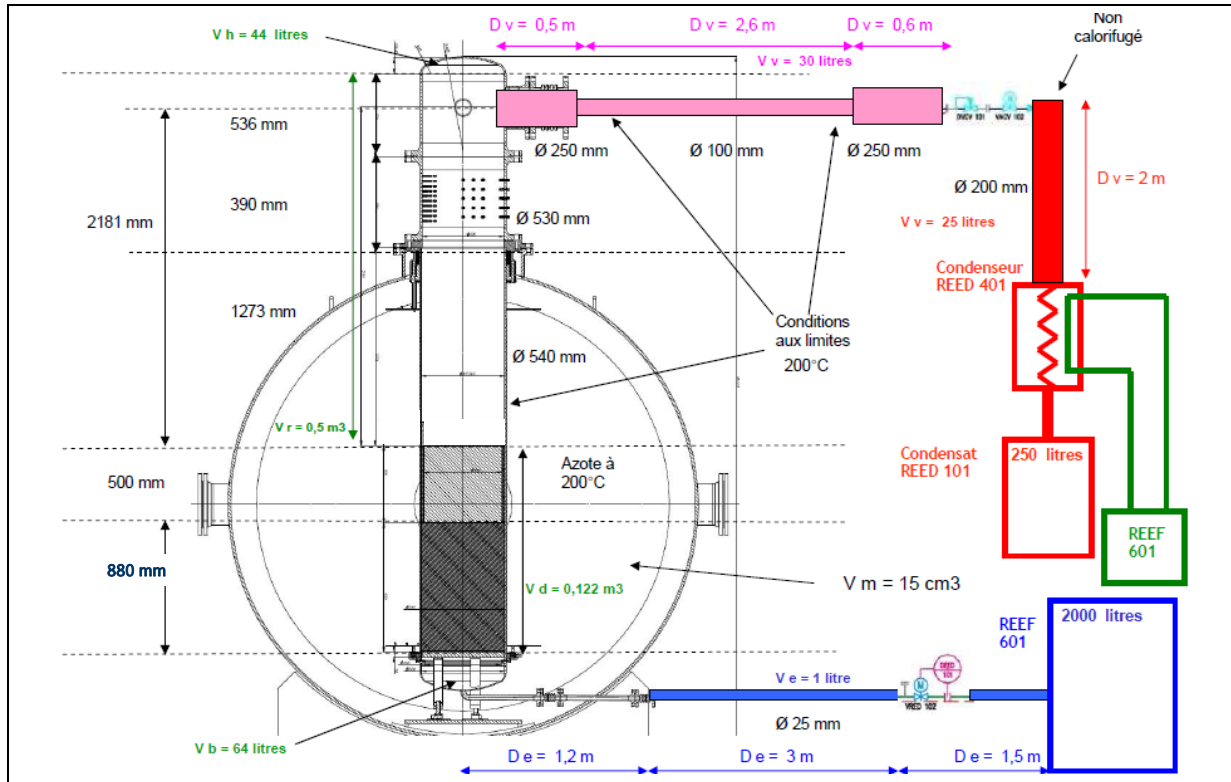


Figure 3.1: PEARL facility

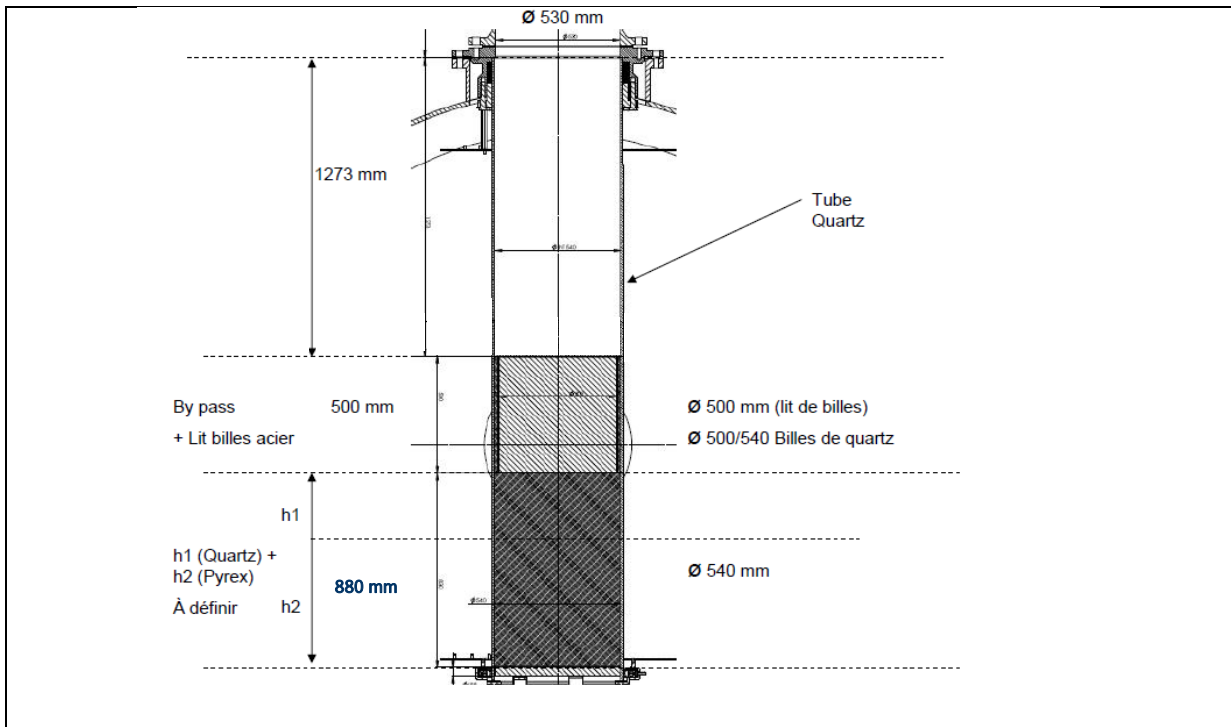


Figure 3.2: PEARL test section

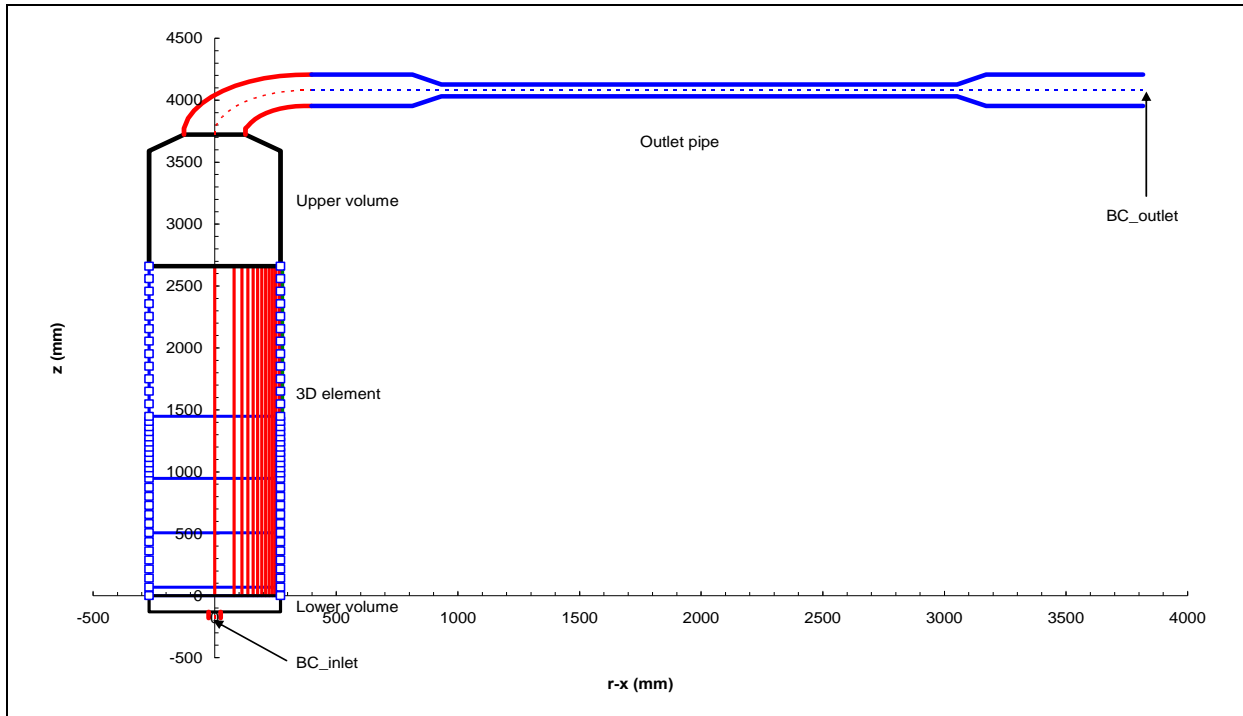


Figure 3.3: ICARE/CATHARE modelling of PEARL facility

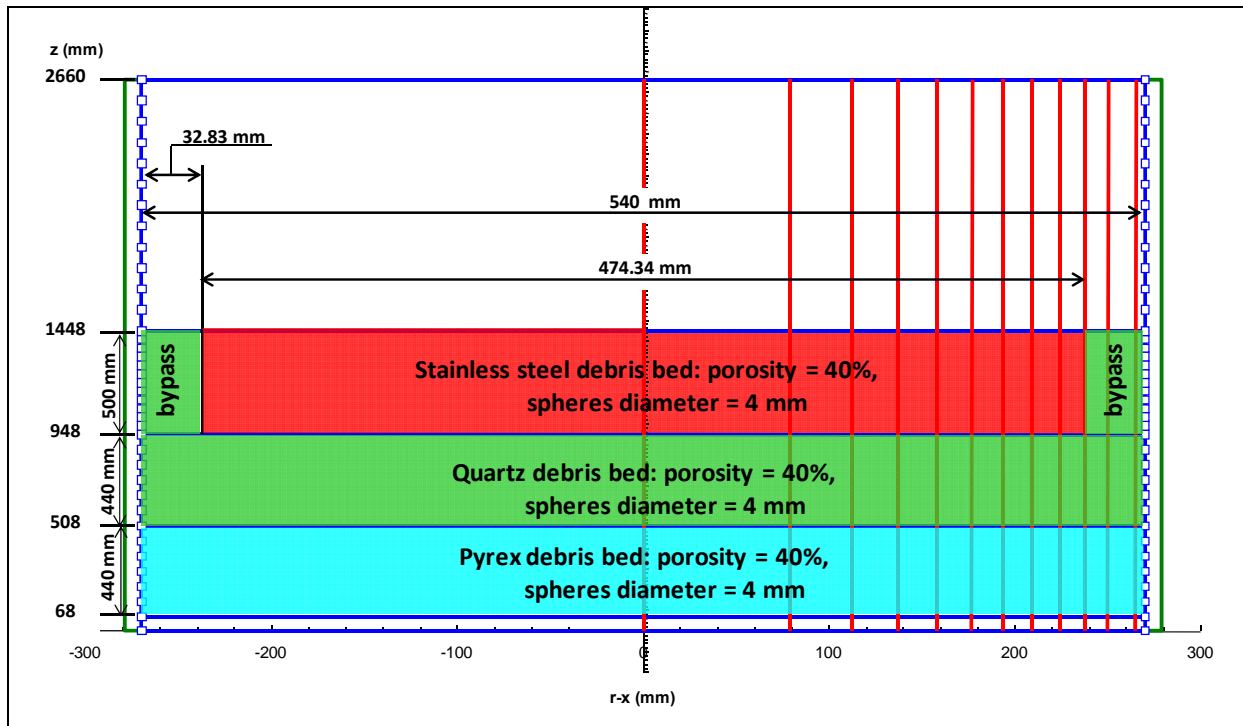


Figure 3.4: ICARE/CATHARE modelling of PEARL facility; debris bed regions

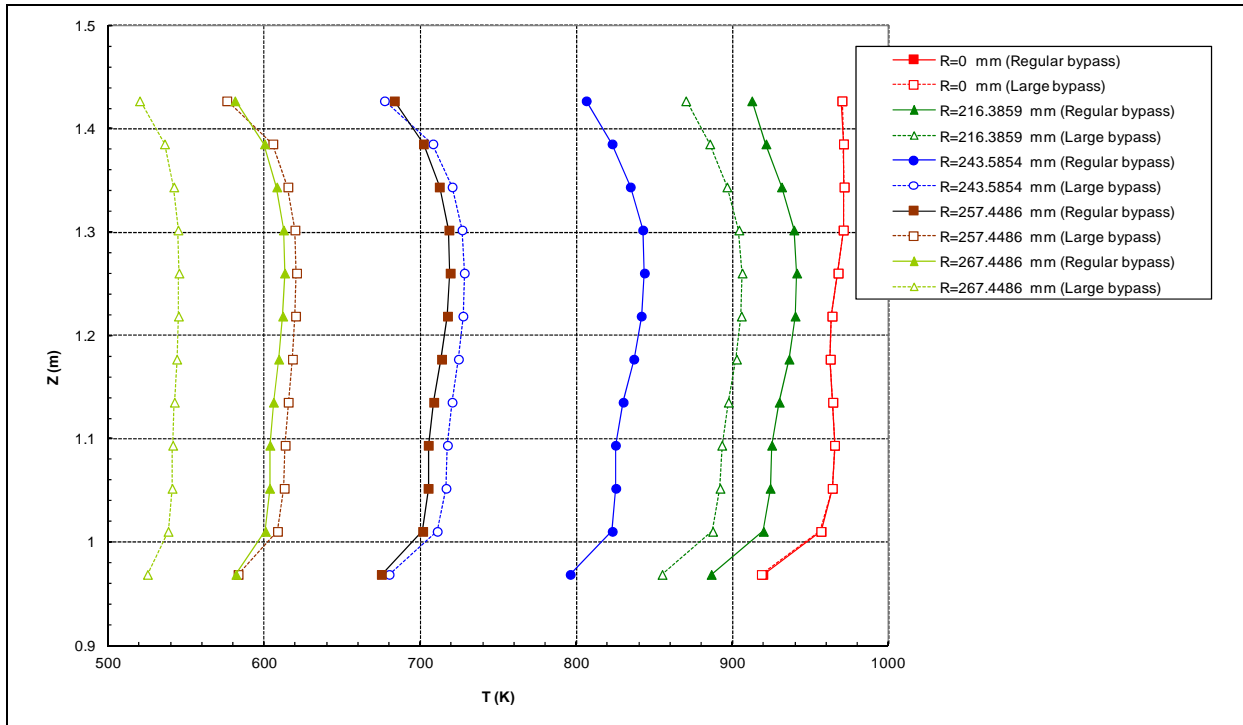


Figure 3.5: Axial temperature profiles at the end of overheated steam phase (1900 s)

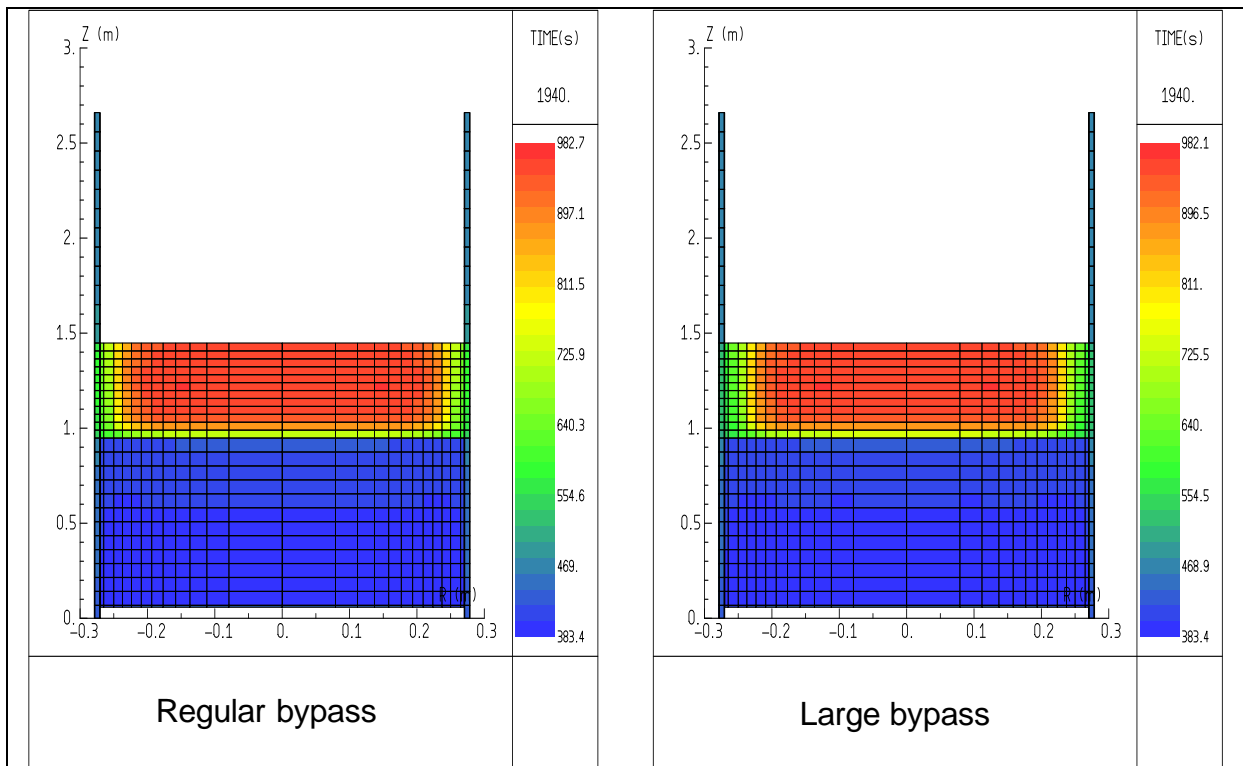


Figure 3.6: Temperature distribution at the end of filling phase (1940 s)

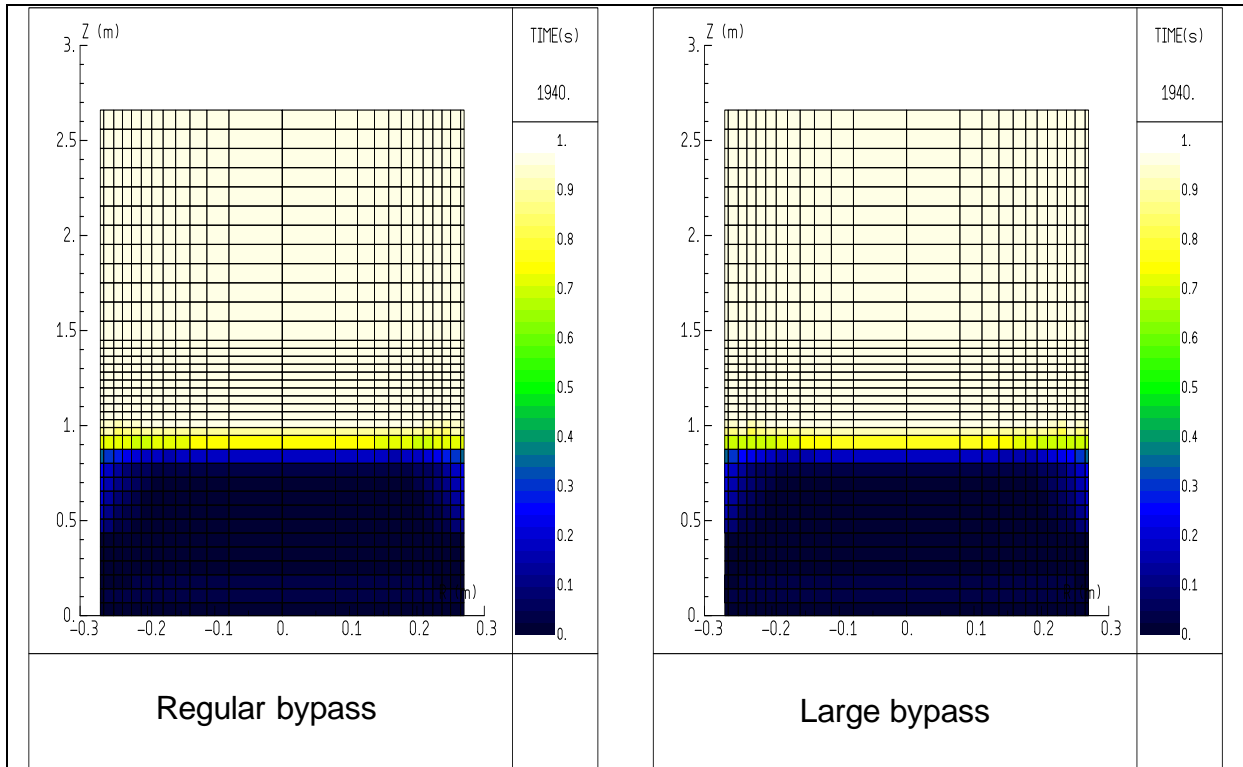


Figure 3.7: Void fraction distribution at the end of filling phase (1940 s)

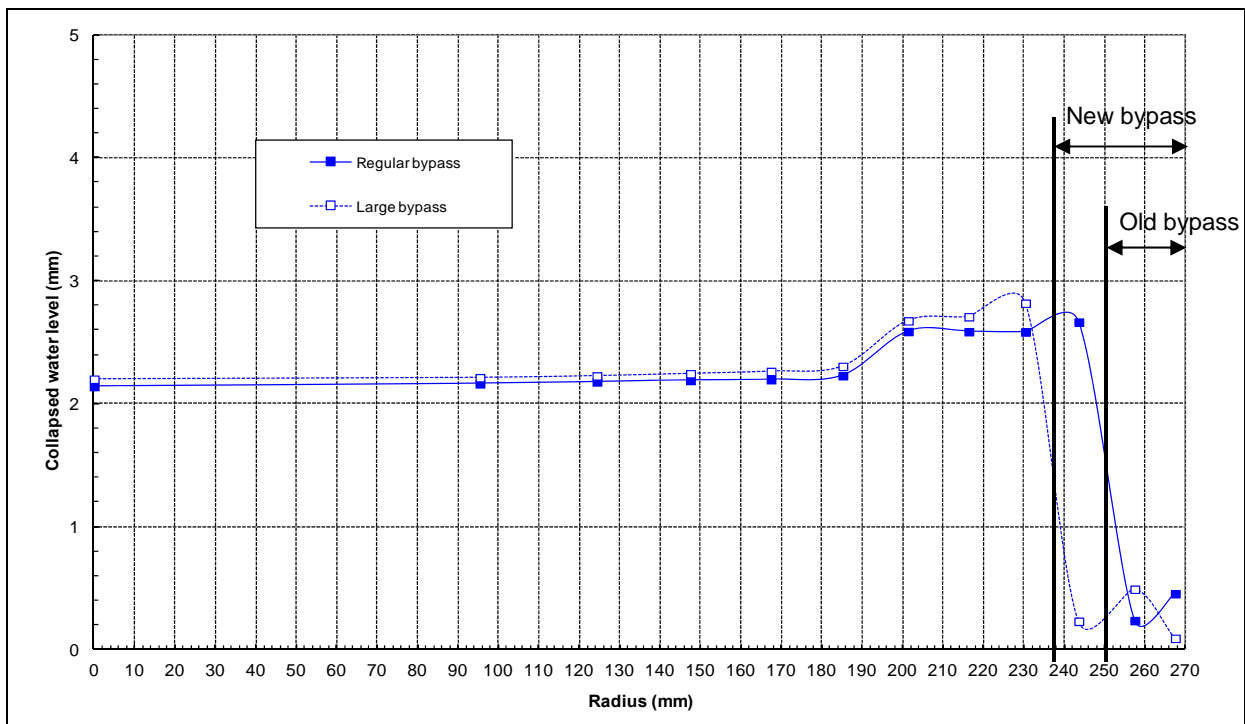


Figure 3.8: Flow rate = 5 m/h; Collapsed water level radial profile at 1970 s

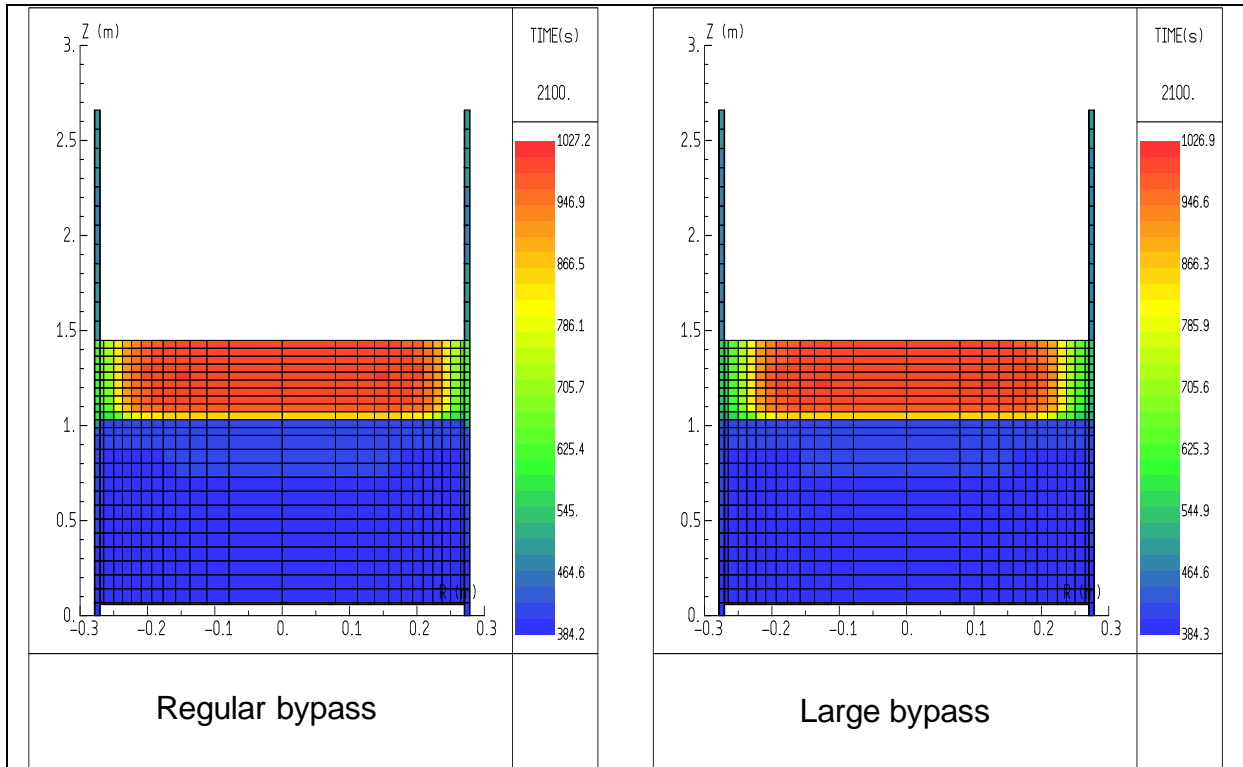


Figure 3.9: Flow rate = 5 m/h; Temperature distribution at 2100 s

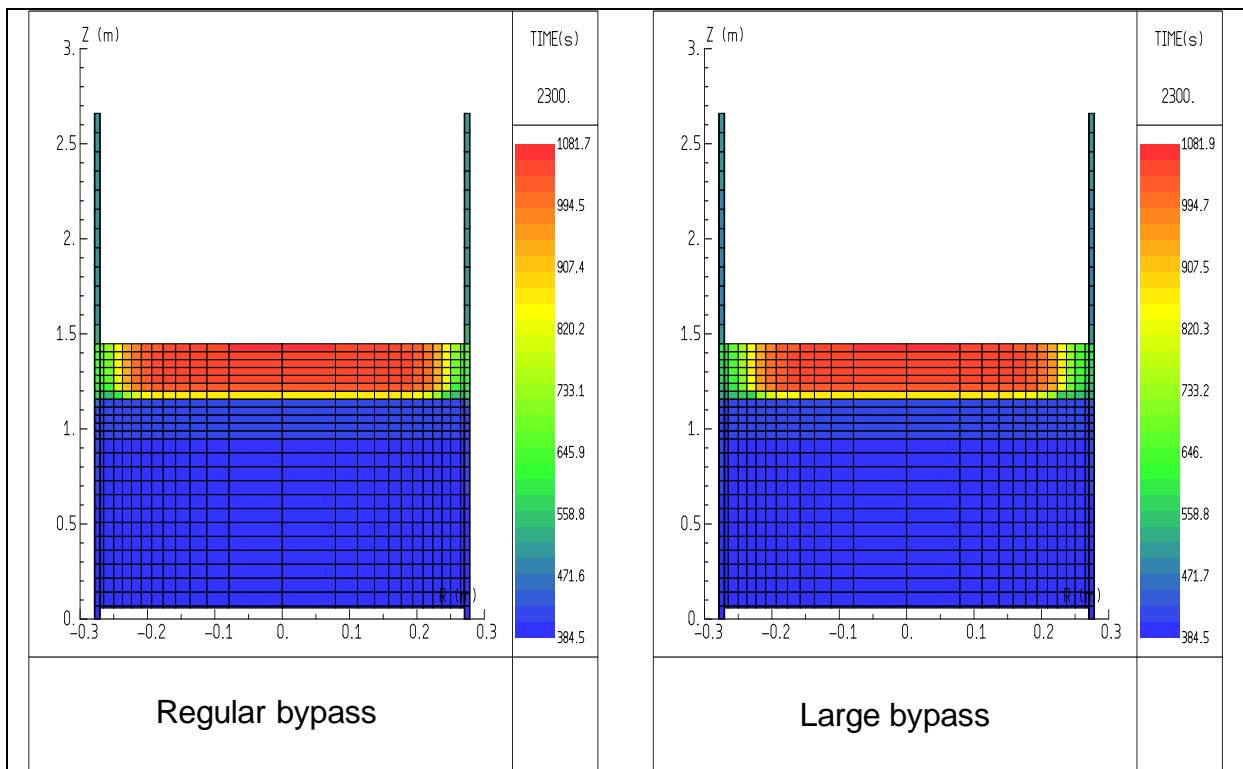


Figure 3.10: Flow rate = 5 m/h; Temperature distribution at 2300 s

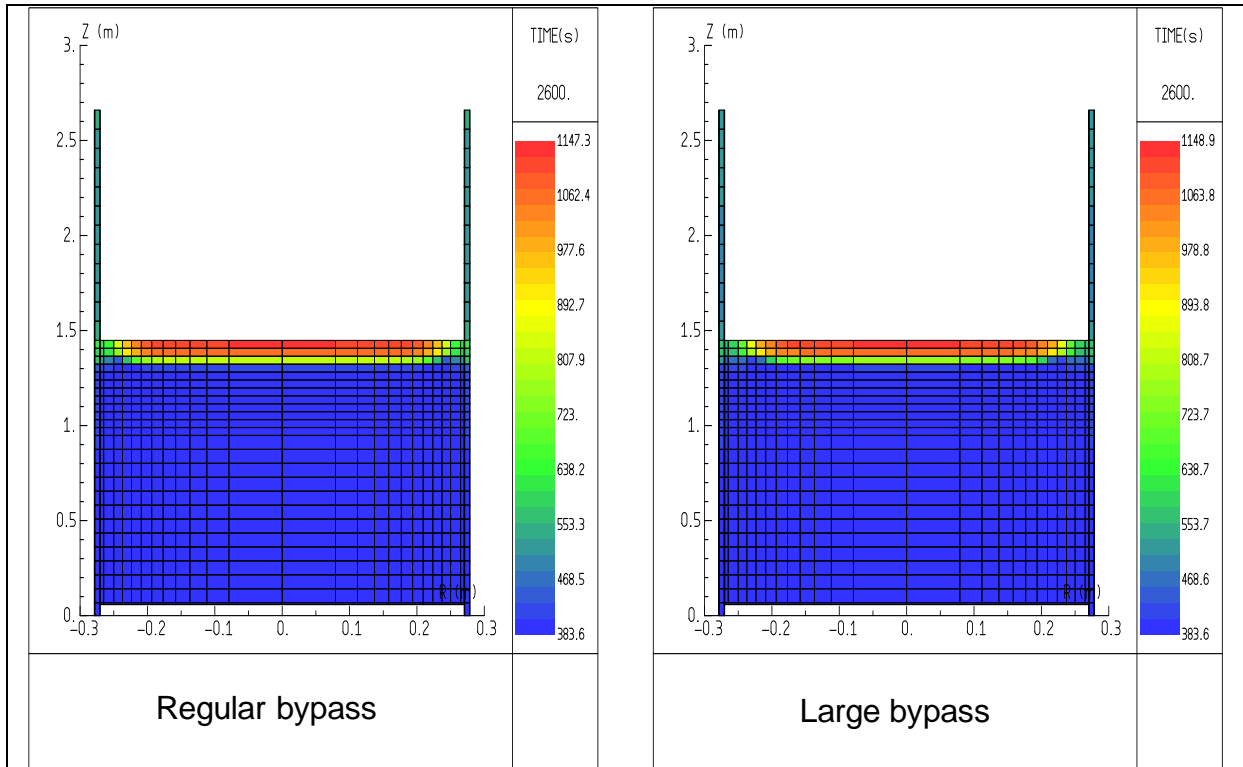


Figure 3.11: Flow rate = 5 m/h; Temperature distribution at 2600 s

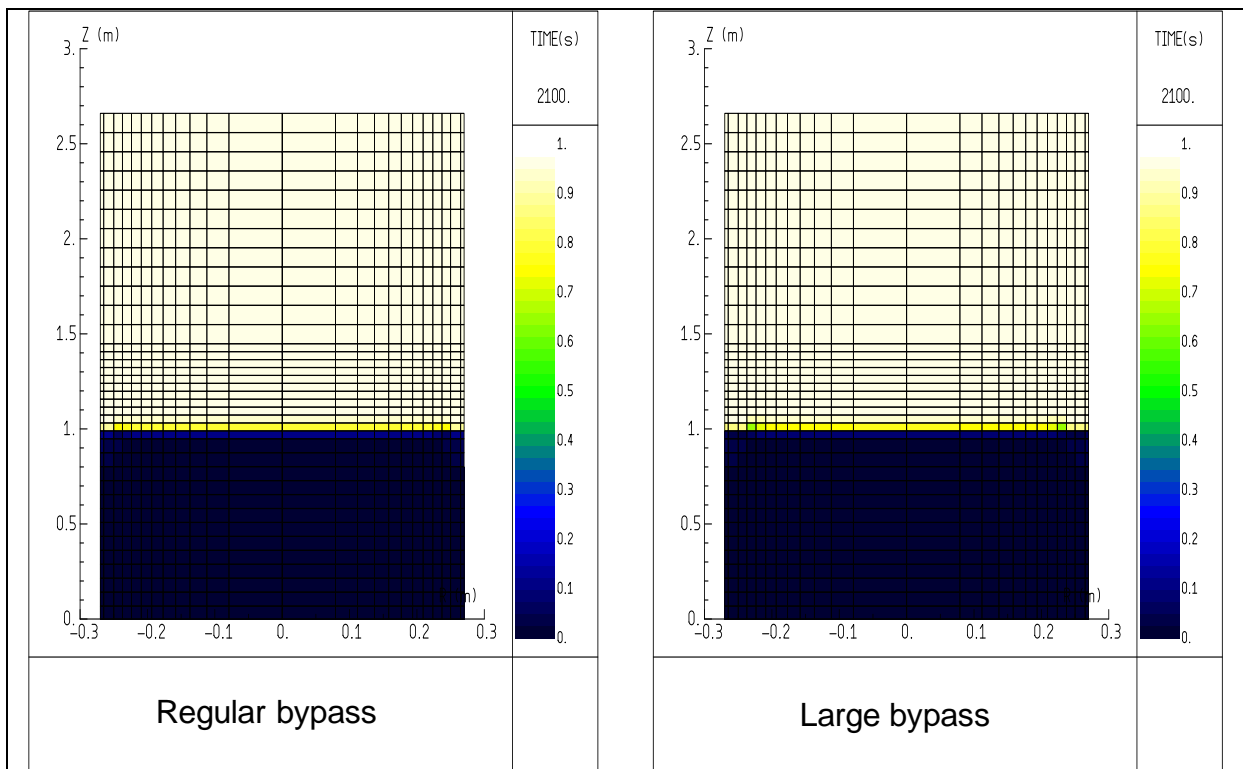


Figure 3.12: Flow rate = 5 m/h; Void fraction distribution at 2100 s

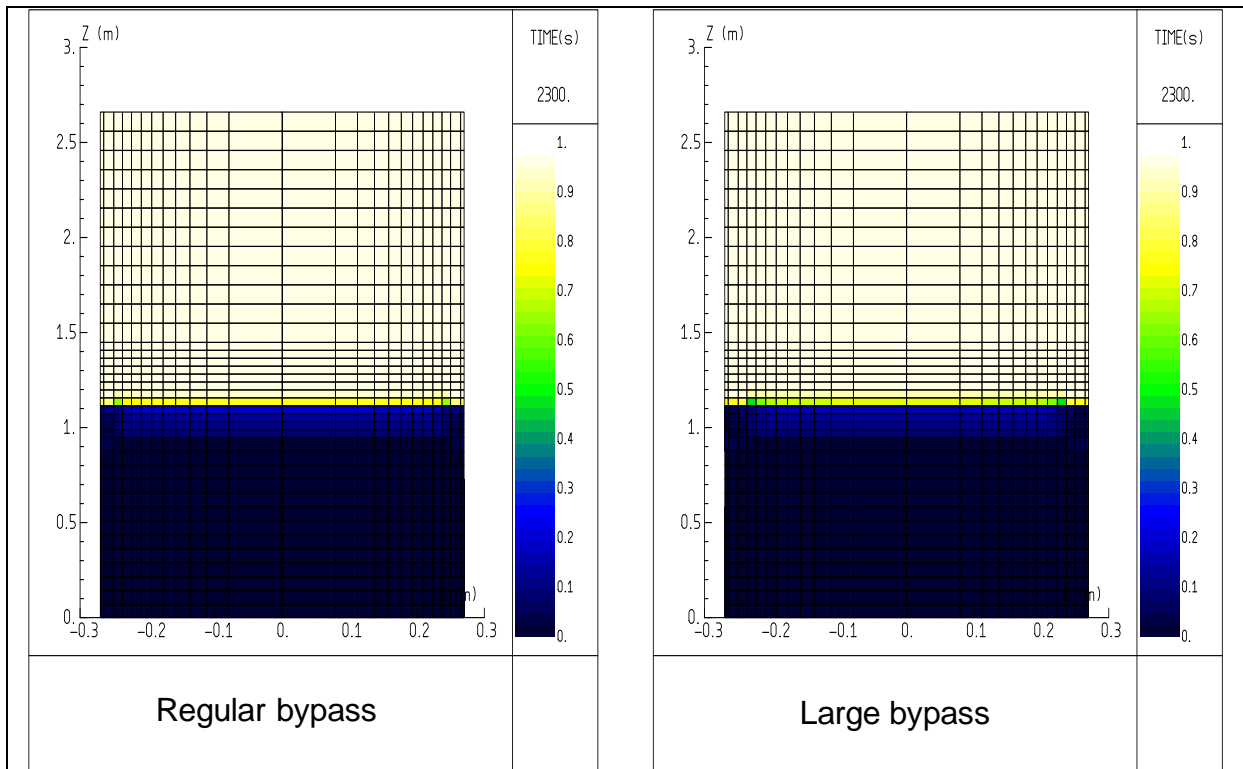


Figure 3.13: Flow rate = 5 m/h; Void fraction distribution at 2300 s

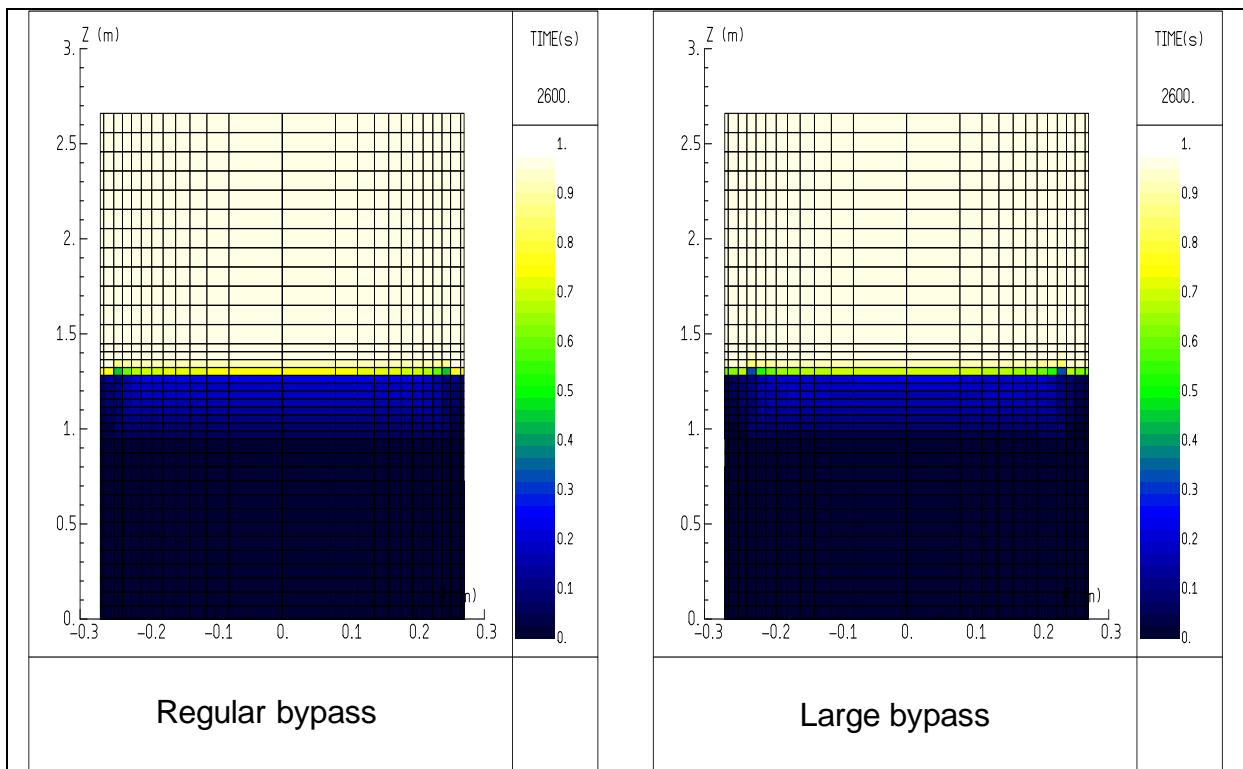


Figure 3.14: Flow rate = 5 m/h; Void fraction distribution at 2600 s

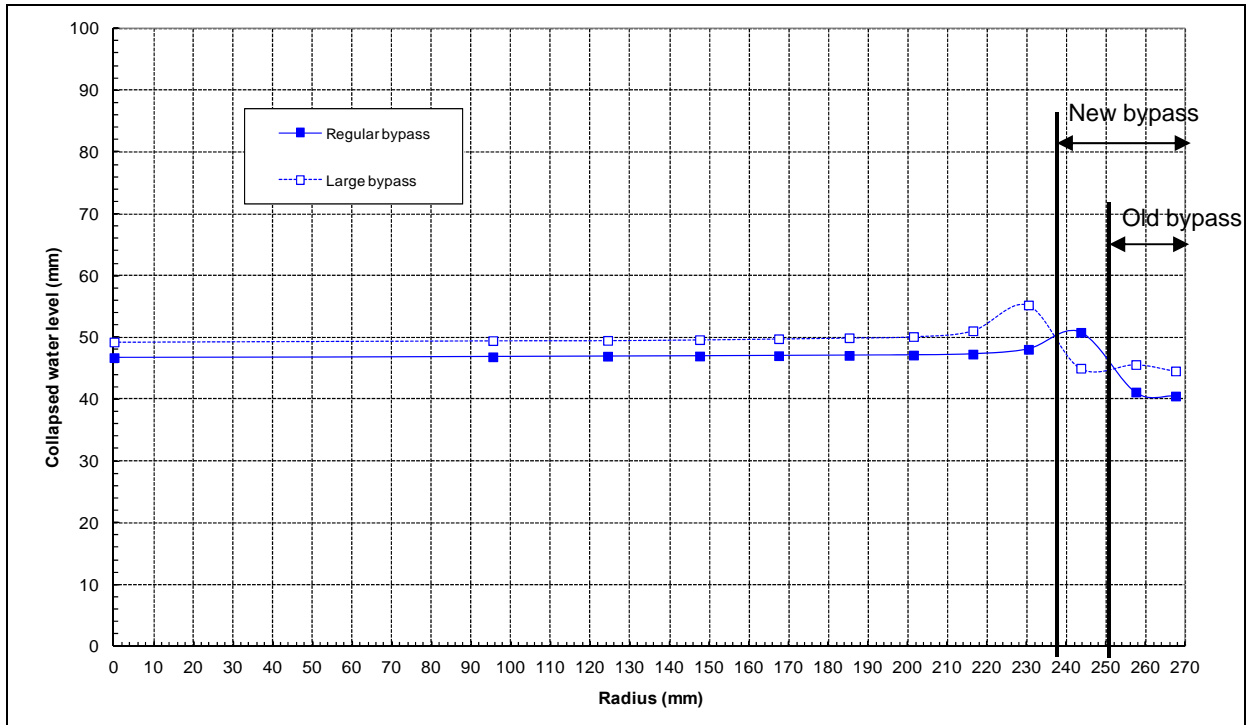


Figure 3.15: Flow rate = 5 m/h; Collapsed water level radial profile at 2100 s

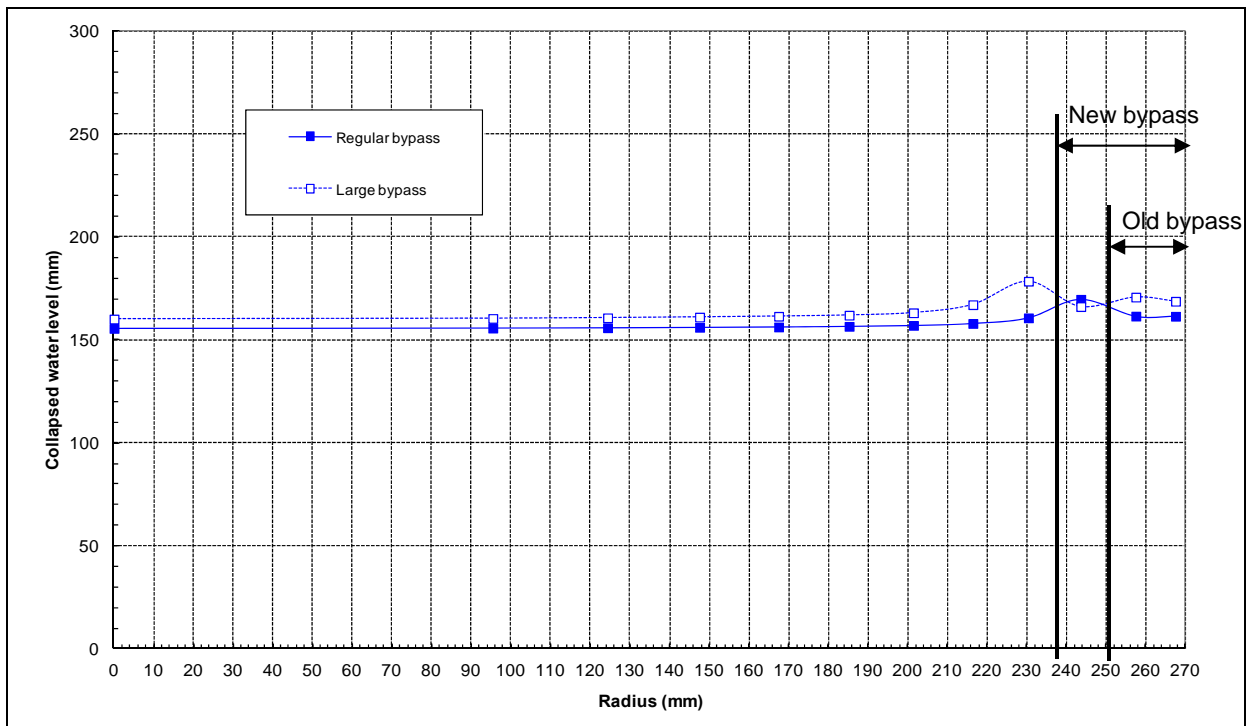


Figure 3.16: Flow rate = 5 m/h; Collapsed water level radial profile at 2300 s

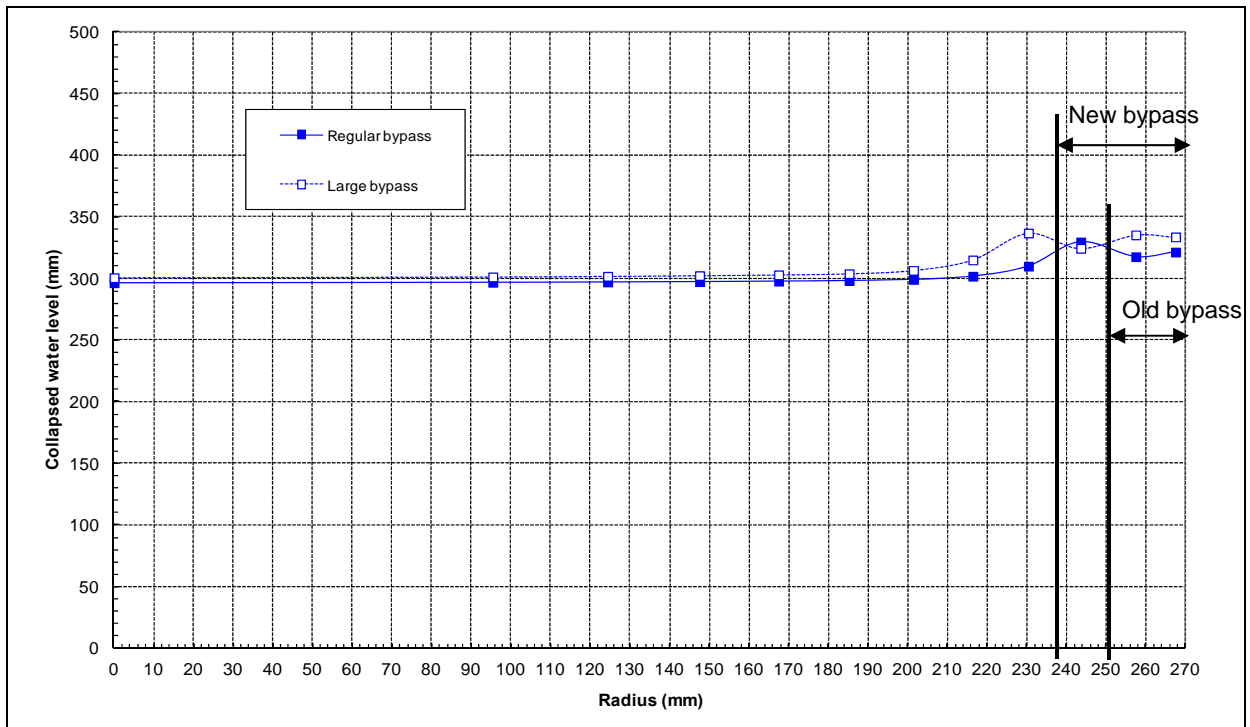


Figure 3.17: Flow rate = 5 m/h; Collapsed water level radial profile at 2600 s

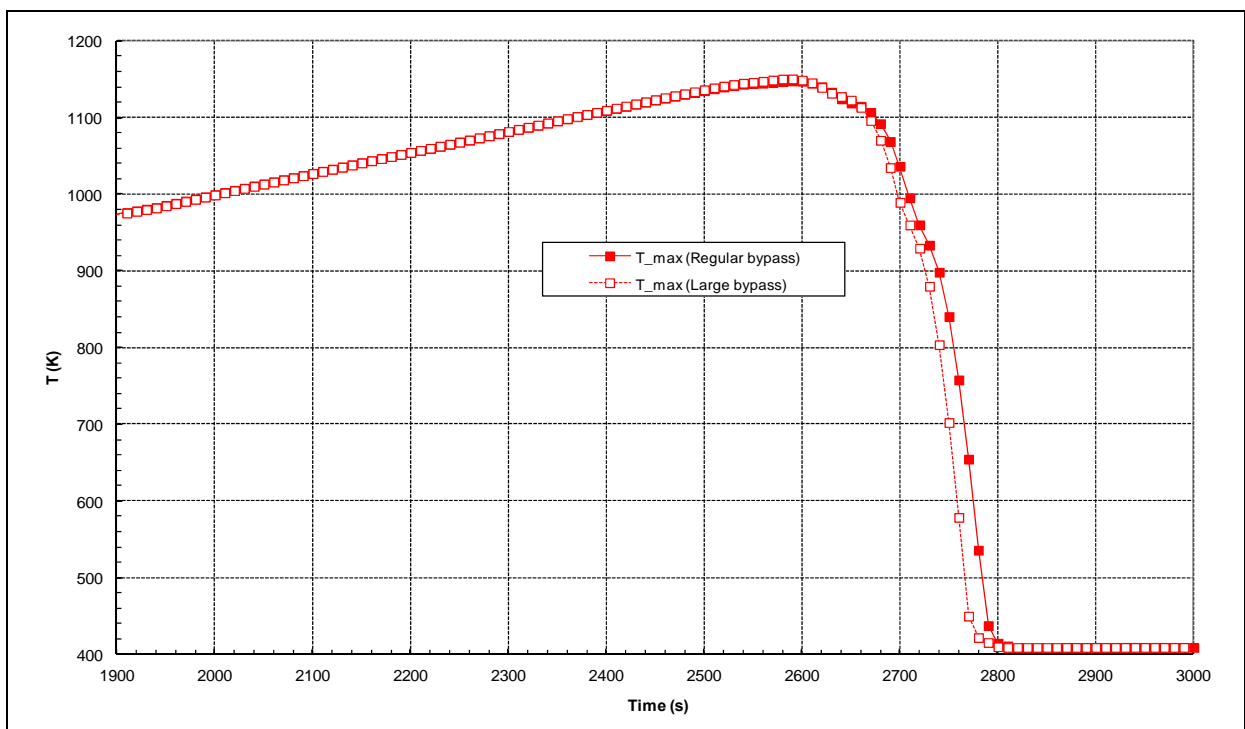


Figure 3.18: Flow rate = 5 m/h; Evolution vs. time of the maximum debris bed temperature

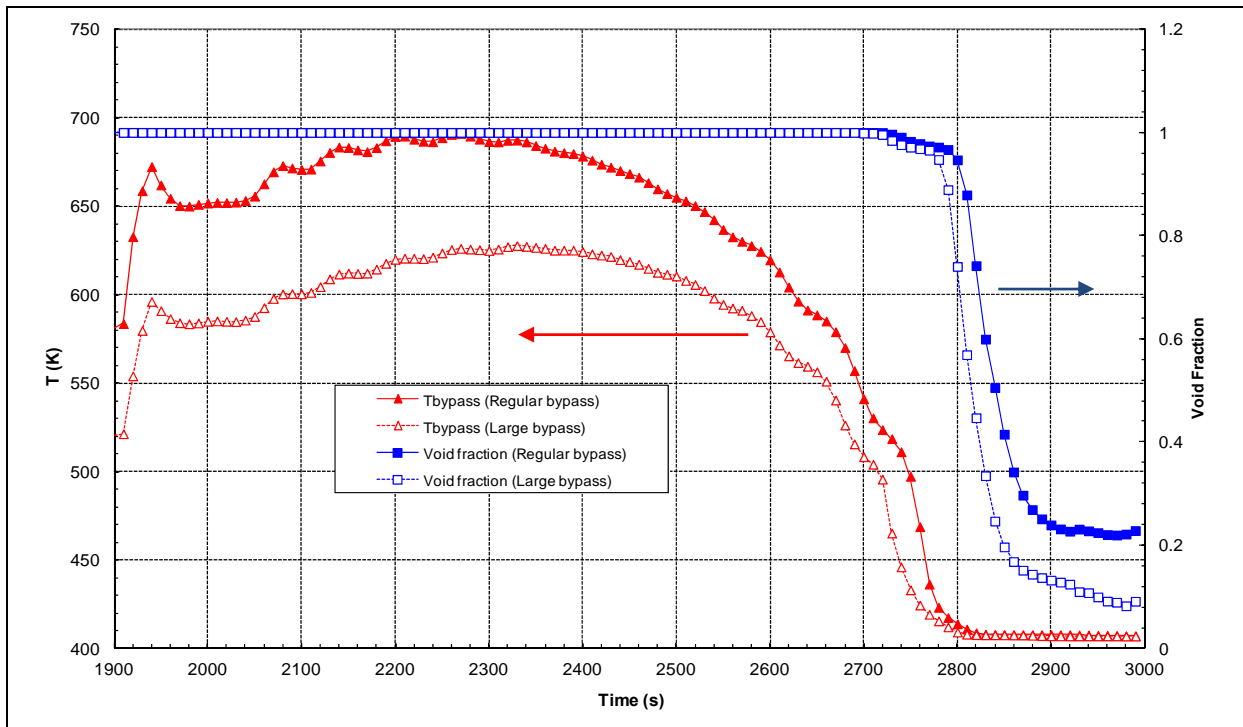


Figure 3.19: Flow rate = 5 m/h; Evolution vs. time of the bypass outer side temperature and void fraction, at the top of the debris bed

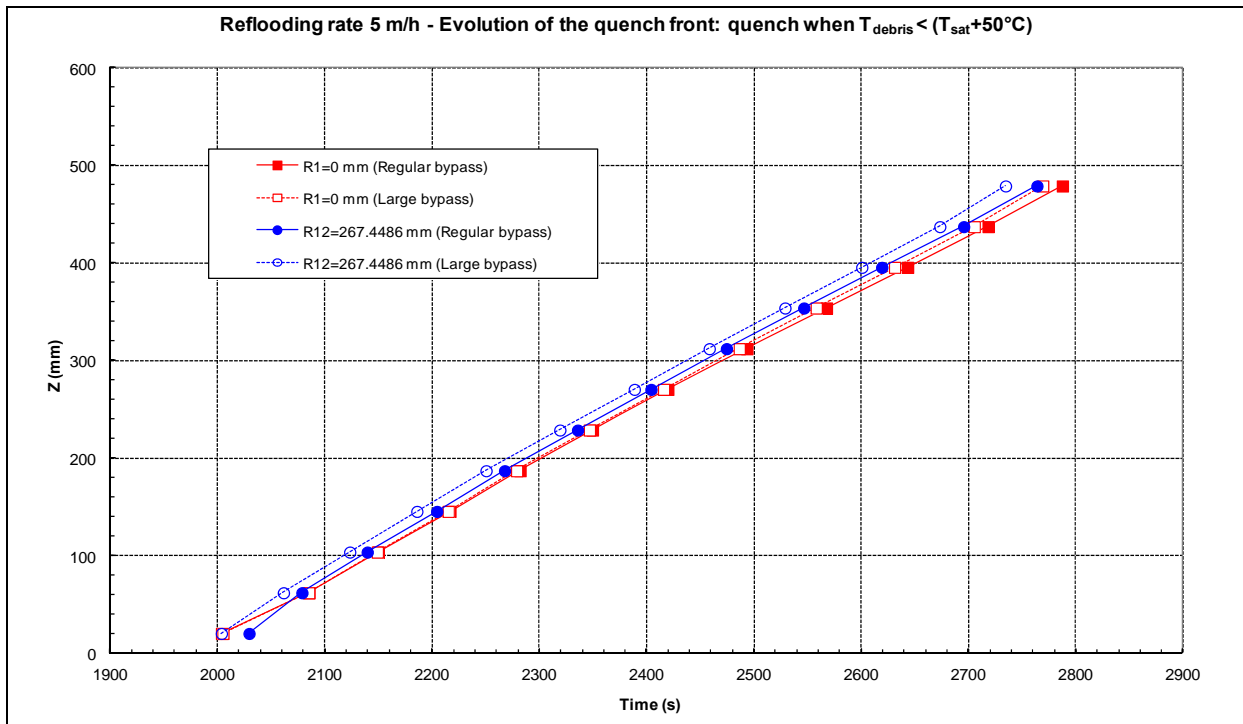


Figure 3.20: Flow rate = 5 m/h; Quenching front axial level vs. time (heated debris bed center and bypass outer side)

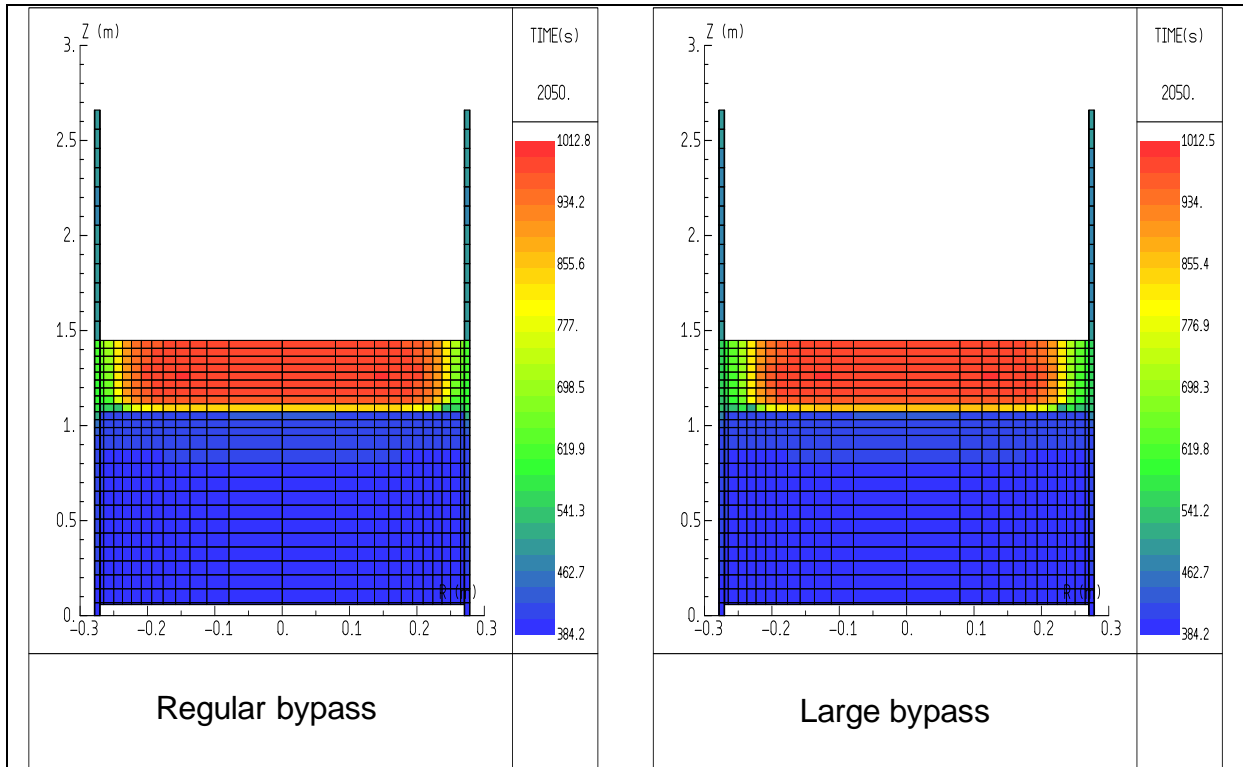


Figure 3.21: Flow rate = 10 m/h; Temperature distribution at 2050 s

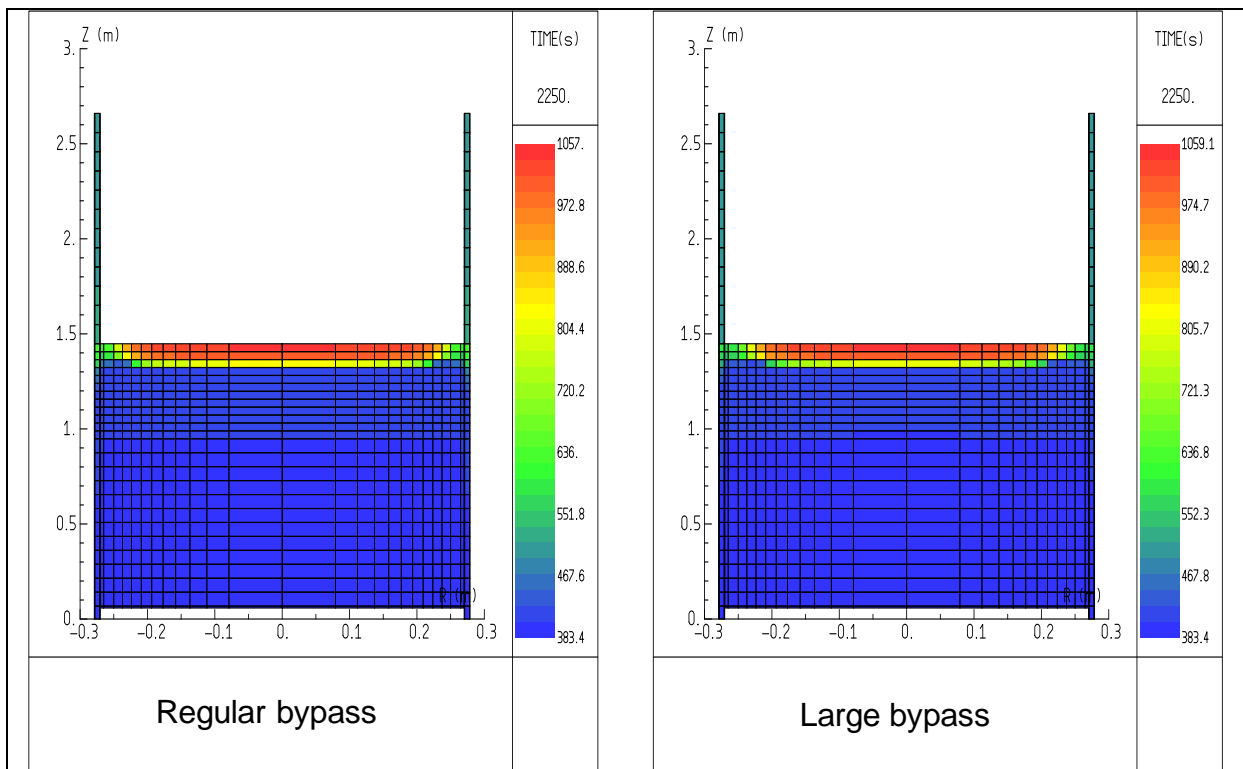


Figure 3.22: Flow rate = 10 m/h; Temperature distribution at 2250 s

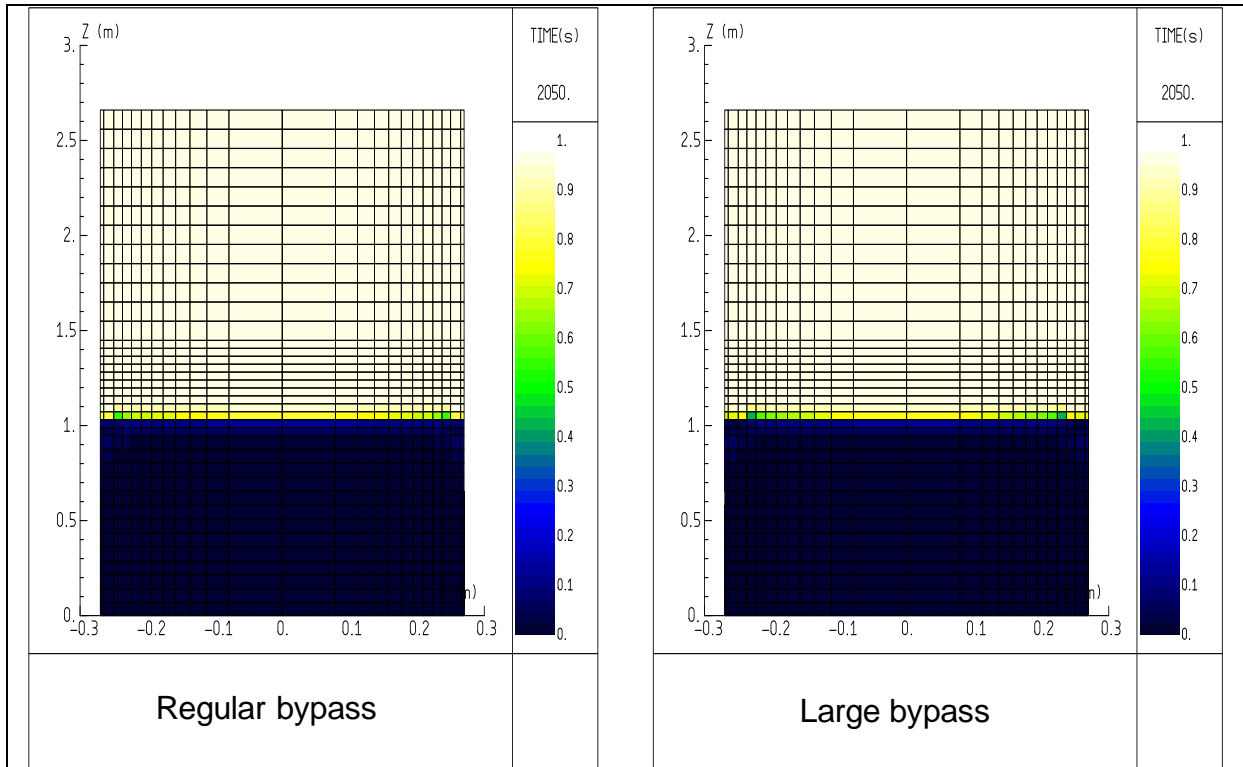


Figure 3.23: Flow rate = 10 m/h; Void fraction distribution at 2050 s

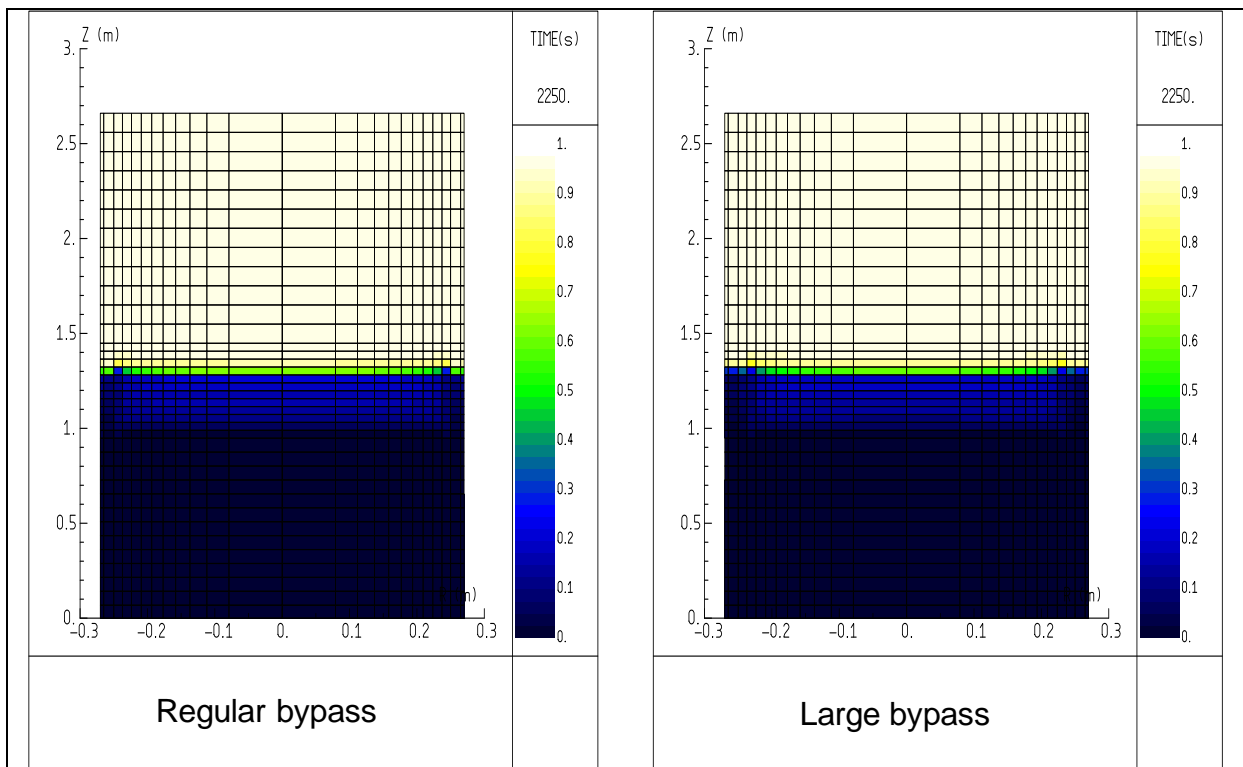


Figure 3.24: Flow rate = 10 m/h; Void fraction distribution at 2250 s

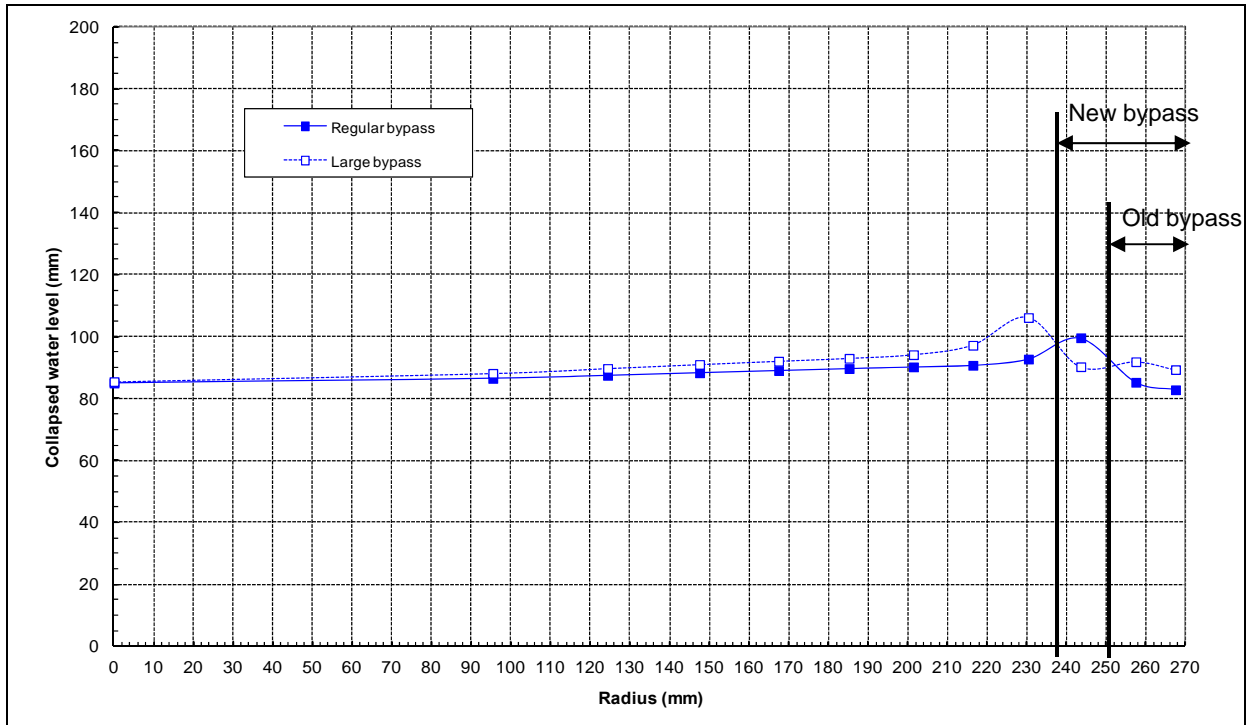


Figure 3.25: Flow rate = 10 m/h; Collapsed water level radial profile at 2050 s

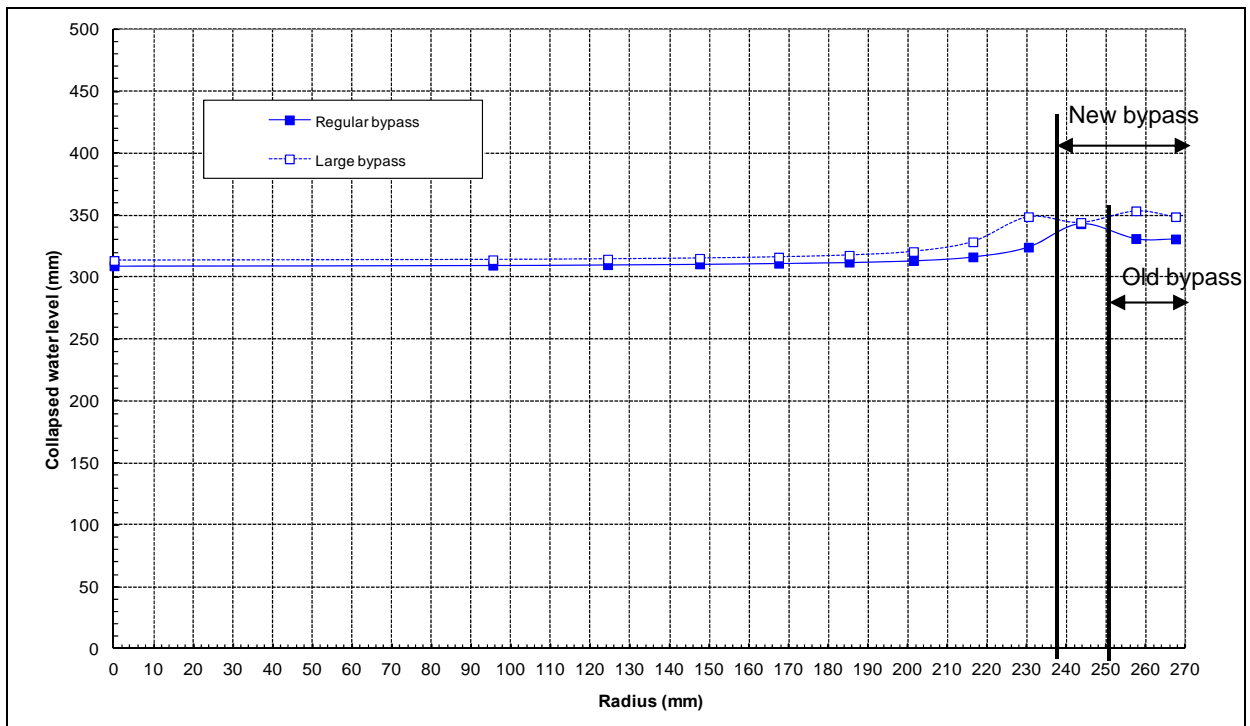


Figure 3.26: Flow rate = 10 m/h; Collapsed water level radial profile at 2250 s

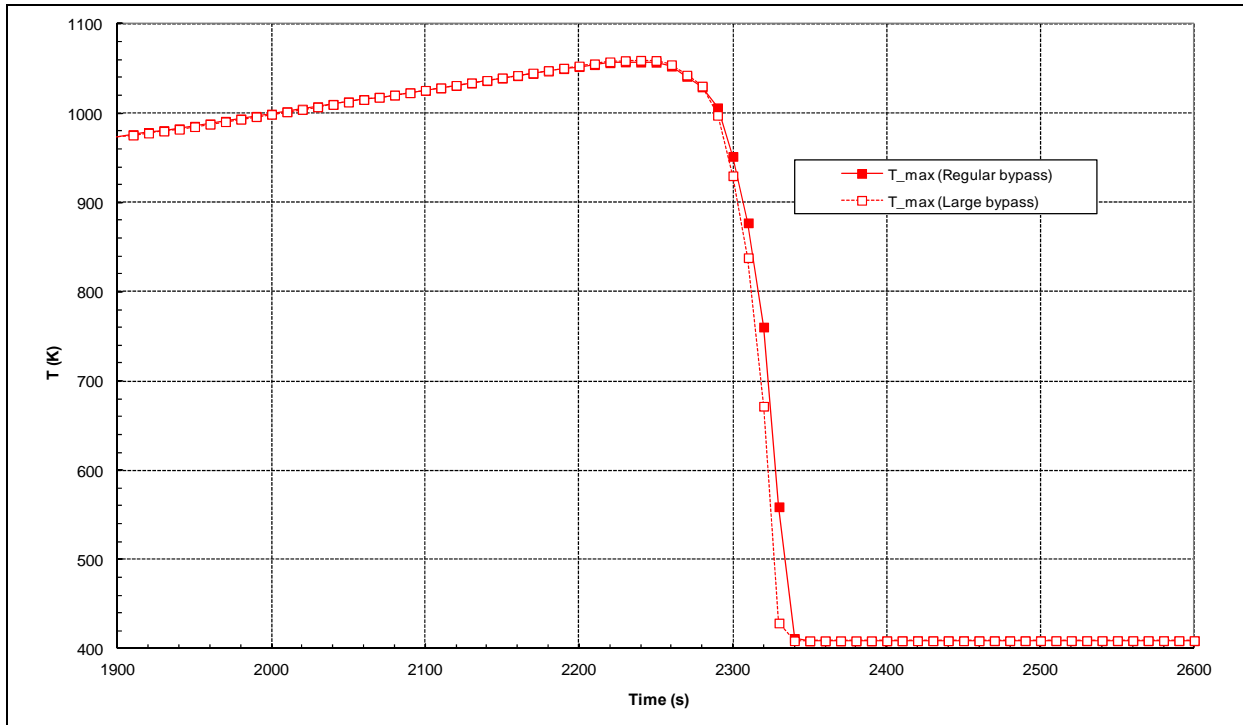


Figure 3.27: Flow rate = 10 m/h; Evolution vs. time of the maximum debris bed temperature

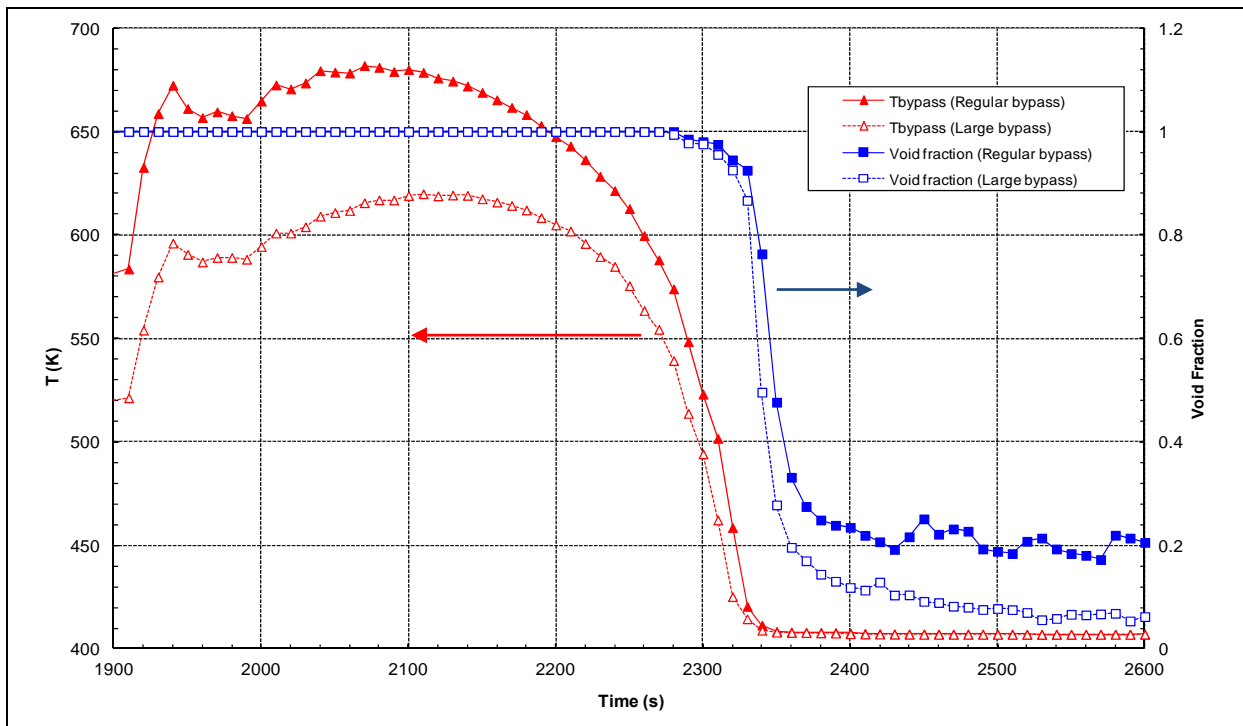


Figure 3.28: Flow rate = 10 m/h; Evolution vs. time of the bypass outer side temperature and void fraction, at the top of the debris bed

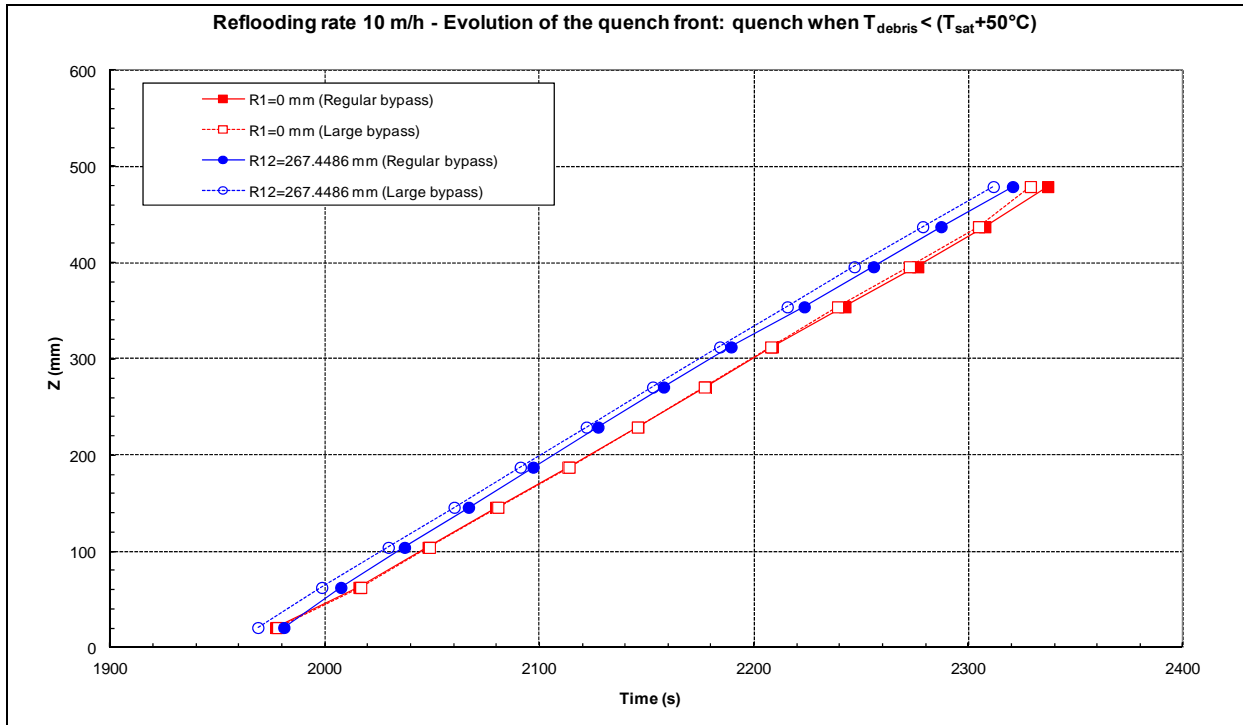


Figure 3.29: Flow rate = 10 m/h; Quenching front axial level vs. time (heated debris bed center and bypass outer side)

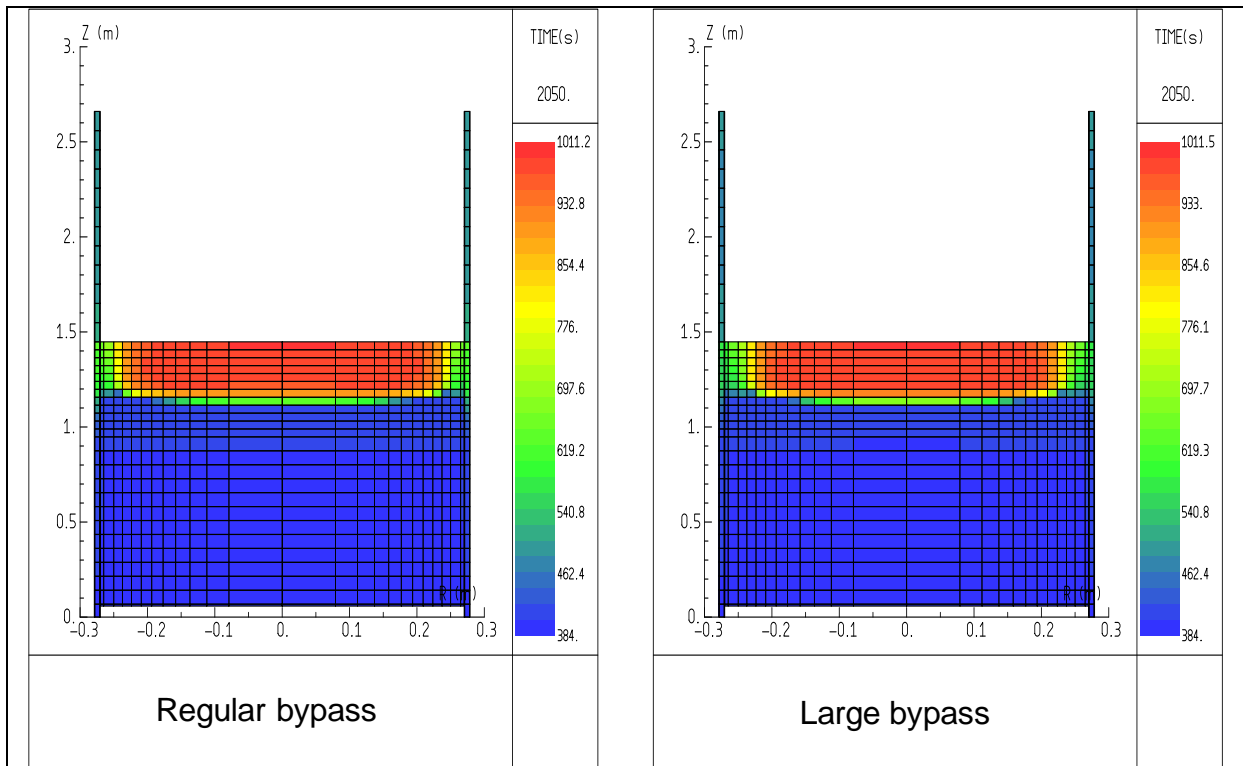


Figure 3.30: Flow rate = 15 m/h; Temperature distribution at 2050 s

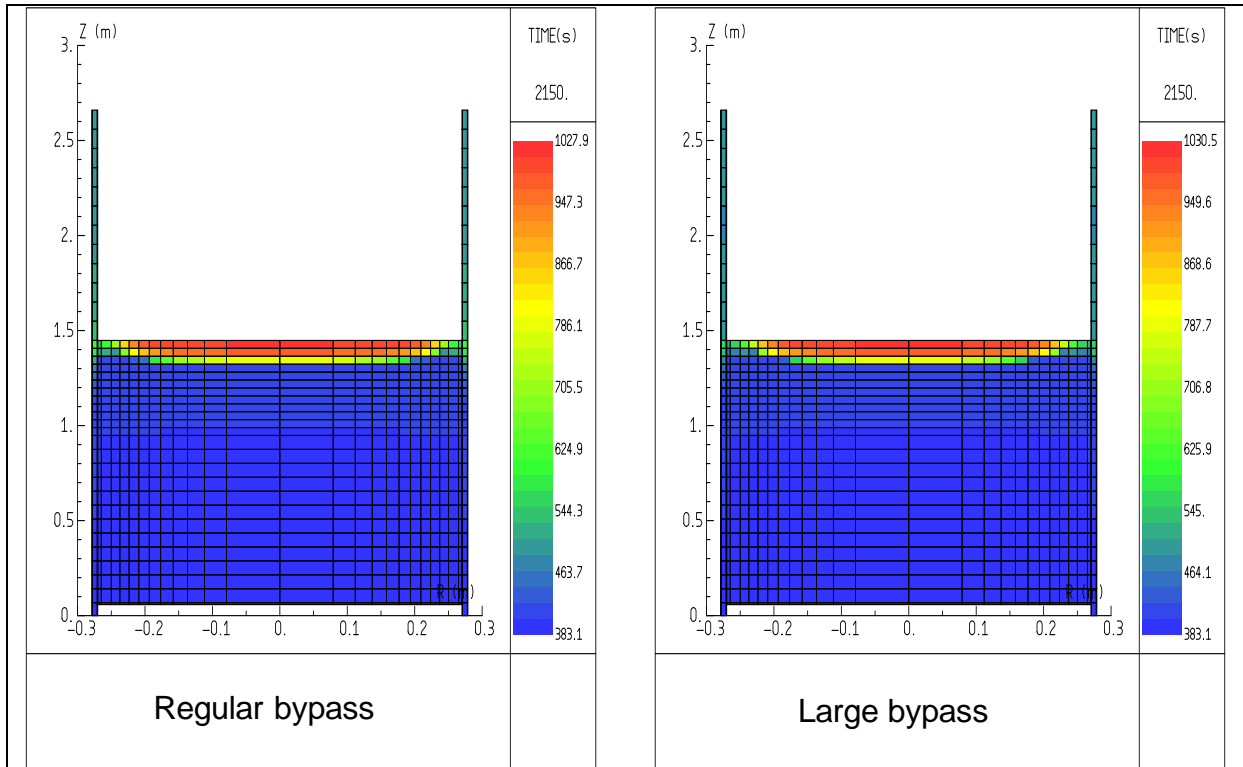


Figure 3.31: Flow rate = 15 m/h; Temperature distribution at 2150 s

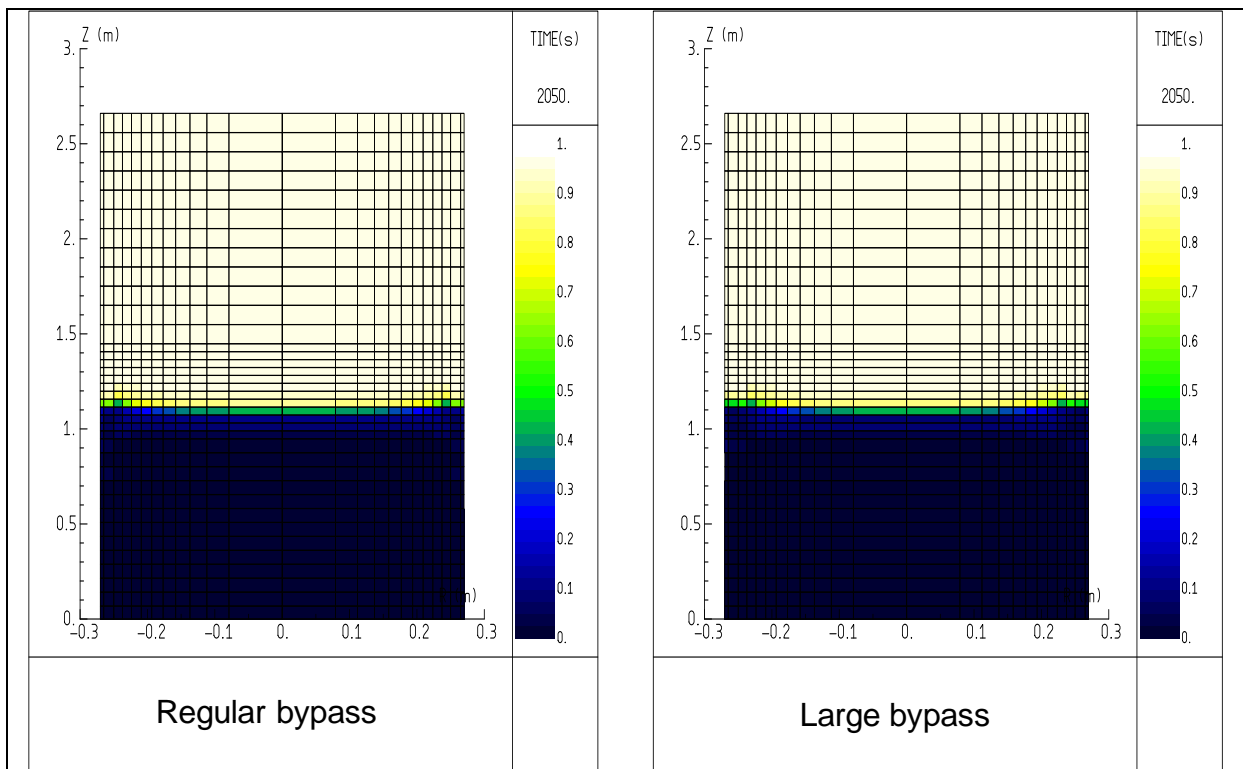


Figure 3.32: Flow rate = 15 m/h; Void fraction distribution at 2050 s

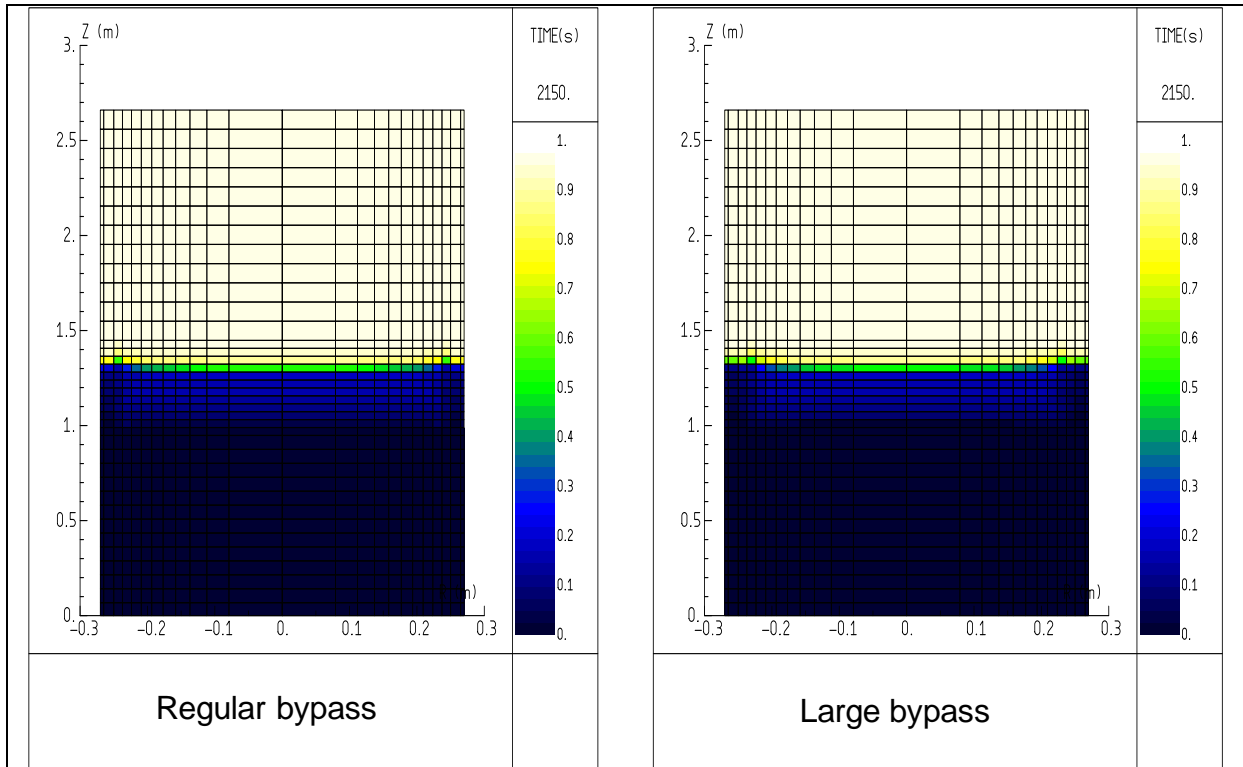


Figure 3.33: Flow rate = 15 m/h; Void fraction distribution at 2150 s

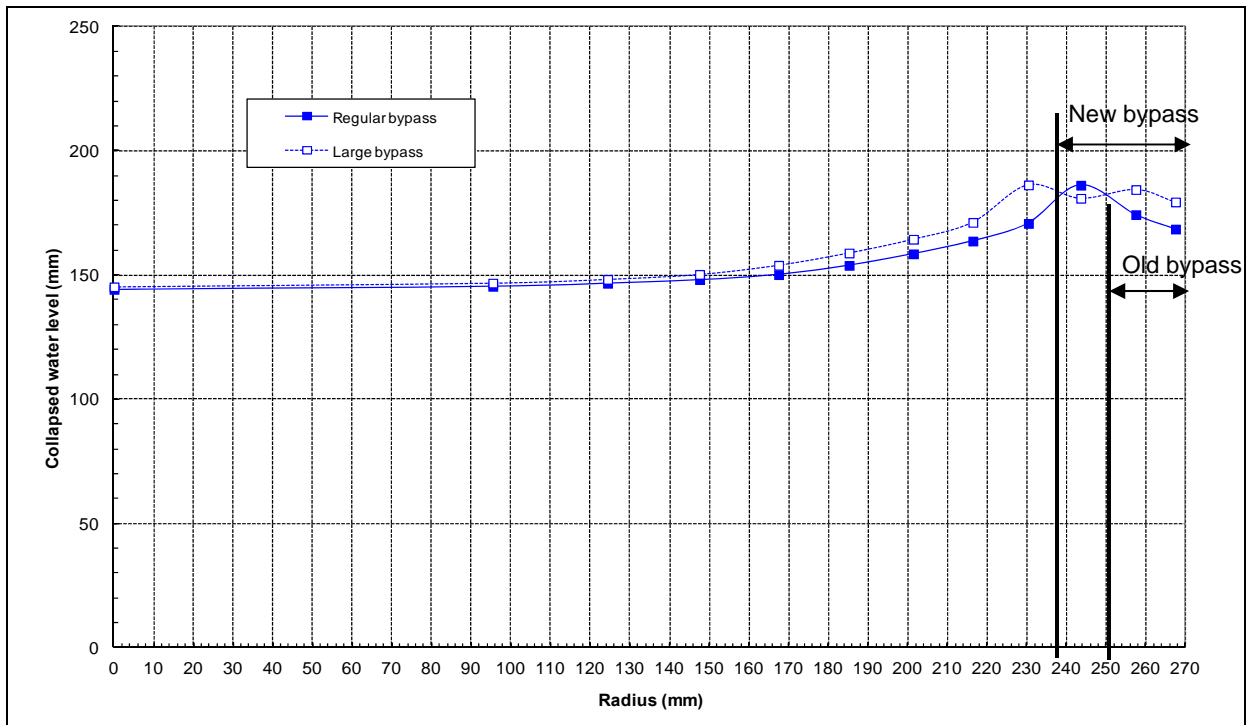


Figure 3.34: Flow rate = 15 m/h; Collapsed water level radial profile at 2050 s

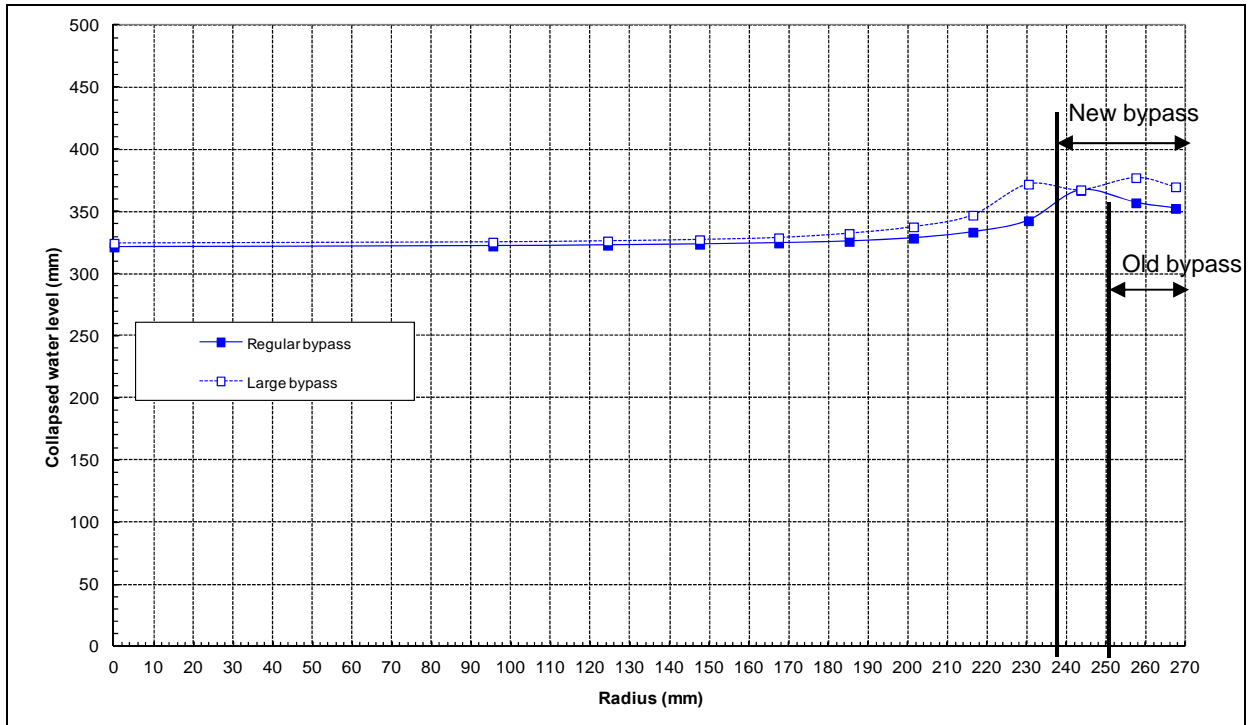


Figure 3.35: Flow rate = 15 m/h; Collapsed water level radial profile at 2150 s

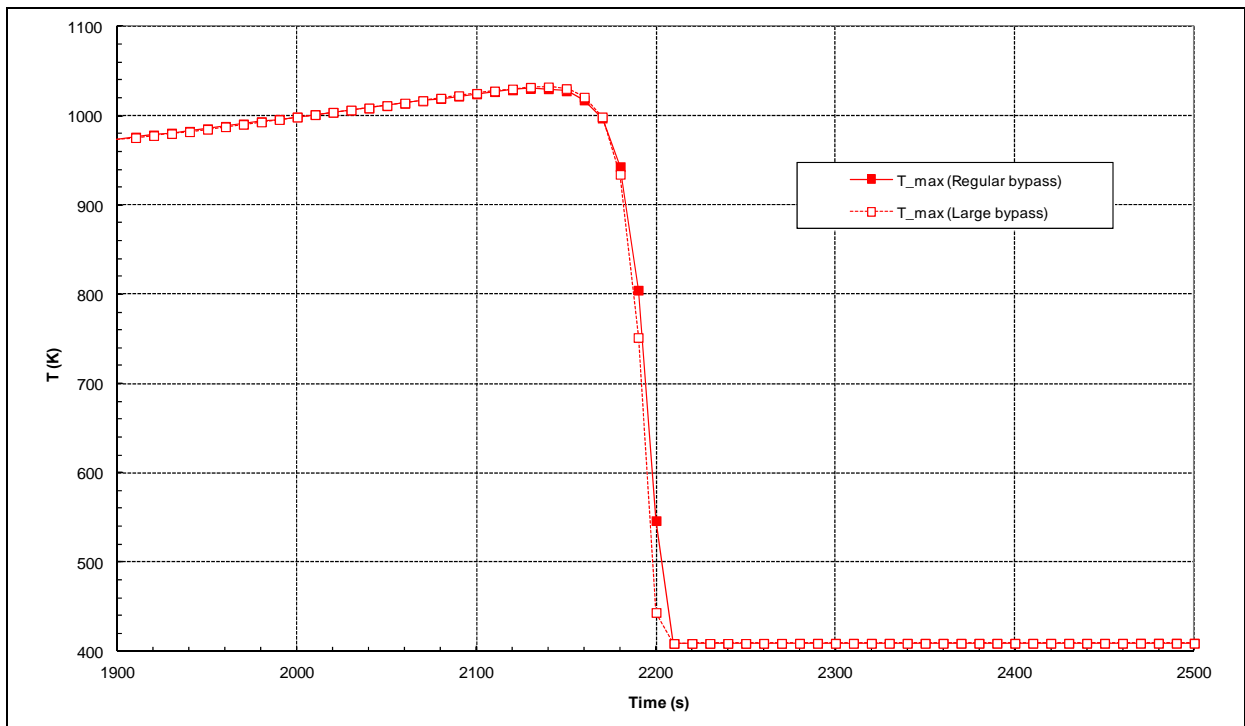


Figure 3.36: Flow rate = 15 m/h; Evolution vs. time of the maximum debris bed temperature

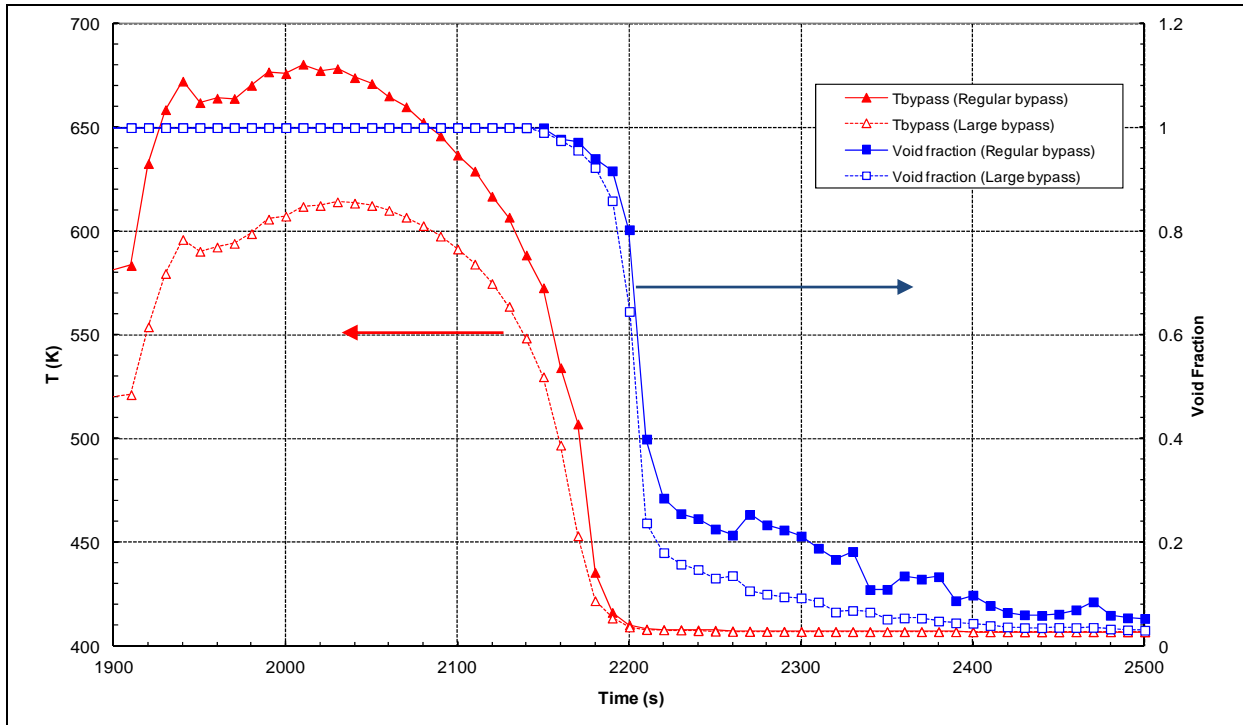


Figure 3.37: Flow rate = 15 m/h; Evolution vs. time of the bypass outer side temperature and void fraction, at the top of the debris bed

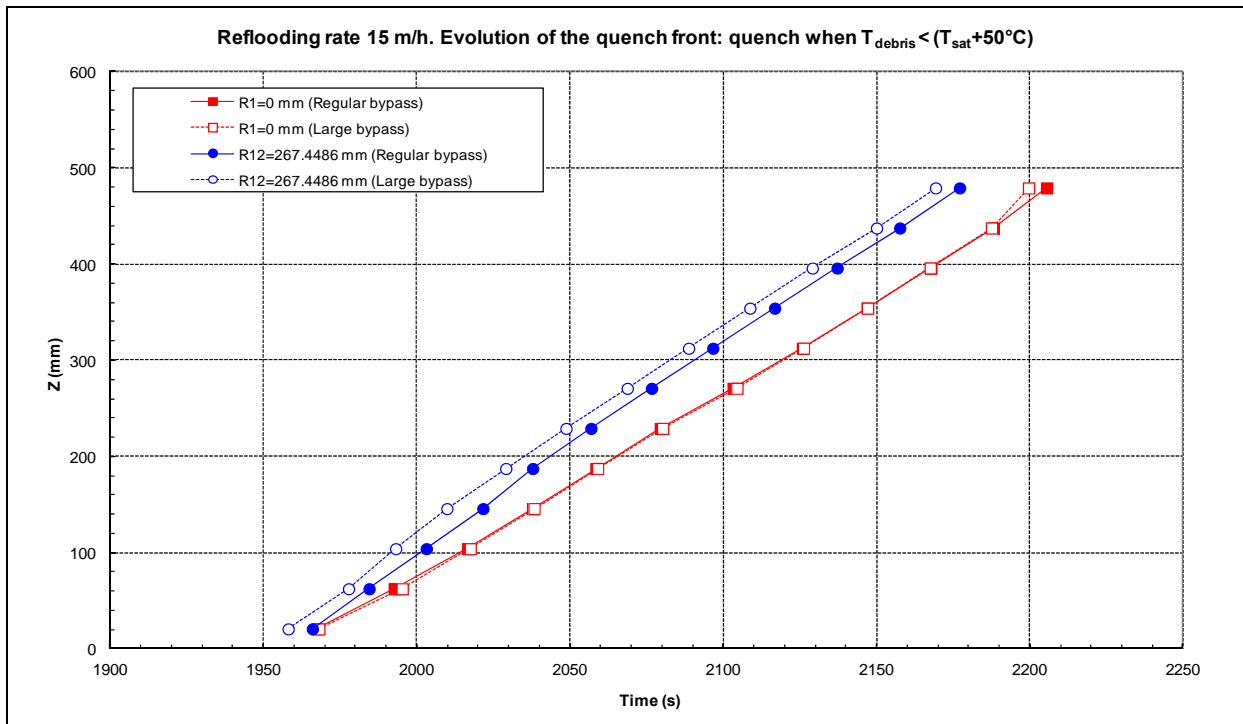


Figure 3.38: Flow rate = 15 m/h; Quenching front axial level vs. time (heated debris bed center and bypass outer side)

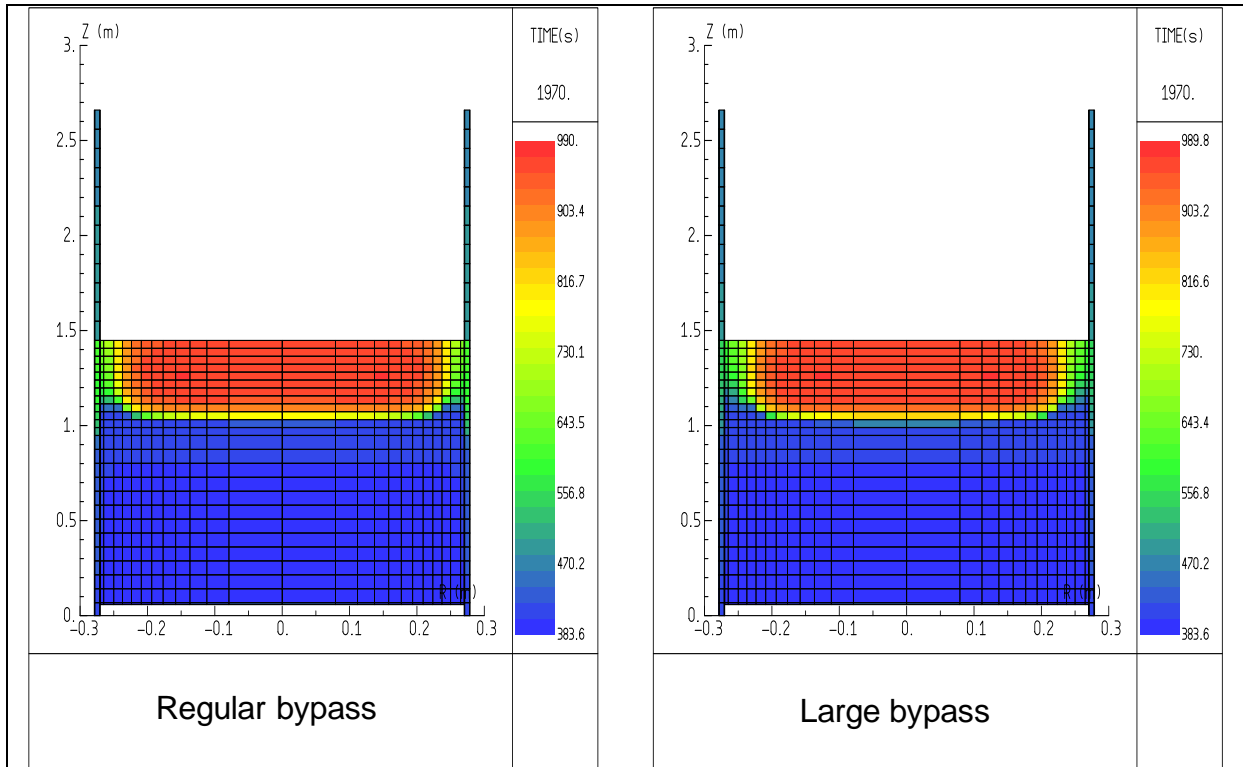


Figure 3.39: Flow rate = 30 m/h; Temperature distribution at 1970 s

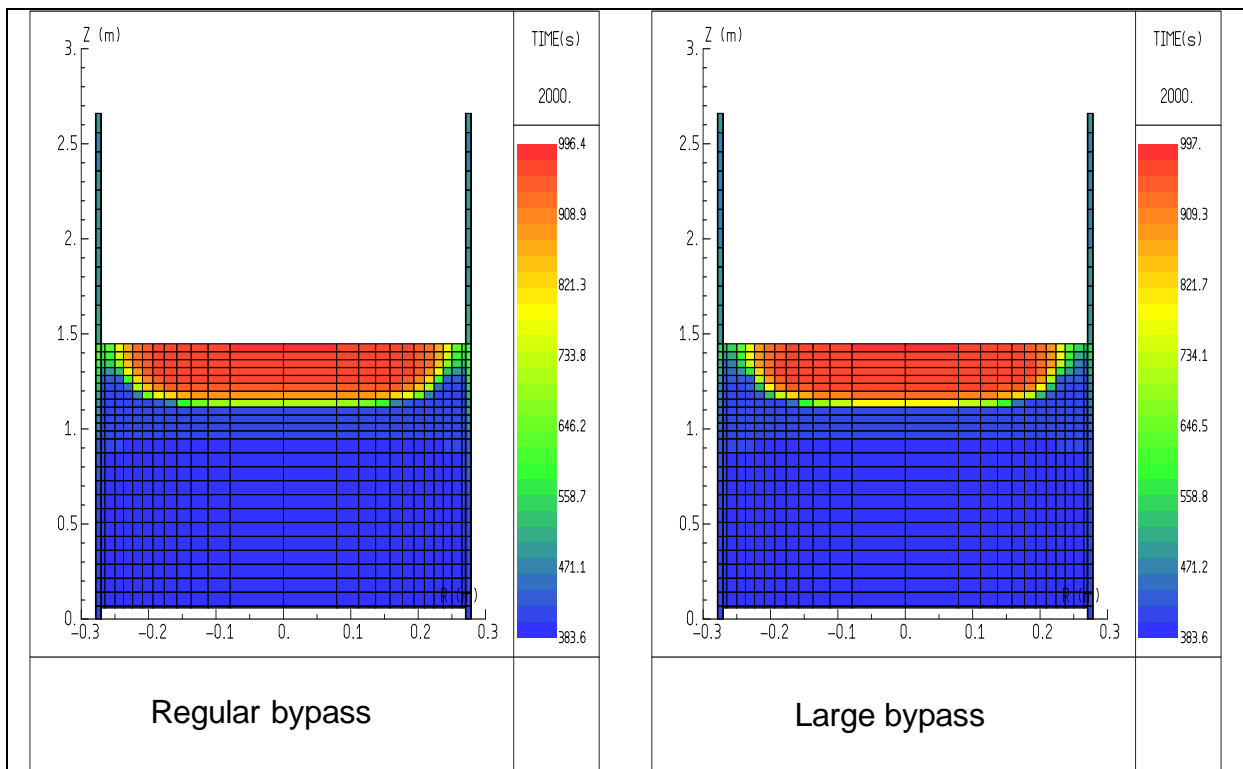


Figure 3.40: Flow rate = 30 m/h; Temperature distribution at 2000 s

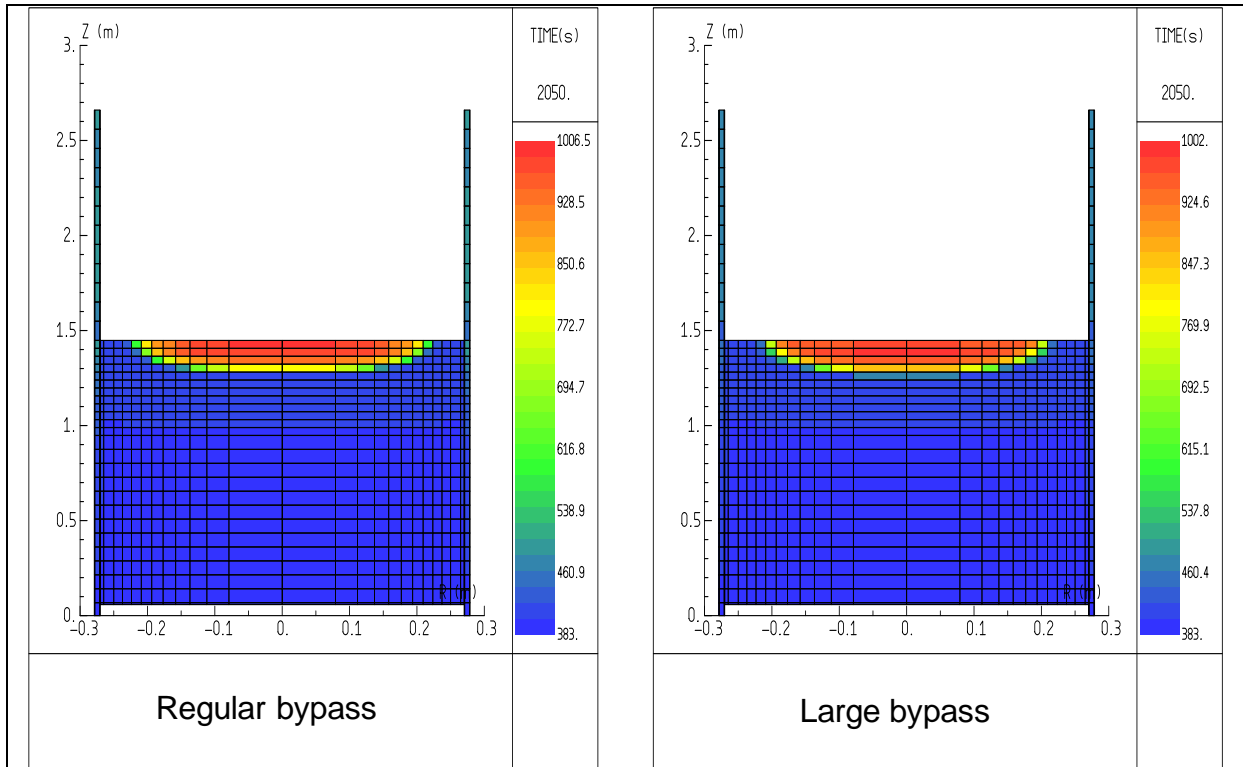


Figure 3.41: Flow rate = 30 m/h; Temperature distribution at 2050 s

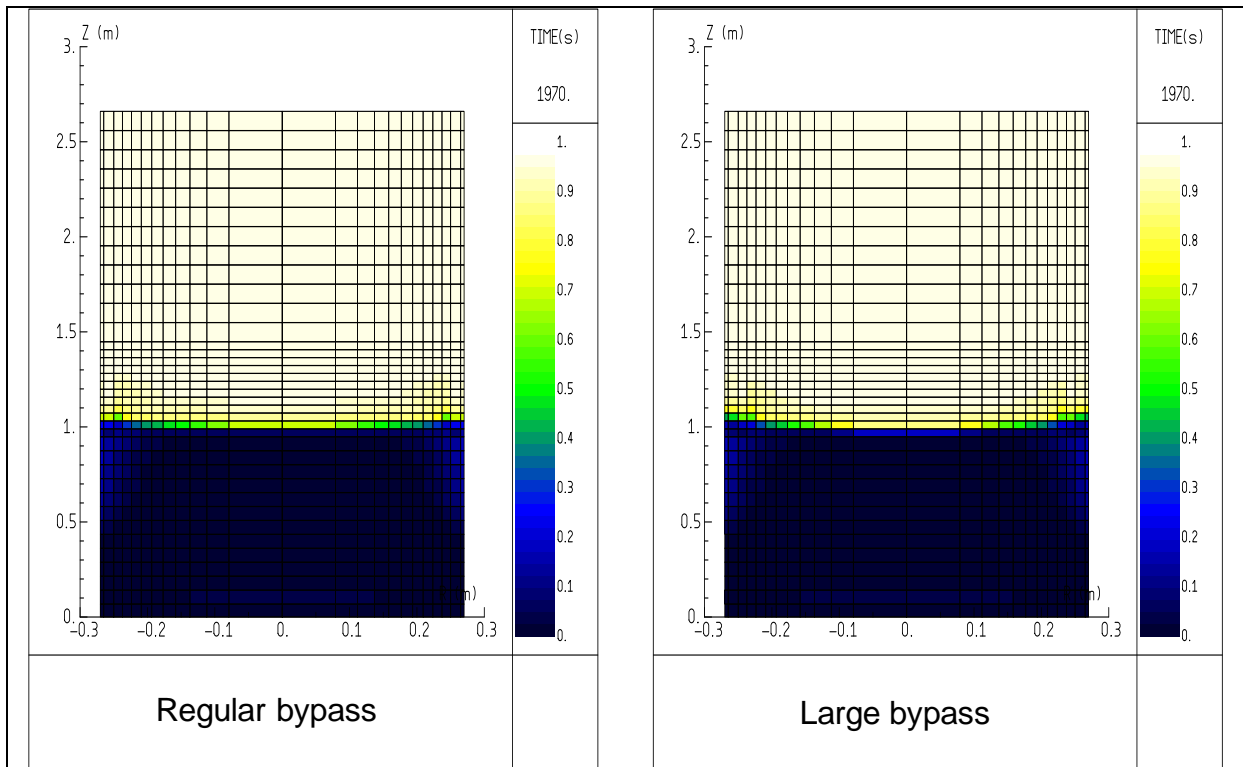


Figure 3.42: Flow rate = 30 m/h; Void fraction distribution at 1970 s

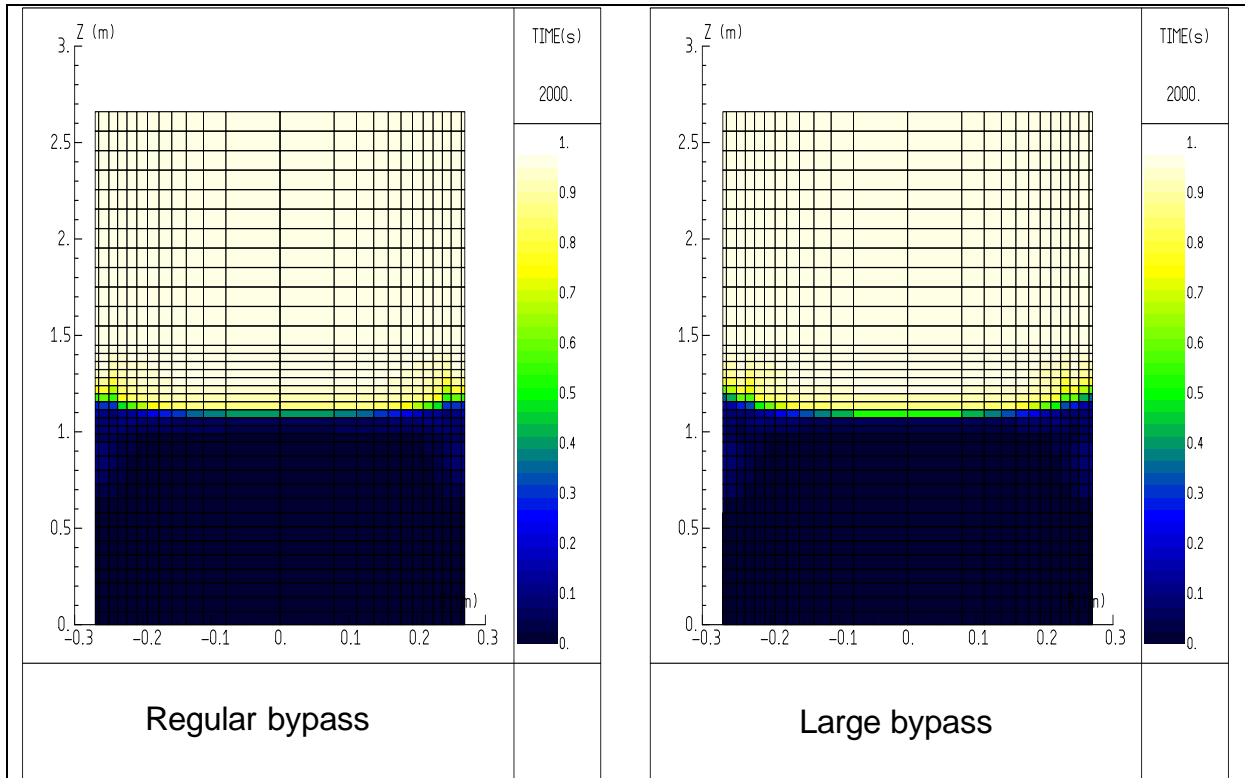


Figure 3.43: Flow rate = 30 m/h; Void fraction distribution at 2000 s

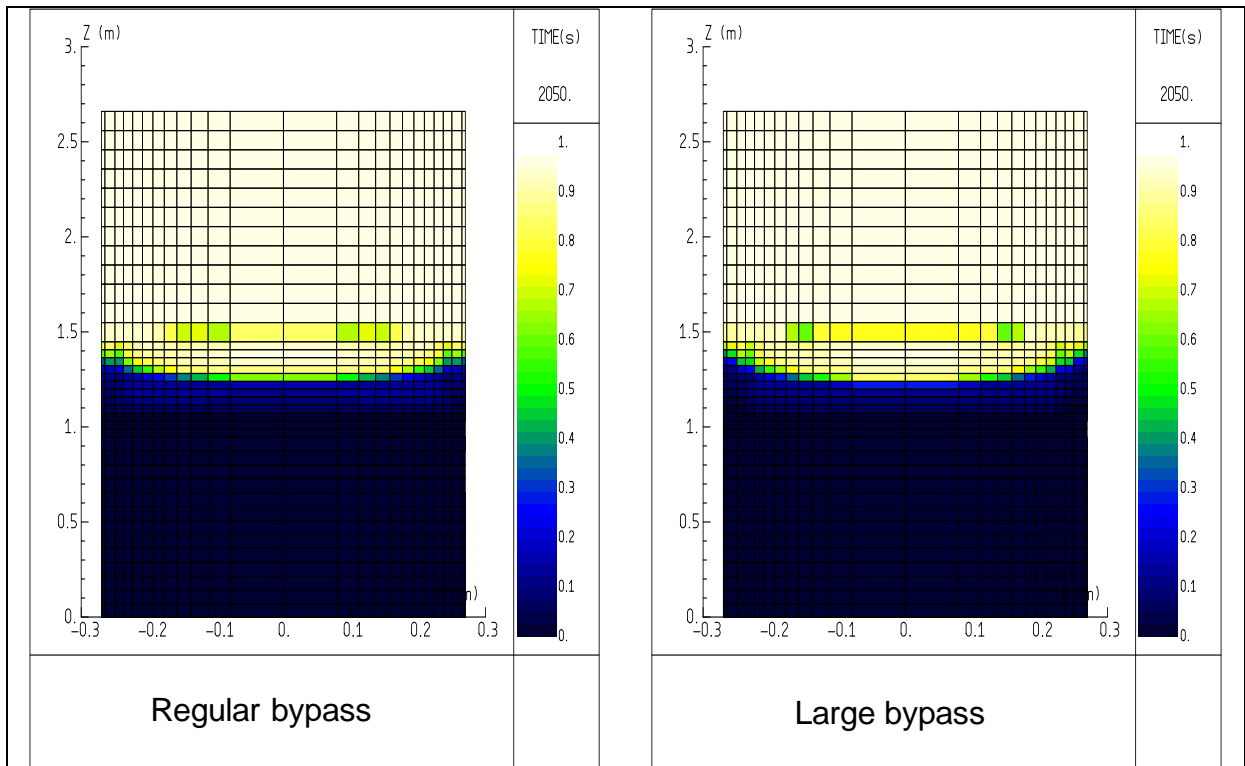


Figure 3.44: Flow rate = 30 m/h; Void fraction distribution at 2050 s

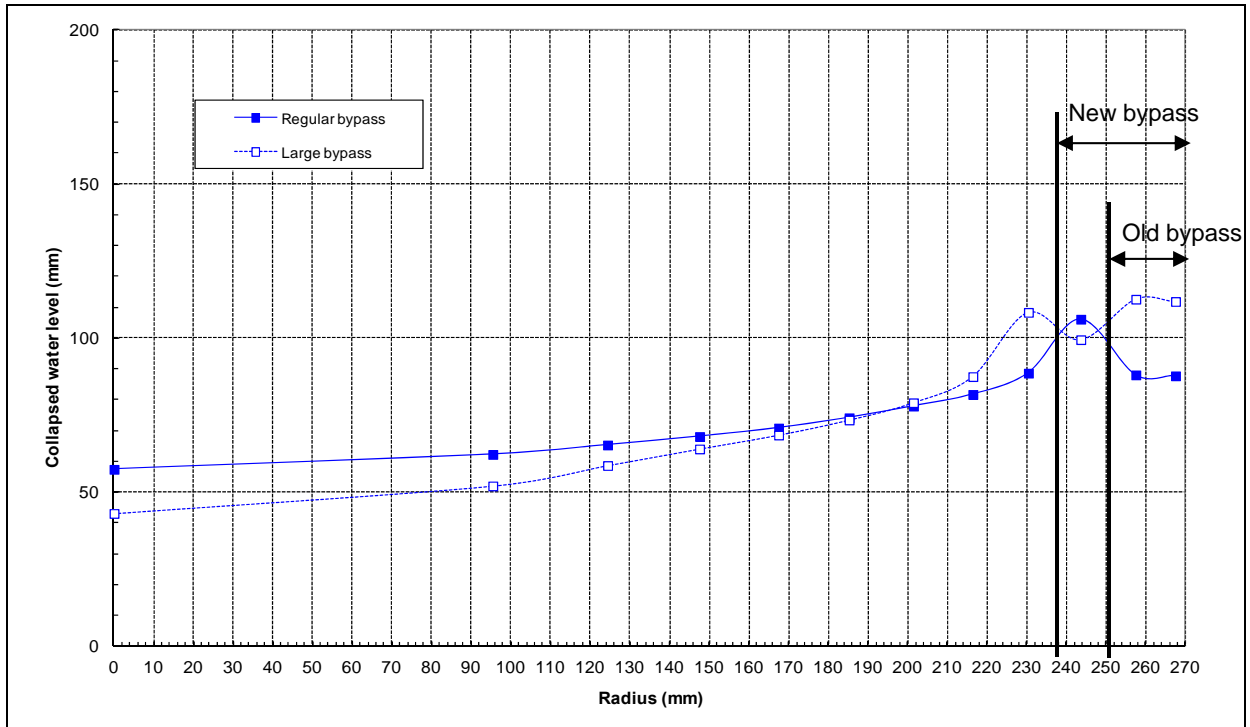


Figure 3.45: Flow rate = 30 m/h; Collapsed water level radial profile at 1970 s

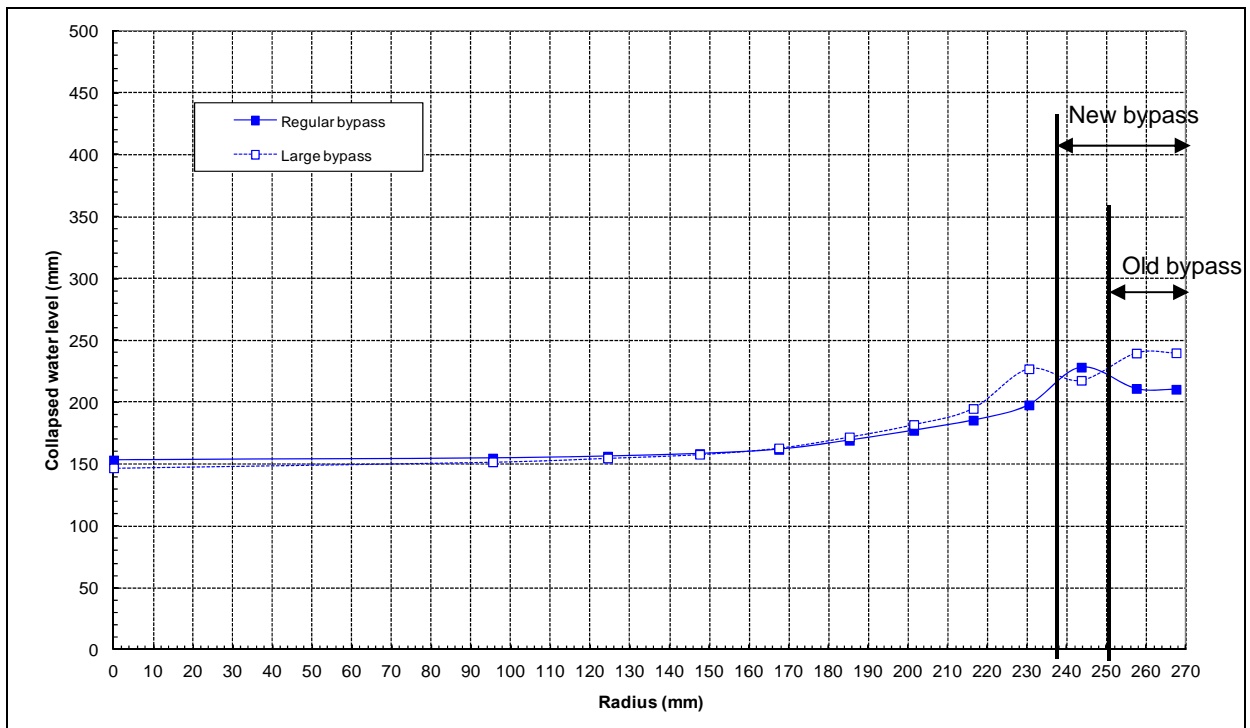


Figure 3.46: Flow rate = 30 m/h; Collapsed water level radial profile at 2000 s

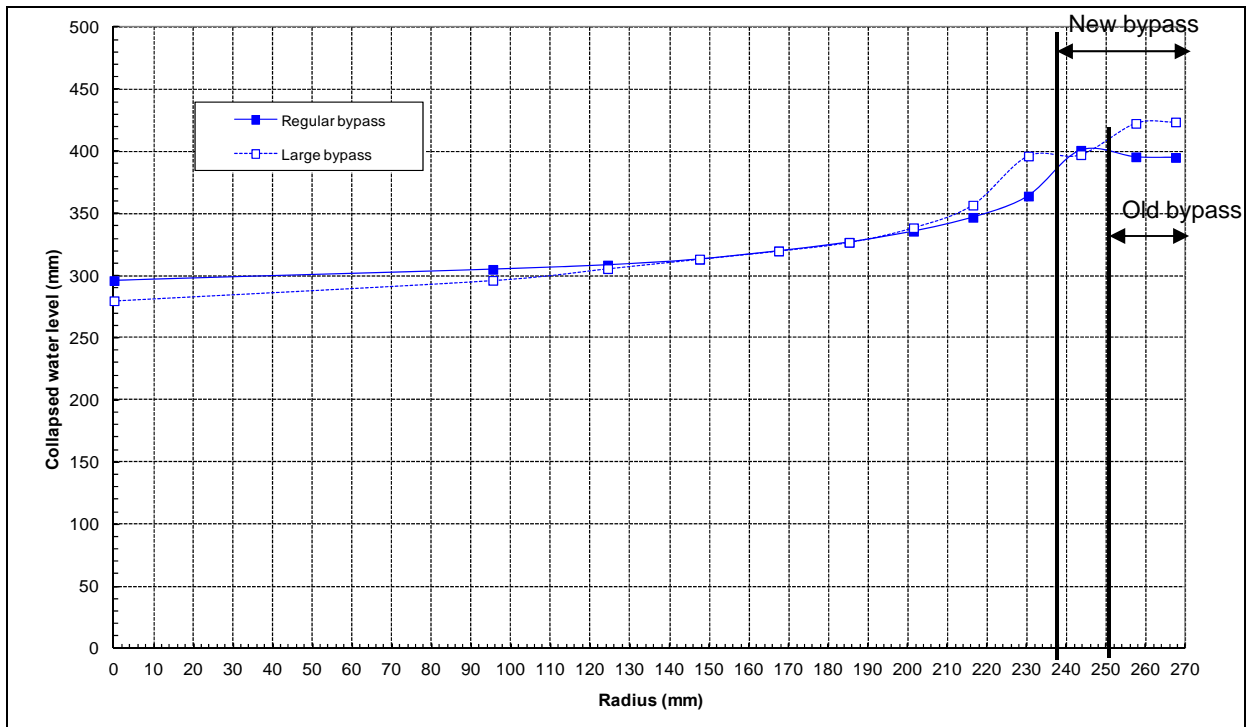


Figure 3.47: Flow rate = 30 m/h; Collapsed water level radial profile at 2050 s

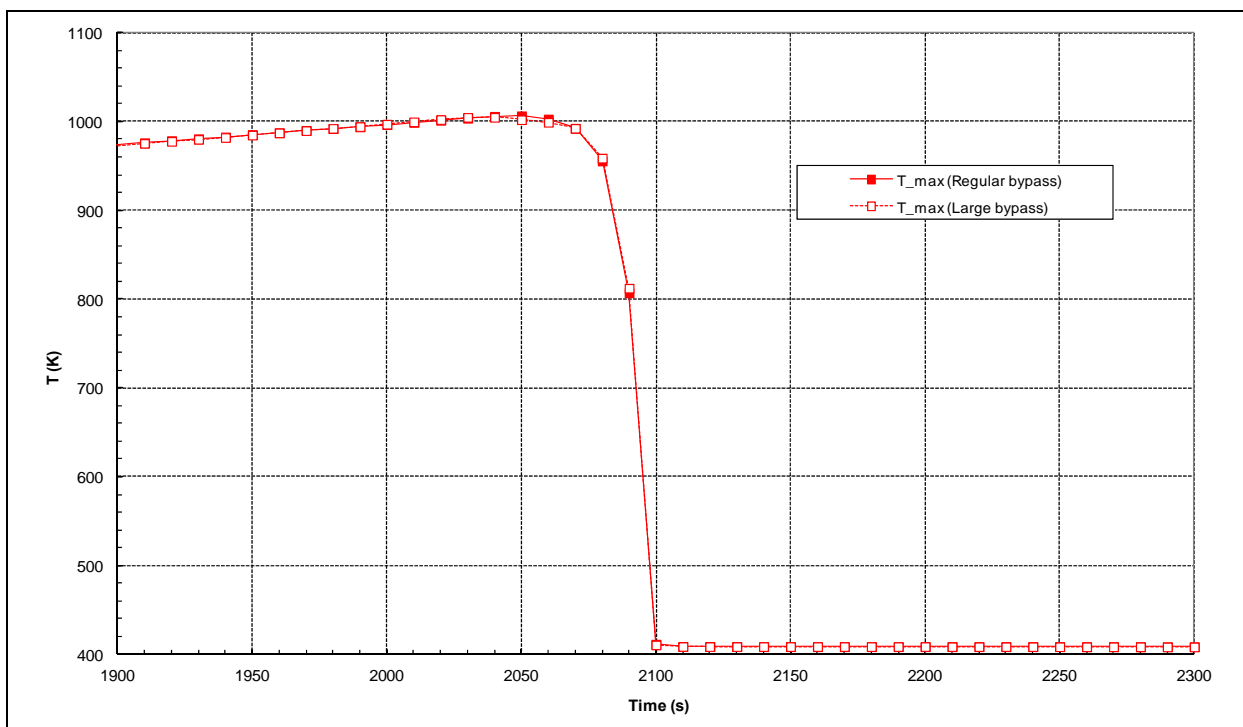


Figure 3.48: Flow rate = 30 m/h; Evolution vs. time of the maximum debris bed temperature

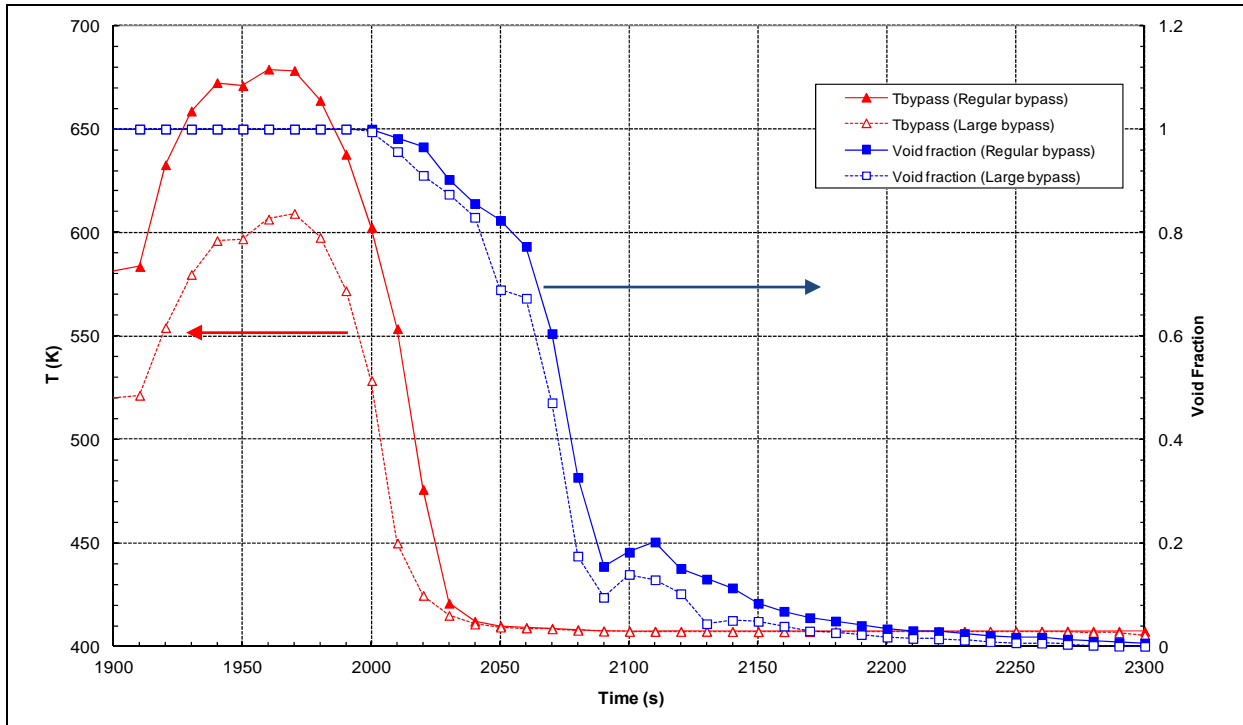


Figure 3.49: Flow rate = 30 m/h; Evolution vs. time of the bypass outer side temperature and void fraction, at the top of the debris bed

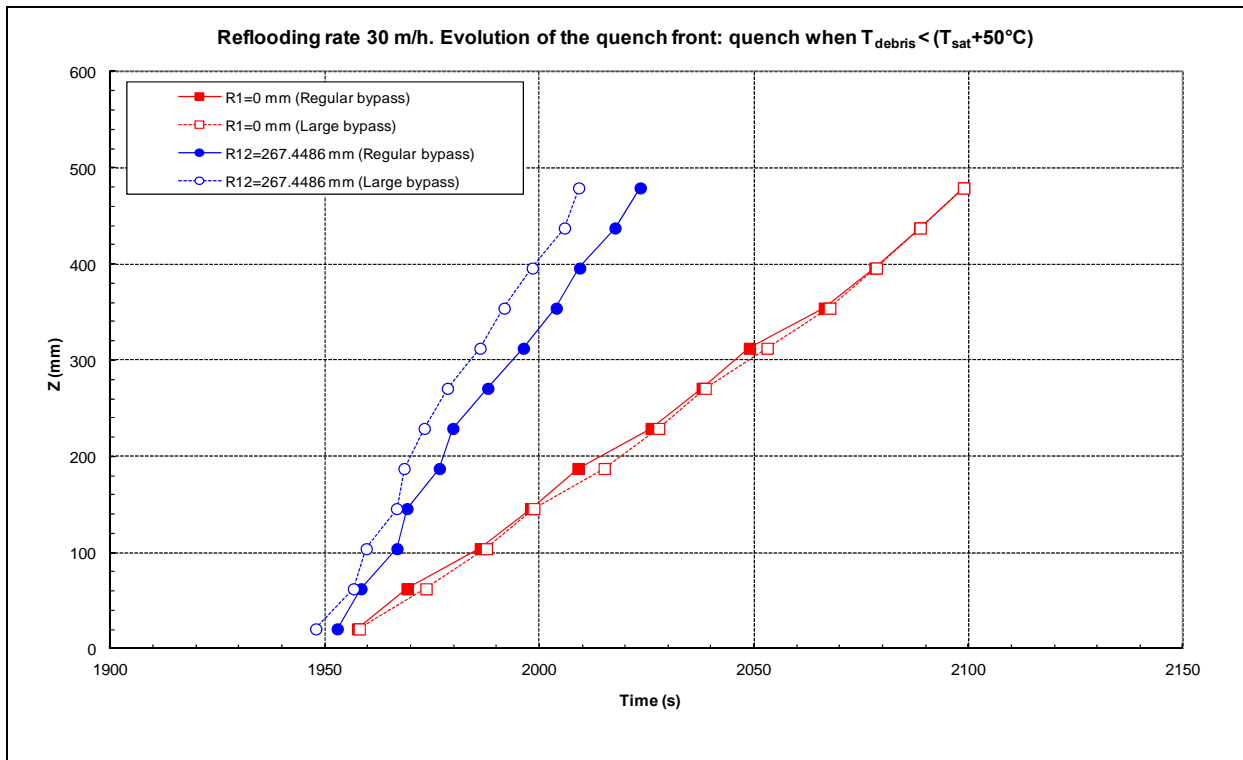



Figure 3.50: Flow rate = 30 m/h; Quenching front axial level vs. time (heated debris bed center and bypass outer side)

 Ricerca Sistema Elettrico	Sigla di identificazione	Rev.	Distrib.	Pag.	di
	ADPFISS-LP1-031	0	L	48	64

4. Calculation of degraded core reflooding scenarios in the TMI-2 plant with the ASTEC code

The work has been performed in the frame of ENEA participation in the Benchmark Exercise on TMI-2 plant promoted by the OECD/NEA/CSNI. The European integral code ASTEC V2.0R2, jointly developed by IRSN and GRS, has been employed in the analysis. After a brief description of the code models used and of the simulation of the TMI-2 plant, the main results of the reflooding scenarios during a Surge Line Break (SLB) severe accident sequence are presented and discussed. The main purpose of this analysis is to verify the robustness and the reliability of the ASTEC code under degraded core reflooding conditions during a severe accident.

4.1 Description of code models used

The European ASTEC V2.0R2 code is an integral code able to assess the whole severe accident sequence in a nuclear power plant, from the initiating event up to fission product release and behavior in the containment. The code includes several coupled modules that can deal with the different severe accident phenomena: thermal-hydraulics in the reactor system, core degradation and melt release, fission product release and transport, ex-vessel corium interaction, aerosols behavior and iodine chemistry in the containment, etc. Among them, the CESAR module is used to compute the thermal-hydraulics in the primary and secondary systems of the reactor. Such module is coupled to the ICARE2 module that computes core degradation, melt relocation and behavior in the lower head up to vessel failure.

The CESAR module allows a detailed representation of all components of primary and secondary circuits including auxiliary, emergency and control systems. CESAR is a two-phase flow thermal-hydraulic code. The gas phase can be a mixture of steam and hydrogen. The solution of the problem is based on two mass equations, two energy equations, one equation for steam velocity, and a drift flux correlation for water velocity. The state variables computed by CESAR are: total pressure, void fraction, steam and water temperature, steam and water velocity, and partial pressure of hydrogen. All hydraulics components can be discretized by volumes (one mesh) or axial meshed volumes and connected by junctions. The volumes can be homogeneous or with a swollen level. Thermal structures are used to model the walls of the components, and compute thermal heat exchange between primary and secondary systems and heat losses to the environment.

The ICARE2 module can simulate the thermal-hydraulics in the part of the vessel below the top of the core: downcomer, lower plenum and the core itself including the core bypass. The model of the lower head of ICARE2 has one single mesh for fluids, three layers for corium (pool, metal and debris), and a 2D meshing for the vessel. The ICARE2 module is activated to compute core heatup and degradation, in coupled mode with CESAR, at the onset of core uncovering. Before ICARE2 activation, the thermal-hydraulics in the vessel and the core is computed by CESAR through an automatic vessel model creation based on ICARE2 input deck. The convective and radiative heat exchanges between core components and structures

are computed by ICARE2. Most important core degradation phenomena are dealt with in ICARE2 including: (1) core material oxidation and hydrogen generation, (2) control rod material interaction, melting and relocation, (3) zircaloy clad melting and fuel dissolution, (4) fuel rod clad failure and metallic melt relocation, (5) debris bed and molten pool formation and spreading in the late degradation phase.

The ASTEC calculations have been performed applying core degradation parameters according to best code practice guidelines and the experience gained in the analysis of real TMI-2 accident scenario. The value of code parameters and modelling options relevant to core degradation are presented in Table 4.1.

Table 4.1: ASTEC core degradation parameters and modelling options

Parameter	ASTEC	Reference
Zircaloy oxidation kinetics	Best-fit of ASTEC code: - Cathcart-Pawel (low temp. range) - Prater-Courtright (high temp. range)	Recommended value of ASTEC code
Cladding failure criteria (T = clad temperature) (e = ZrO ₂ layer thick.)	- T > 2300 K and e < 0.3 mm - T > 2500 K	Standard values in ASTEC applications for steam rich oxidation environment
Melting temperature of oxide (UO ₂ and ZrO ₂)	2550 K	Interpretation of Phebus FP tests
Debris bed formation criteria	2500 K	Fuel rod clad dislocation
Debris bed porosity and particle size	- Porosity = 40%, - Size = 3 mm	- Default value of ASTEC - Mean size of TMI-2 debris
Core slumping	Baffle melting (relocation through core by-pass) or melting at core bottom (relocation through core support plate)	
RPV failure	Vessel wall melting (100%)	Fusion criterion in ASTEC

4.2 TMI-2 plant and core nodalization

The TMI-2 plant nodalization scheme is shown in Figure 4.1. The plant simulation includes a detailed modelling of the primary coolant system with:

- the reactor pressure vessel volumes and structures, including the VENT valve between the cold collector and the hot collector;

- the two primary coolant loops (1 hot leg and 2 cold legs in each loop) with once-through steam generators and main coolant pumps;
- the pressurizer with surge-line, PORV, heaters, spray-line and valve;
- the external walls of the primary circuit;
- main emergency and control systems.

Modelling of the secondary systems is limited to the secondary side of steam generators, the steam lines with isolation valves, and main feedwater and auxiliary feedwater injections.

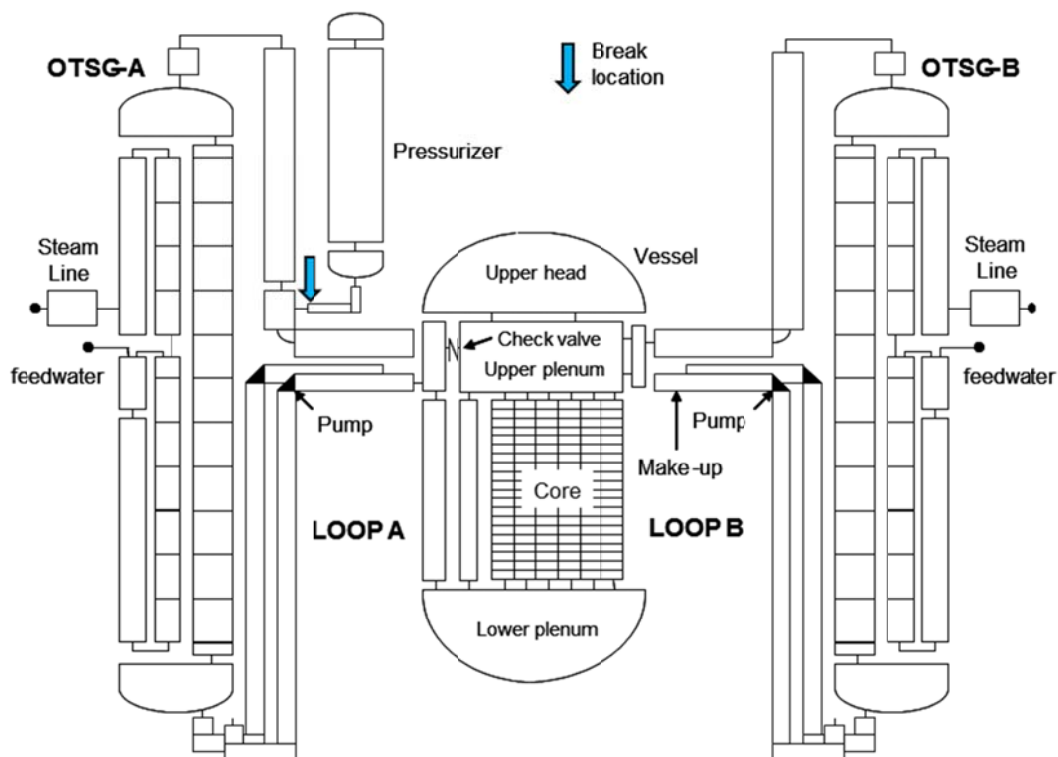


Figure 4.1: TMI-2 plant nodalization scheme

The core is represented by 6 radial rings plus the by-pass, and axially discretized in 20 equal meshes. The core baffle, the barrel and the thermal shield at the core periphery are also represented. One representative fuel rod component and one control rod component are modelled in each core ring. The control rod component simulates all the full and part-length control rods, all the guide tubes (including those containing burnable poison rods) and all the instrument tubes.

4.3 TMI-2 plant initial conditions

The TMI-2 plant state at transient initiation (initial conditions at $t = 0$) is obtained by a steady-state code run lasting 2000 s and starting from plant thermal-hydraulic parameter values close to the ones specified for TMI-2. During the steady-state calculation, some


regulations on the primary and secondary sides are activated to facilitate the achievement of stable conditions, as close as possible to the initial TMI-2 plant state defined in the benchmark specifications. The regulated parameters are:

- The pressurizer pressure by turning on/off the heaters in the bottom pressurizer volume and the spray in the pressurizer top volume;
- The pressurizer liquid mass, by water injection or draining, in order to obtain the precise liquid level;
- The feedwater mass flowrate at the steam generator downcomer inlet according to the steam mass flowrate at the steam generator outlet;
- The primary loop mass flowrate varying the pump rotation speed.

The TMI-2 plant initial conditions calculated by ASTEC are compared with TMI-2 benchmark specification data in Table 4.2. The primary circuit conditions show a very good agreement with the plant data. The largest discrepancy is on the steam temperature at the steam generator outlet, which is under predicted by 5 °C. This deviation leads to an overestimation of the feedwater flow rate at the steam generator inlet of about 1.5%, in order to match the right steam generator power removal.

Table 4.2: Initial conditions for TMI-2 calculations

Parameter	Unit	ASTEC	TMI-2
Primary System			
Reactor Power	MW	2772	2772
Pressurizer pressure (dome)	MPa	14.94	14.96
Temperature Hot Leg A/B	K	591.3	591.15
Temperature Cold Leg A/B	K	563.6	564.15
Mass Flow Rate - Loop A/B	kg/s	8800	8800
Pressurizer level	m	5.588	5.588
Total primary mass	kg	222392	222808
Secondary System			
Pressure SG A/B	MPa	6.41	6.41
Steam temperature SG A/B	K	567.0	572.15
Riser collapsed level SG A/B	m	3.21	3.28 - 4.03
Liquid mass SG A/B	kg	16782	13140-19210
Feedwater flow SG A/B	kg/s	772.1	761.1
SG feedwater temperature	K	511.15	511.15

 Ricerca Sistema Elettrico	Sigla di identificazione	Rev.	Distrib.	Pag.	di
	ADPFISS-LP1-031	0	L	52	64

4.4 SLB sequence and reflooding scenarios

The SLB severe accident sequence has been simulated by the double ended guillotine break (DEGB) of the surge line in conjunction with the simultaneous and temporary loss of offsite power supply (station blackout at $t = 0$ s). The loss of offsite power leads to immediate reactor scram, primary pump coastdown, and turbine and feedwater trip on the secondary side without auxiliary feedwater start-up. The large primary coolant leakage started by the surge line break leads to quick depressurization of the primary system with rapid primary coolant inventory depletion. The High Pressure Injection (HPI) emergency coolant system is not actuated on demand and the Low Pressure Injection (LPI) emergency core cooling system is delayed after core uncover and heatup with significant core melting, in order to investigate the consequences of the reflooding of a degraded core.

In a first reflooding scenario, the core reflow is started from a slightly degraded core (degraded core mass equal to 10 tons), while in a second scenario the reflow is started from a highly degraded core, when the degraded core mass reaches 45 tons. In the second scenario the melting of the fuel rods is significant, and large debris bed regions and a molten pool are developed inside the core. The possibility to cooldown the degraded core is investigated by the start-up of LPI with a the nominal flow rate of 360 kg/s (90 kg/s in each one of the 4 cold legs). The injection is terminated after 1000 s from its initiation, according to the initial water inventory available in the LPI tank, and no recirculation from the sump is considered to continue the injection by the LPI system in the long term.

4.5 Analysis of results

The chronology of main events is presented in Table 4.3. The results of the two reflooding scenarios are compared with the ones of the base case scenario without LPI injection and then without core reflow, which results in early vessel failure.

The total core uncover is predicted early in the transient after $t = 470$ s. The first fuel rod clad burst due to clad creep failure occurs at $t = 776$ s and the onset of clad melting and dislocation is predicted in the middle hottest part of the core after $t = 1712$ s. In the first reflooding scenario the LPI system is started at $t = 1794$ s and stopped at $t = 2794$ s, while in the second scenario it is started at $t = 2077$ s and stopped at 3077 s. In the accident scenario without LPI injection the vessel failure is predicted early at $t = 5372$ s. In both reflooding scenarios the vessel failure is delayed by about 2 hours and cannot be prevented due to renewed core uncover after the stop of LPI injection. The vessel failure is predicted at $t = 11010$ s and $t = 13142$ s in the first and second reflooding scenarios, respectively.

Table 4.3: Chronology of main events in SLB sequence base case and reflooding scenarios

Event (s)	No core reflood	Core reflood onset at 10 tons degraded mass	Core reflood onset at 45 tons degraded mass
SLB + Loss of offsite power	0 s	0 s	0 s
Reactor scram and primary pump stop	0 s	0 s	0 s
Total core uncovering	470 s	470 s	470 s
First fuel rod clad perforation/burst	776 s	776 s	776 s
First clad melting and dislocation	1712 s	1712 s	1712 s
Start of LPI injection (Q-tot = 360 kg/s)	-	1794 s	2077 s
Stop of LPI injection	-	1894 s	3077 s
Vessel failure	5372 s	11010 s	13142 s

The time evolution of main parameters which describe the thermal-hydraulic behavior of the primary system and the in-vessel core degradation is illustrated from Figure 4.2 to Figure 4.9, for both reflooding scenarios in comparison with the base case results.


Primary system pressure

Following break opening at $t = 0$ s the primary system depressurizes rapidly towards the containment pressure which, in turn, is assumed to increase of 0.5 bar over the atmospheric pressure, during the initial primary coolant blowdown phase. The primary pressure approaches the containment pressure within the first 15 minutes of the transient (see Figure 4.2). At the onset of reflood the strong vaporization of water in contact with the hot damaged structures of the core leads to sudden pressure spikes up to about 40 bar. After the pressure peak, the release of the steam through the break leads to progressive pressure decrease. Smaller pressure spikes are predicted around $t = 7000$ s, due to massive slumping of hot corium in the lower head of the vessel filled by water.

Break mass flow rate and primary mass inventory

The large initial value of primary mass leakage rate through the surge like break (around 1600 kg/s in the first seconds of the transient) reduces quickly in the short term according to the rapid depressurization of the primary circuit (see Figure 4.3-a). After core reflood, large flow fluctuations are observed at the break outlet, during the refilling of the vessel and the lower part of the hot leg upstream the break (see Figure 4.3-b). In the long term, after the stop of LPI injection, the steam flow rate through the break progressively decreases according to the primary pressure behavior.

According to the coolant mass lost through the break, the primary mass reduces down to approximately 15 ton (7% of initial mass inventory) in the initial transient phase (see Figure 4.4). The residual water is located partly in the vessel lower plenum, below the core bottom elevation, and partly in the loop seal of the cold legs. After the onset of the reflood phase, the primary inventory rises up to about 140 tons (63% of initial mass inventory), during the time interval of 1000 s with the LPI emergency cooling system in operation.

 Ricerca Sistema Elettrico	Sigla di identificazione	Rev.	Distrib.	Pag.	di
	ADPFISS-LP1-031	0	L	54	64

Afterwards, the primary mass inventory start to progressively decrease. Practically, there is no more coolant in the primary system and then also in the lower plenum when the vessel fails.

Core uncover and heatup

Due to fast primary mass inventory depletion the water level fall down below the core bottom early in the first part of the transient (see Figure 4.5). The lower plenum and then the core are quickly completely refilled by water, in few minutes, once the LPI starts, owing to the large flow rate of this emergency cooling system. After stop of LPI operation, the core is uncovered again completely in about 30 minutes.

The heat-up at the core top starts at $t = 400$ s during the initial core uncover (see Figure 4.6). The clad temperature rises progressively at an average heat-up rate of ~ 1.3 K/s until reaching the zircaloy melting point (~ 2100 K) at $t = 1600$ s and then the temperature threshold for debris bed formation and collapse (2500 K) at $t = 2000$ s, in the base case (without reflood) and in the case with delayed onset of core reflood. No clad temperature escalation is predicted at the core top during the oxidation phase, since the zircaloy oxidation proceeds under steam starvation conditions, due to the limited steam production, once the water level fall down below the bottom of the fissile powered zone of the core.

The fuel rods are rapidly quenched at the core top as soon as the core starts to be recovered by water. Since the duration of LPI operation is limited (1000 s), the fuel rods at core top start to heat-up again after $t = 3400$ s and $t = 4600$ s in the two reflooding scenarios starting from slightly and highly degraded core, respectively. After some times the clad temperature at the core top becomes unreliable due to complete downward relocation of materials (meltdown or debris bed formation and collapse).

Hydrogen generation

The amount of hydrogen produced before reflood is rather limited because of steam starvation conditions. After the onset of reflood, the steam produced leads to fast oxidation of metallic materials still present in the collapsed core structures (debris). Up to 270 kg of hydrogen is produced during reflood starting from the slightly degraded core (see Figure 4.7). A smaller amount of 200 kg is predicted starting the reflood with a highly degraded core. Most of hydrogen is in this case produced by the oxidation of debris bed. Around 70 kg of hydrogen is produced after core reflood and its cooldown in the two scenarios, mainly due to further oxidation of debris and melt during the second core heat-up phase.

In-vessel core degradation progression

At the onset of core reflood, fast quenching of the partially damaged fuel rods leads to fuel rod clad embrittlement with extended debris formation, collapse and accumulation in the lower part of the core, as indicated by the sudden increase in the total mass of degraded core materials in Figure 4.8, with respect to the base case without reflooding. The extension of core degradation is similar in the two reflooding scenarios.

After core refilling the debris remain in a coolable configuration and then the core degradation and melt progression is temporarily stopped. In both reflooding scenarios the

corium relocation into the lower plenum is much smaller than in the base case (see Figure 4.9) and, thanks to molten jet fragmentation and debris coolability in the lower head, the early failure of the vessel is then prevented.

No recirculation of water from the sump is considered in these scenarios which might guarantee the core recovery in the long term. Therefore, after the stop of LPI operation, there is new core uncover and heat-up, during which the in-core debris start to gradually melt and relocate in the lower plenum, and thus threatening the integrity of the lower head. The vessel failure is calculated at about 11010 s and 13142 s in the 10 tons and 45 tons reflooding scenarios, respectively. By this time the total mass of corium relocated in the lower head is approximately 130 tons in both scenarios.

The in-vessel core degradation configuration just before and after reflood is illustrated in Figure 4.10 and Figure 4.11 for the two reflooding scenarios, respectively. The pictures in the figures put in evidence the large amount of debris and melt that develops and accumulates in the lower part of the core during reflood.

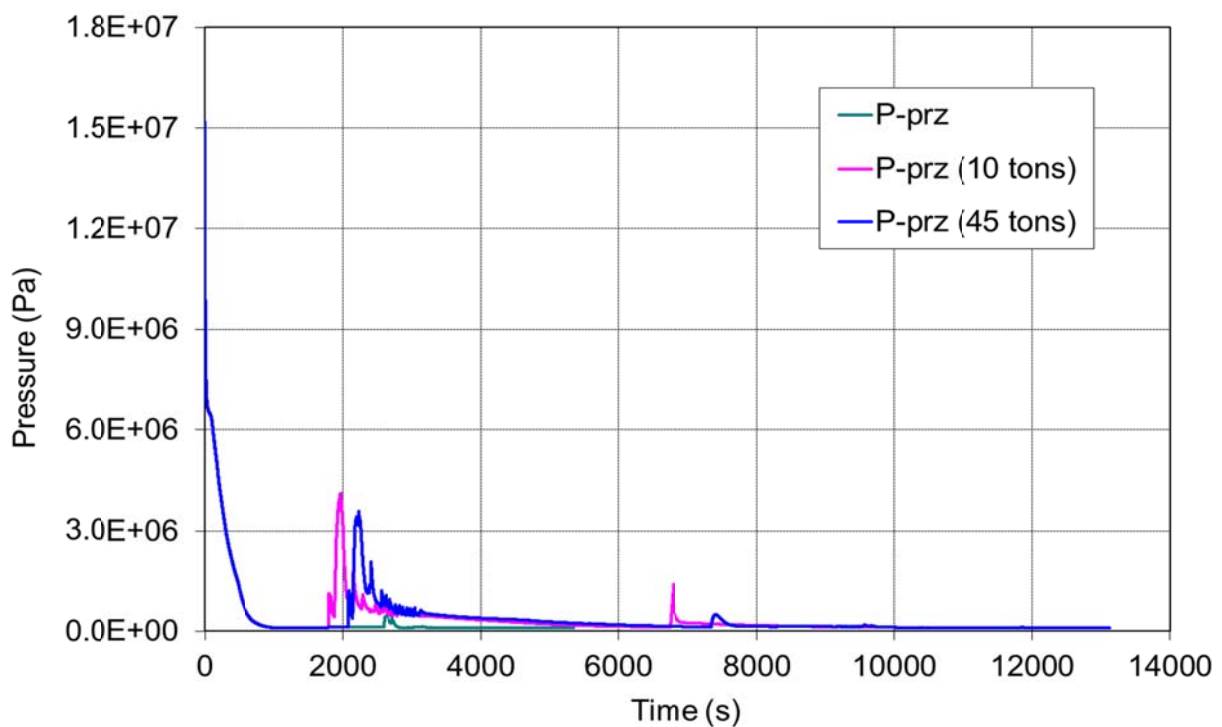


Figure 4.2: Primary system pressure

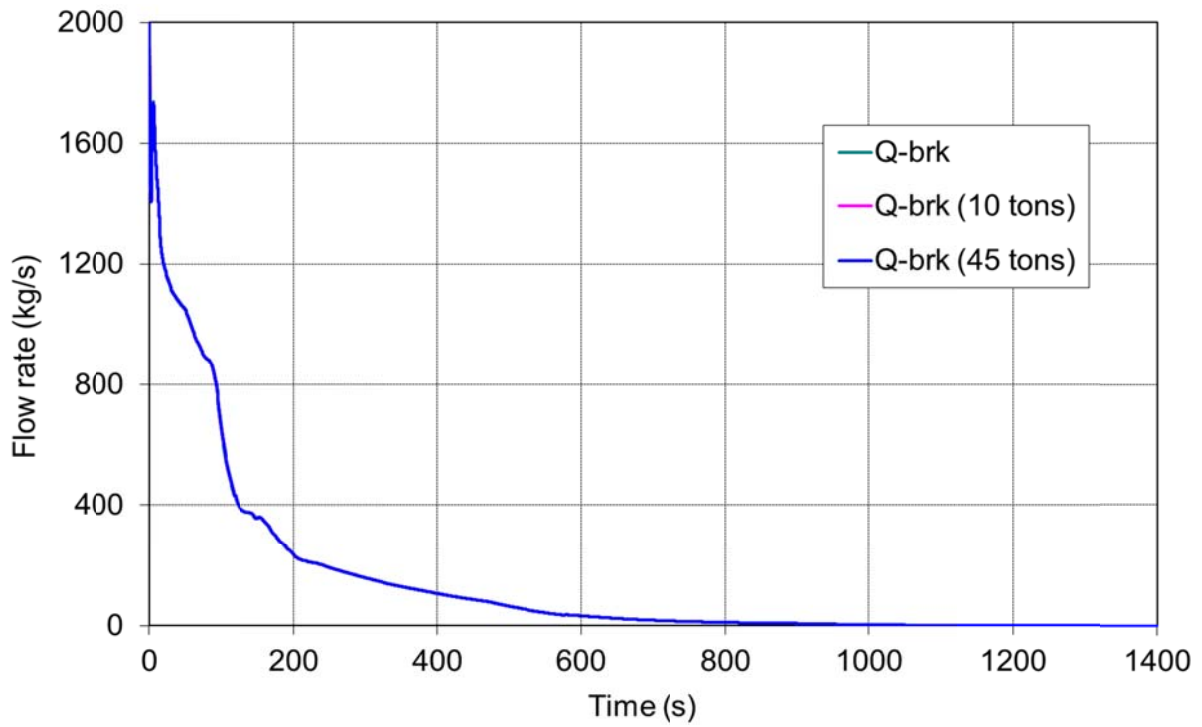


Figure 4.3-a: Break mass flow rate (*short term*)

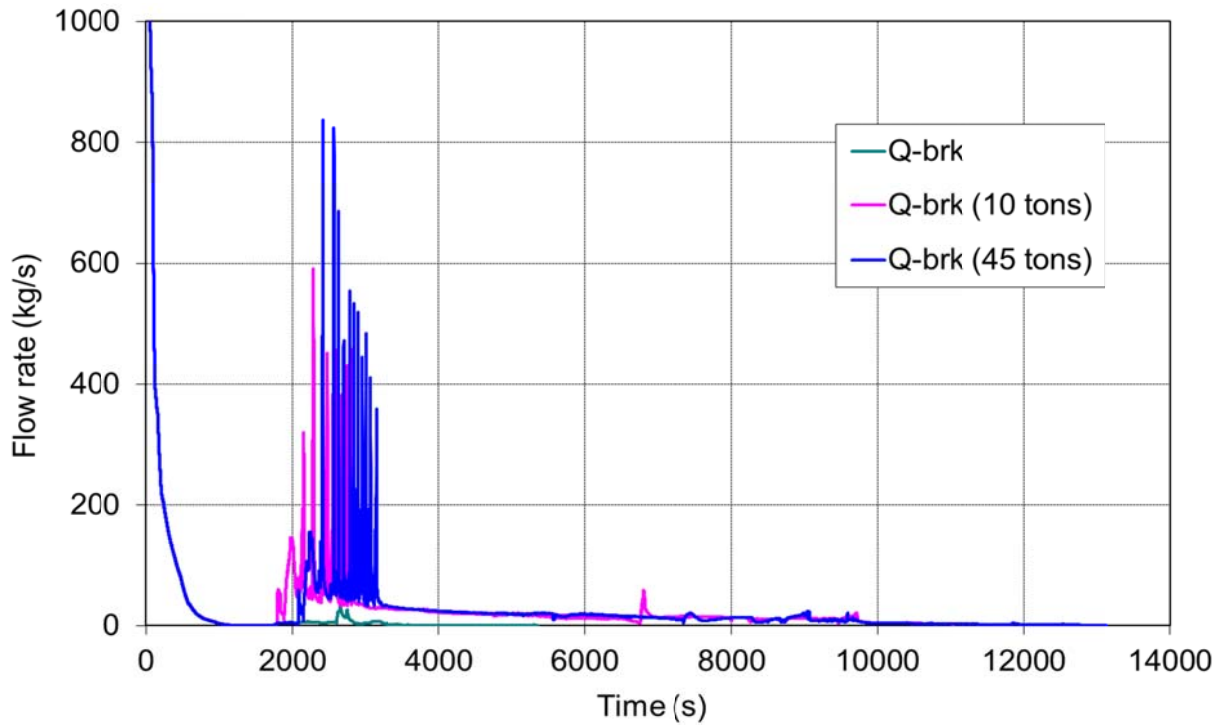


Figure 4.3-b: Break mass flow rate (*long term*)

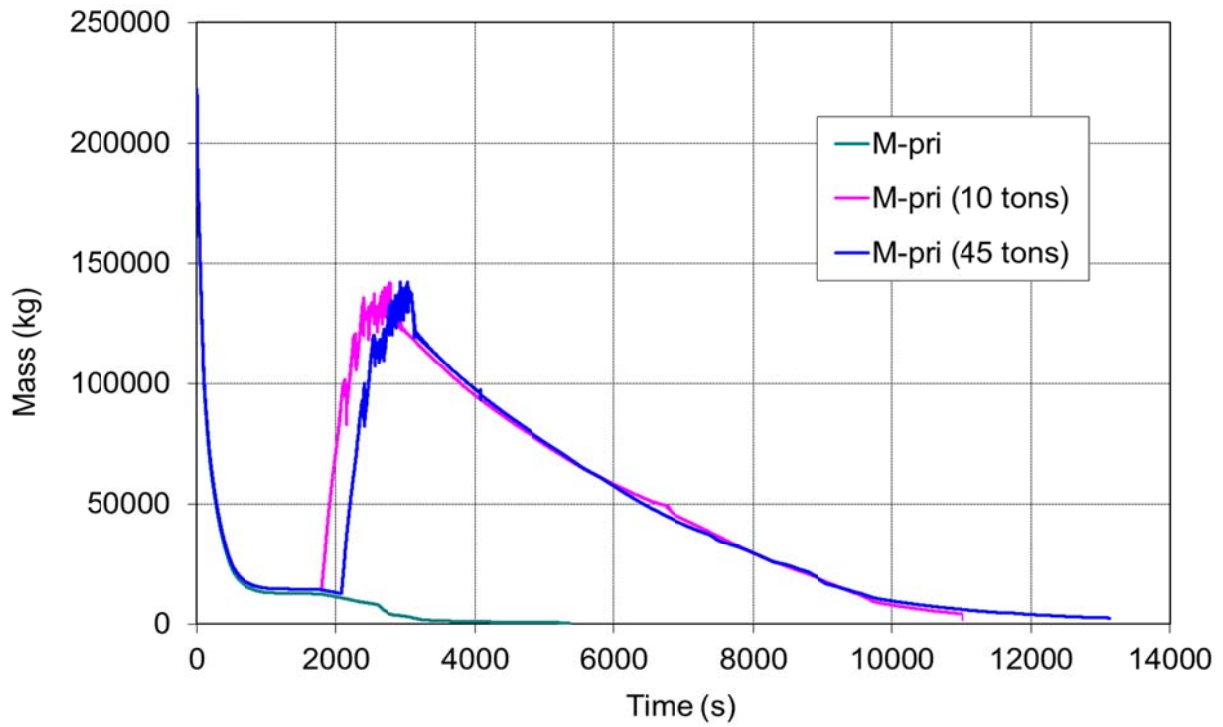


Figure 4.4: Primary coolant mass inventory

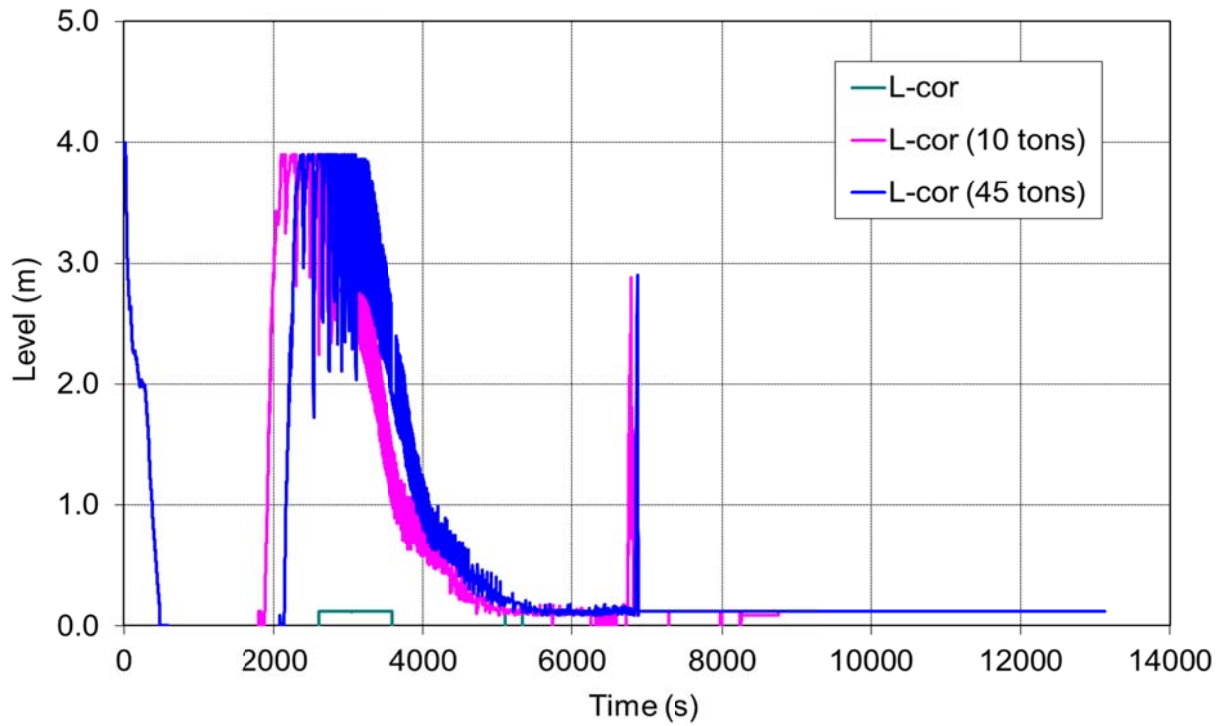


Figure 4.5: Core collapsed level

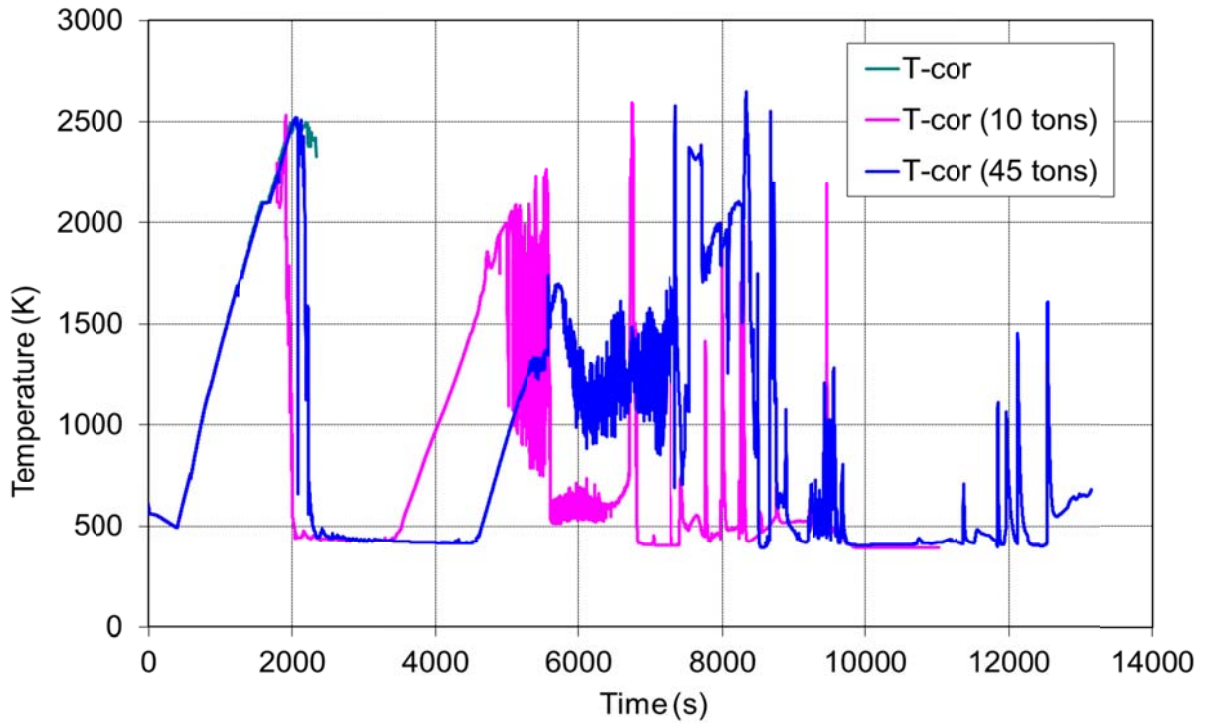


Figure 4.6: Clad temperature at core top in the inner core ring

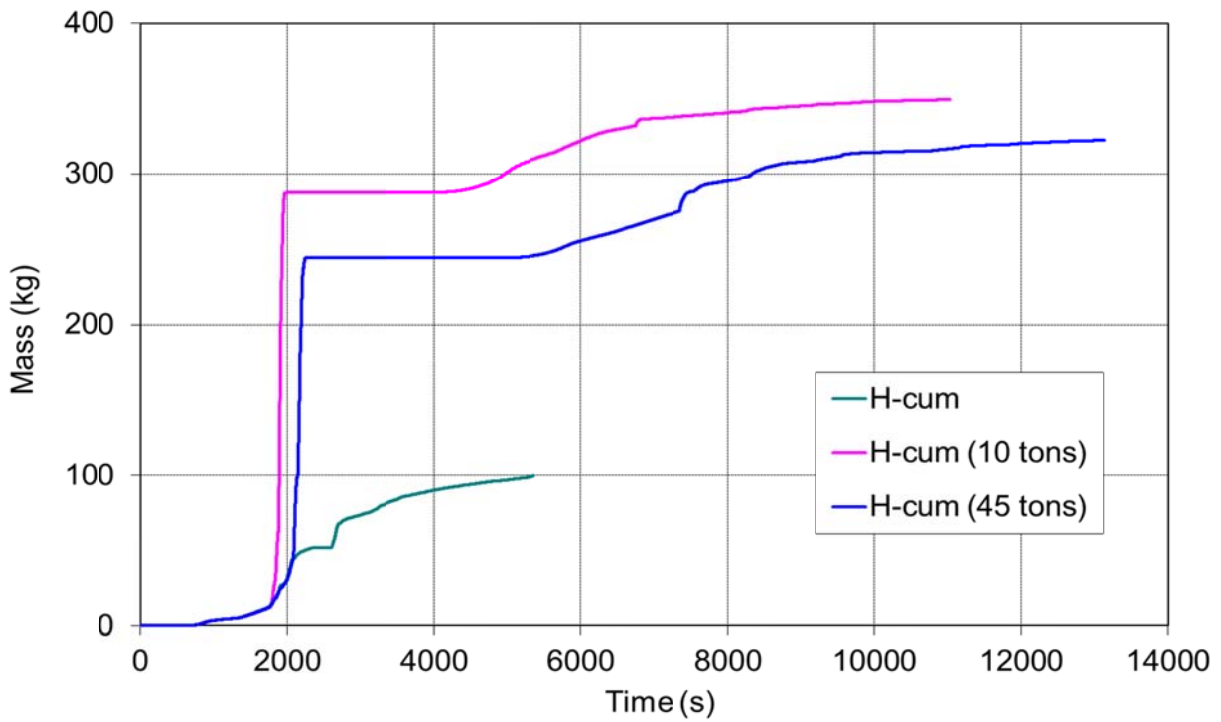


Figure 4.7: Cumulated hydrogen mass

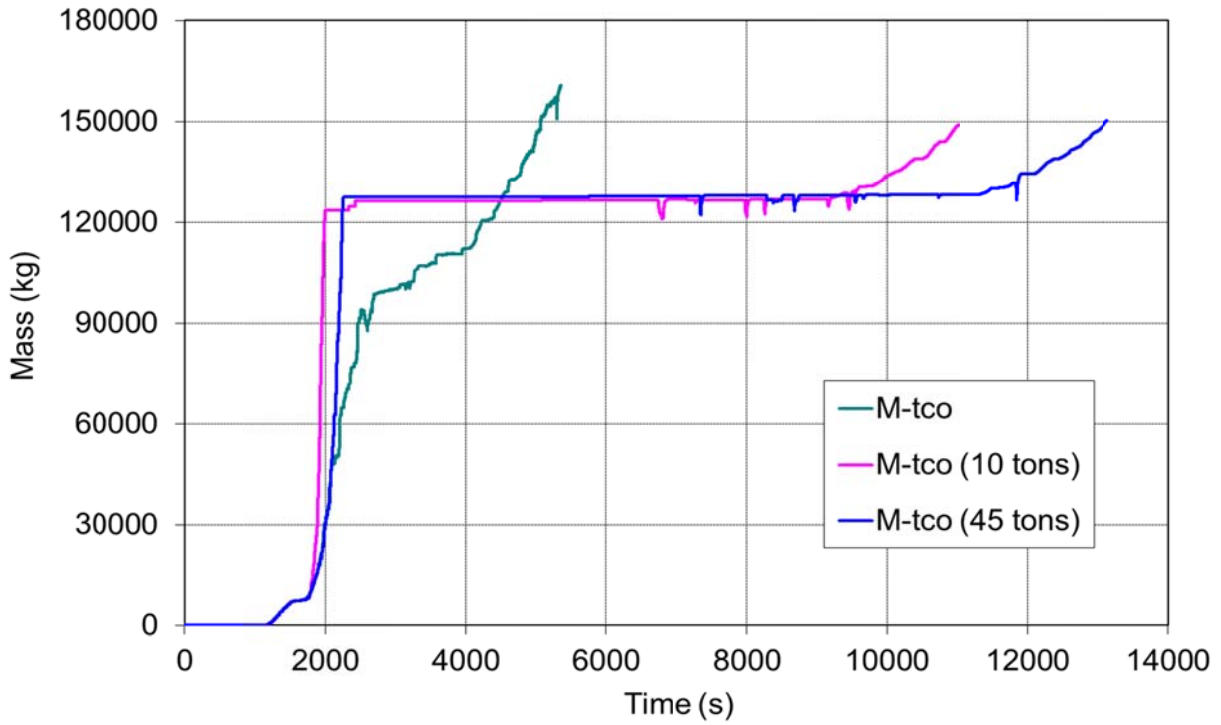


Figure 4.8: Total mass of degraded core materials

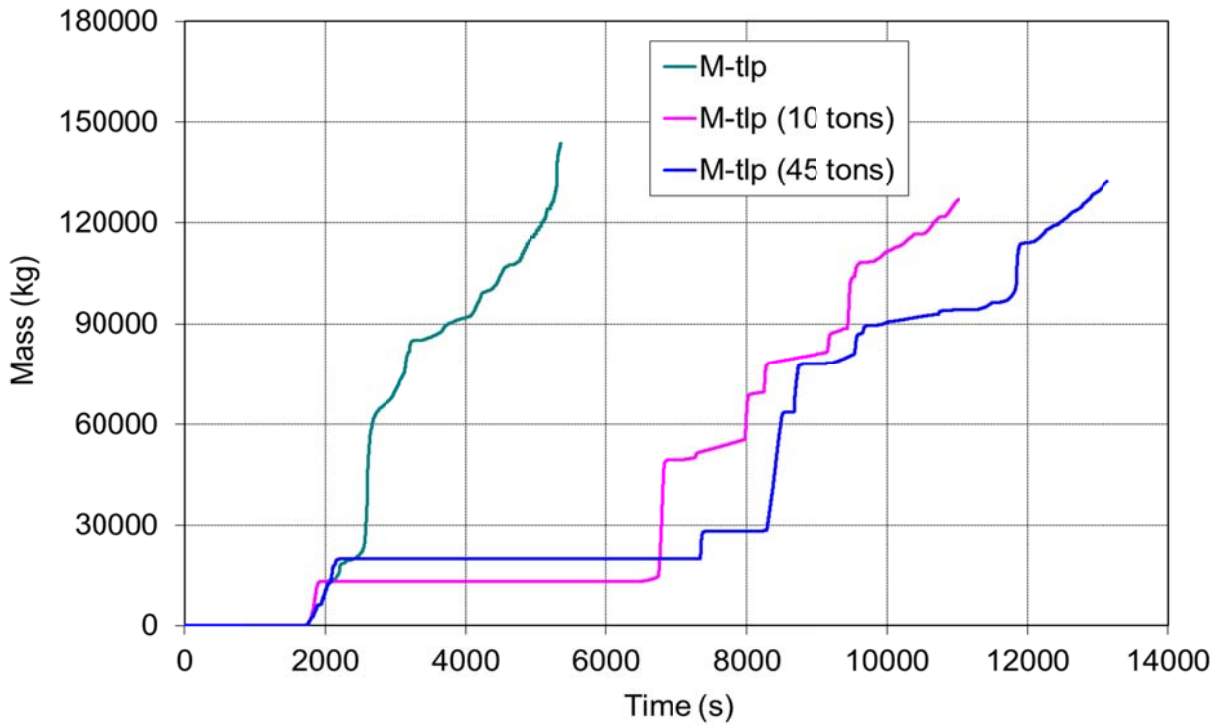


Figure 4.9: Total mass of materials relocated into the lower plenum

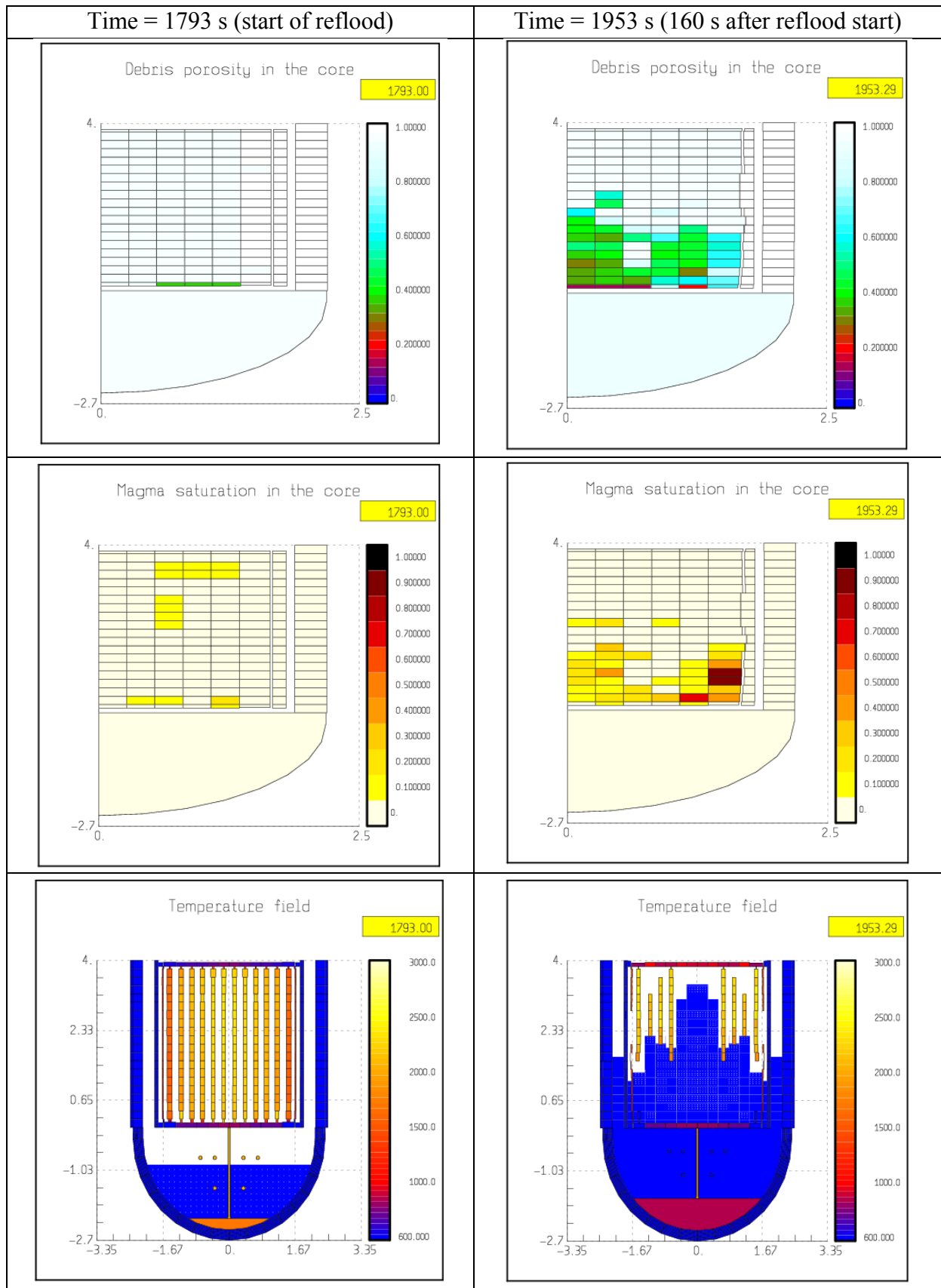


Figure 4.10: Core configuration just before and after reflood (10 tons case)

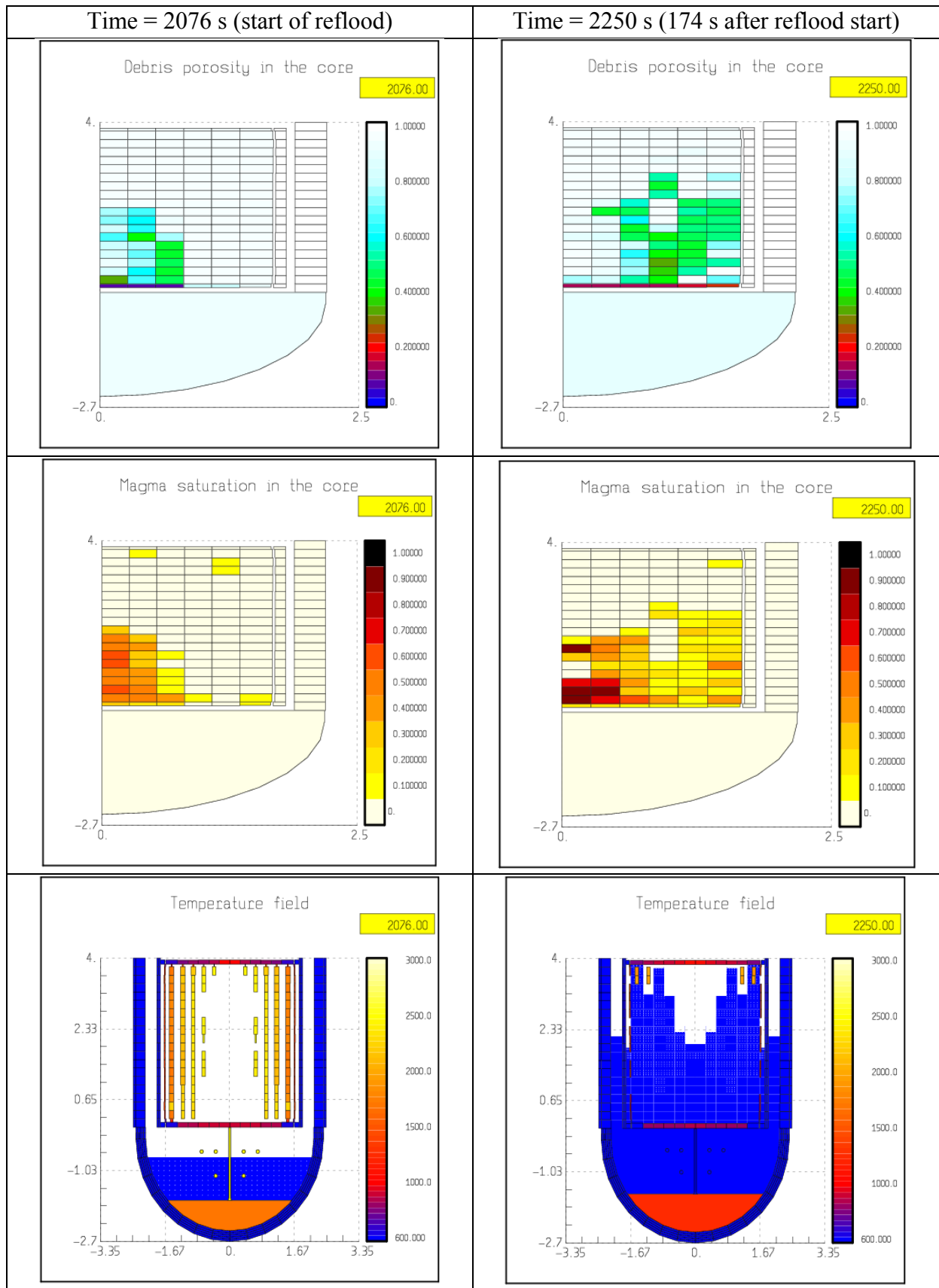




Figure 4.11: Core degradation configuration just before and after reflood (45 tons case)

 Ricerca Sistema Elettrico	Sigla di identificazione	Rev.	Distrib.	Pag.	di
	ADPFISS-LP1-031	0	L	62	64

4.5 Final remarks

The calculation of the SLB sequence and reflooding scenarios has allowed the in-depth verification of both thermal-hydraulic and core degradation code models and then to assess the robustness of the ASTEC V2.0R2 code under the most severe core damage conditions until corium relocation in the lower plenum, which can threaten the vessel wall integrity. The reflooding scenarios investigated have further allowed the verification of the code for evaluating the coolability of a damaged core and the success of accident management measures based on the availability and capability of emergency core cooling systems, which can be made available later during the accident progression, at different levels of core degradation.

The results of the SLB sequence and reflooding scenarios show that the core melt progression, molten core slumping and vessel failure can be delayed by the actuation of the LPI system with a very high flow rate. Once the availability of water from the LPI system is over, recirculation of water from the sump is needed to avoid further core uncovering and heatup in the long term and then terminate the severe accident.

 Ricerca Sistema Elettrico	Sigla di identificazione	Rev.	Distrib.	Pag.	di
	ADPFISS–LP1-031	0	L	63	64

5. Conclusions

The activities performed by ENEA in the frame of Tasks 3.1 & 3.2 of PAR2013 – LP1 and devoted to the development and verification of code models used in the analysis of accidents in nuclear power plants are divided into three topics. The following conclusions can be drawn for each of them:

- ***Upper plenum temperature calculations: comparison of TRANSURANUS with a 2D model under steady-state conditions***


New 2D and finite element models have been developed and implemented in the TRANSURANUS code for the calculation of the fuel rod plenum temperature. The models' predictions showed a good agreement under the conditions selected for the comparison and indicated that the conductive heat transfer has a prominent role in helium rods. The results of the FRAPCON–3 model showed that fission gas release could cause a transition from a laminar to a turbulent regime of heat transfer. Therefore, the hypothesis of negligible convective contribution to heat transfer assumed in the 2D models should be reconsidered in the case of significant fission gas release. A limited effect was noted for the gamma heating of the plenum spring. These preliminary conclusions will be further assessed and verified. Geometrical effects not modelled in a 1.5 dimensional code and transient conditions will be considered as well.

- ***Complementary ICARE/CATHARE calculations to support the experimental program PEARL***

The complementary analyses of PEARL debris bed experiments with ICARE/CATHARE have highlighted the importance of some parameters on the debris bed quenching behavior. The calculations with a ticker unheated region (bypass), at the outside of the stainless steel debris bed, show very limited effect on the debris bed behavior during the reflooding. In particular, the increase of the bypass size has a poor efficacy to enhance 2D effects, consisting on a preferential water penetration through the external debris bed region, during the reflooding. The obtained results confirm the conclusions of the previous work on the essential role of the water flow rate to enhance 2D effects. Increasing water flow rate and steam production rate, the pressure gradient between the debris bed center and the periphery also increases, favoring the water flow through the bypass to the detriment of the inner region of the heated debris bed. 2D behavior of the water penetration within the debris bed becomes visible, independently on the bypass thickness, at a water flow rate of 15 m/h. 2D effects are well established when the water flow rate is equal to 30 m/h.

- ***Calculation of degraded core reflooding scenarios in the TMI-2 plant with the ASTEC code***

The calculation of the SLB sequence and reflooding scenarios performed in the frame of OECD Benchmark Exercise on the TMI-2 plant has further confirmed the

 Ricerca Sistema Elettrico	Sigla di identificazione	Rev.	Distrib.	Pag.	di
	ADPFISS-LP1-031	0	L	64	64

robustness of the ASTEC code under the most severe core damage conditions with large corium relocation in the lower plenum and lower head vessel failure. The reflooding scenarios investigated allowed the verification of the success criteria for accident management measures based on the availability and capability of emergency core cooling systems, which can be made available later during the accident progression into severe conditions. The results of the SLB sequence and reflooding scenarios show that the core melt progression, molten core slumping and vessel failure can be delayed by the actuation of the LPI system with a very high flow rate. Once the availability of water from the LPI system is over, recirculation of water from the sump is needed to avoid further core uncover and heatup in the long term and then terminate the severe accident.

Besides the important achievements in code model development, improvement and verification, these activities contributed to strengthen research collaborations with foreign partners at international level and acquire tools and their knowledge for safety analysis applications to the existing nuclear power plants located near the border of our country.